AD-773 368

INSTRUMENT LANDING SYSTEM PERFORMANCE PREDICTION

G. Chin, et al

Transportation Systems Center

Prepared for:

Federal Aviation Administration

January 1974

Best
Available
Copy

AD-773368

1. Report No. FAA-RD-73-200	2. Government Accession No	3. Recipient's Catalog No
4. Title and Subtitle INSTRUMENT LANDING SYSTEM PERFORMANCE PREDICTION		5. Report Date January 1974
		6. Performing Organization Code
7. Author's' G. Chin, L. Jordan, D. Kahn, S. Morin		8. Performing Organization Report No DOT-TSC-FAA-73-21
9. Performing Organization Name and Address Department of Transportation Transportation Systems Center Kendall Square Cambridge MA 02142		10. Work Unit No FA407-R4129
		11. Contract or Grant No.
		13. Type of Report and Period Covered Final Report July 1972 - June 1973
12. Sponsoring Agency Name and Address Department of Transportation Federal Aviation Administration Systems Research and Development Service Washington DC 20590		
		14. Sponsoring Agency Code

15. Supplementary Notes

16. Abstract

   Further achievements made in fiscal year 1973 on the development of an Instrument Landing System (ILS) performance prediction model are reported. These include ILS localizer scattering from generalized slanted rectangular, triangular and cylindrical surfaces, a model of a parabolic localizer antenna system and an ILS glide slope terrain scattering theory. In addition, applications of this ILS performance prediction model are presented.

17. Key Words · ILS · Scattering · Localizer · Glide Slope	18. Distribution Statement DOCUMENT IS AVAILABLE TO THE PUBLIC THROUGH THE NATIONAL TECHNICAL INFORMATION SERVICE. SPRINGFIELD VIRGINIA 22151		
19. Security Classif. (of this report) Unclassified	20. Security Classif. (of this page) Unclassified	21. No. of Pages 124	22. Price $4.50

Form DOT F 1700.7 (8-69)

ia

PREFACE

This final report covers the work performed during fiscal year 1973 in applying and further developing the Transportation Systems Center (TSC) Instrument Landing System (ILS) performance prediction model. In addition to the model applications and development reported here, the TSC group also undertook a limited scale modeling effort. The results of this scale modeling effort will be released in two special reports to be issued early in fiscal year 1974.

The work reported on here was performed by members of the Modeling and Analysis Section of the Electromagnetic Technology Division, Transportation Systems Center for the Category I and II ILS Section of the Terminal Navigation Branch of the Systems Research and Development Service, Federal Aviation Administration (FAA).

Preceding page blank

TABLE OF CONTENTS

LIST OF ILLUSTRATIONS

LIST OF ILLUSTRATIONS (CONTINUED)

LIST OF ILLUSTRATIONS (CONTINUED)

1. INTRODUCTION

The objective of the Instrument Landing System (ILS) Perform-
ance Prediction Program is to provide a relatively inexpensive
scientific means by which ILS performance may be predicted. The
prediction is accomplished through the use of a physics model
based on electromagnetic scattering theory whose equations have
been programmed for use on a high speed computer. The model
predicts such things as the ILS performance that would result from
a proposed addition at an airport of hangars, terminal buildings
or control towers. Suggested modifications to the proposed build-
ing plan may be made following the prediction study. The model is
also used to predict comparative ILS antenna array performance.
This prediction is useful if one is in doubt as to the ILS needed
for a new runway instrumentation, or for the upgrading to more
stringent FAA requirements of an already instrumented runway, or
is useful as a means of stu'ying a problem site which has not
produced an acceptable course structure with the existing ILS
antenna array. The need for expensive testing of different antenna
systems for such sites is then considerably reduced with the use
of the ILS performance prediction model.

The users of the ILS Performance Prediction Model will be
personnel from the Federal Aviation Administration (FAA). The
model will serve as an aid to the FAA personnel in helping with
the prediction of ILS performance when modifications to the exist-
ing airport environment have been proposed. The FAA should then
be in a better position to recommend any necessary changes as
indicated by the model.

A Phase I ILS localizer computer program package for localizer
performance prediction has been developed and has been delivered
to the FAA. This program is capable of predicting localizer
performance in a medium complex airport environment where the
scatterers can be represented as large rectangular or cylindrical
perfect reflectors. These generally are not important limitations
as most important derogators are typically the large nearly

perfectly conducting metallic or metal reinforced concrete hangars and terminal buildings. For structures which are not perfectly reflecting, the model gives a worst case result. The basic electromagnetic scattering theory of this Phase 1 localizer performance prediction model is presented in this report.

The computer program written for this physics model has been structured to allow easy variation of key parameters. For example, the performance of a particular localizer antenna array in a changing airport environment may be predicted in order to determine the effect on the localizer performance of different building locations and orientations; and the relative performance of different ILS localizer antenna arrays may be predicted for a given airport environment. This parametrization of the model allows a variation of either the antenna system or the airport environment for systematic comparative study predictions.

A number of such studies were made this year with the Phase 1 ILS localizer performance prediction computer program. These applications of the model to specific airports are discussed in Section 5 of this report.

This report is essentially divided into two parts. These are an applications part, mentioned above, and a theoretical part in which localizer, glide slope terrain and parabolic antenna scattering theory are developed.

In Section 2 the physics basic to the development of the ILS localizer performance prediction model is developed with reference to an earlier Transportation Systems Center (TSC) publication.[1] This earlier work is further developed to allow a determination of localizer performance when the localizer radiation is scattered from a rectangular perfectly-conducting slab with arbitrary tilt angles and heights above the ground plane. In the same section, the localizer scattering theory for vertical cylinders (simulating water towers and other cylindrical scatterers) is developed. Appendixes A, B and C further extend these results. Appendix A develops the theory of scattering from cylindrical objects raised above the ground plane. In Appendix B the scattering theory for

triangular shaped objects with arbitrary tilt angles and heights above the ground plane is presented. This latter is useful in shortening the running time of the computer program particularly when complex shaped buildings which can be broken up into rectangular and triangular shaped parts are present. A method of predicting localizer performance when there is a hump in the runway is developed in Appendix C. Since this is a relatively common occurrence, its addition to the Performance Prediction Model extends the applicability of the model.

Section 3 presents the theory of ILS glide slope terrain scattering under conditions of important large scale terrain variations. Applications illustrating this glide slope terrain scattering theory are presented.

Section 4 presents the method and theory used to analyze the Texas Instruments parabolic localizer antenna for inclusion in the ILS localizer performance prediction model. Appendix E contains a short discussion on localizer array patterns when mutual coupling is present.

Section 5 discusses the applications of the ILS localizer performance prediction model to different airports studied this year. Finally, in Appendix D, glide slope fuselage scattering is discussed and a method of evaluating the scattering functions is presented.

2. LOCALIZER SCATTERING

2.1 INTRODUCTION

The techniques for investigating ILS multipath problems which were developed in the TSC-FAA report "Instrument Landing System Scattering"[1] by G. Chin, L. Jordan, D. Kahn and S. Morin have been applied to two previously untreated scatterers. Specifically, we have developed and incorporated into our basic localizer computer program formulas describing the scattering characteristics of an elevated, tilted rectangular slab and a right, circular cylinder. The detailed calculations of these scattering formulas are presented in the following two sections.

2.2 LOCALIZER SIGNAL SCATTERING BY AN ELEVATED RECTANGULAR SLAB

In Reference 1, localizer signal scattering, by a flat, vertical, rectangular wall resting on the ground was investigated. We now examine the more general problem of localizer scattering by a flat, rectangular slab which is elevated above the ground and tilted away from the vertical. The base of the slab is assumed to be parallel to the ground plane. It is further assumed that the slab is perfectly conducting.

The geometry of the problem is illustrated in Figure 2-1. The x-y plane is the ground plane. For simplicity, it is assumed that the ground is perfectly flat and perfectly conducting. The x-axis represents the center line of the runway while the z-axis is perpendicular to the ground. The unit vectors in the x, y, and z directions are denoted by $\hat{e}_x$, $\hat{e}_y$, and $\hat{e}_z$ respectively. The unit vector $\hat{\eta}$ is parallel to the base of the slab while $\hat{\xi}$ is perpendicular to $\hat{\eta}$ and lies in the plane of the slab.

The parameters θ and δ denote, respectively, the angle between $\hat{\eta}$ and $\hat{e}_x$ and $\hat{\xi}$ and $\hat{e}_z$. In terms of the unit vectors $\hat{e}_x$, $\hat{e}_y$, and $\hat{e}_z$, $\hat{\eta}$ and $\hat{\xi}$ have the following representations:

$$\hat{\eta} = \cos\theta\,\hat{e}_x - \sin\theta\,\hat{e}_y \qquad (2.1)$$

4
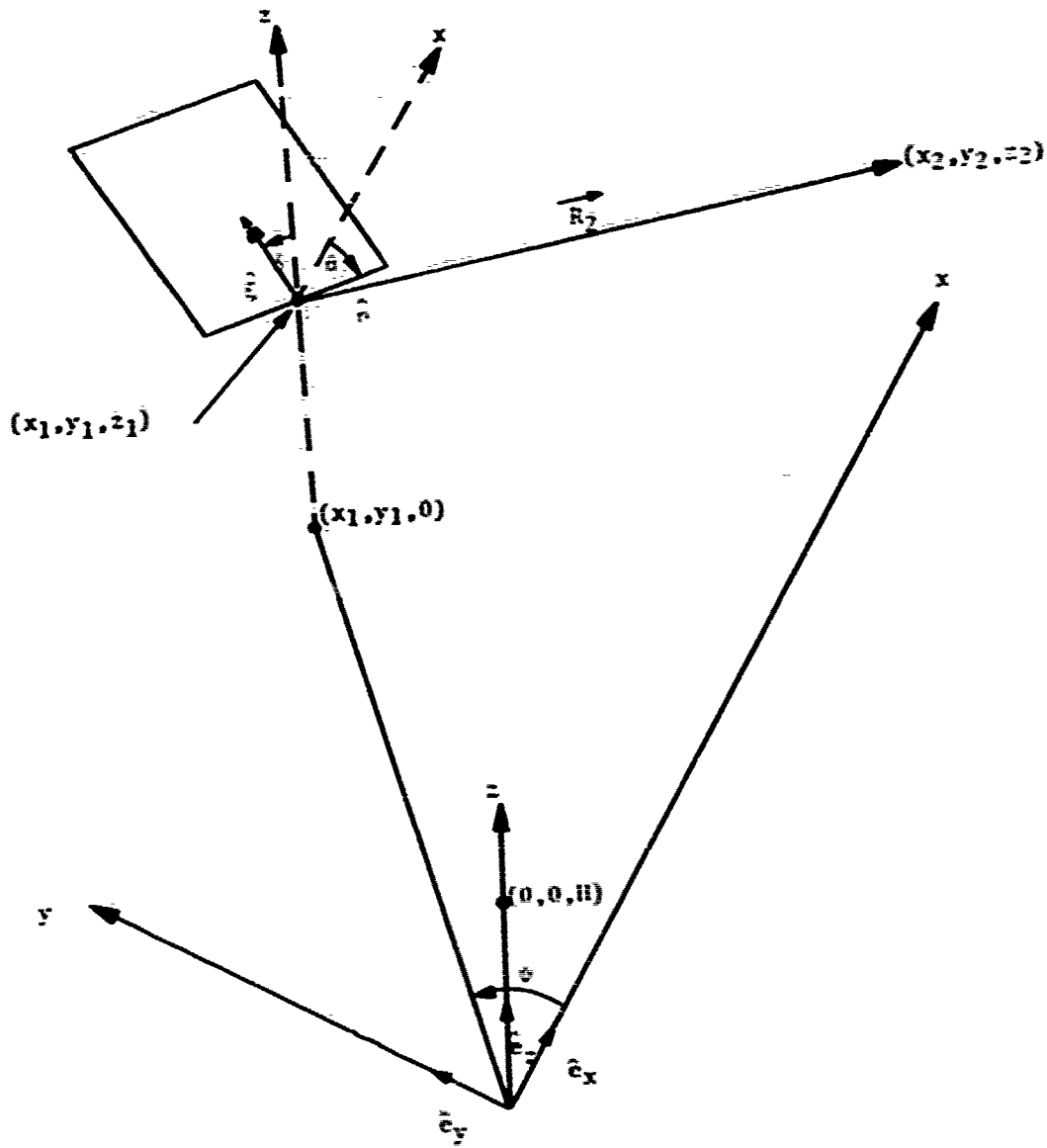
Figure 2-1.   Geometry of the Scattering Problem

$$\hat{\xi} \quad \sin\theta \; \hat{e}_x + \cos\theta \; \hat{e}_y) \sin\delta + \cos\delta \; \hat{e}_z . \qquad (2.2)$$

The unit normal pointing <u>into</u> the illuminated surface of the slab will be denoted by $\hat{n}$ and is given by:

$$\hat{n} = \hat{\xi} \times \hat{\eta}$$

$$\hat{n} = \cos\delta \; (\sin\theta \; \hat{e}_x + \cos\theta \; \hat{e}_y) - \sin\delta \; \hat{e}_z . \qquad (2.3)$$

The localizer antenna has coordinates $(0, 0 \; H)$ relative to the x, y, z coordinate system. The height, H, of the antenna above the ground is typically about 10 feet. The midpoint of the base of the slab has coordinates (x_1, y_1, z_1), z_1 being the distance above the ground plane of the base of the slab. The angle ψ is just the azimuth angle of the midpoint (x_1, y_1, z_1):

$$\psi = \tan^{-1}\left(y_1/x_1\right) . \qquad (2.4)$$

Finally, the point with coordinates (x_2, y_2, z_2) represents the location of the localizer receiver.

In the physical optics approximation, the scattered electric field $\vec{E}_s$ in the Fraunhofer or radiation zone of the slab is given by:

$$\vec{E}_s = \frac{ik}{2\pi}\left(\frac{\mu}{\epsilon}\right)^{1/2} \frac{e^{ikR_2}}{R_2} \cdot \hat{R}_2 \times \left(\hat{R}_2 \times \vec{J}\right) , \qquad (2.5)$$

where

$$\vec{J} = \int_{S_+} (\hat{n} \times \vec{H}_i) \; e^{-ik(\hat{R}_2 \cdot \vec{r})} ds . \qquad (2.6)$$

In Equations (2.5) and (2.6), $k = 2\pi/\lambda$ is the wavenumber of the radiation (λ is the wavelength), and μ and ϵ denote, respectively, the permeability and permittivity of space. The unit vector $\hat{R}_2$ points from the midpoint of the base of the slab toward the receiver point:

$$\hat{R}_2 = \vec{R}_2/\hat{R}_2 , \qquad (2.7)$$

6

where

$$\vec{R}_2 = (x_2 - x_1)\,\hat{e}_x + (y_2 - y_1)\,\hat{e}_y + (z_2 - z_1)\,\hat{e}_z \quad , \qquad (2.8)$$

and

$$R_2 = \left[(x_2 - x_1)^2 + (y_2 - y_1)^2 + (z_2 - z_1)^2\right]^{1/2} \quad . \qquad (2.9)$$

The integral $\vec{J}$ defined by Equation (2.6) is carried out over the illuminated surface of the slab. The vector $\hat{n}$ is the unit normal pointing into the surface of the scatterer while $\vec{H}_i$ is the incident magnetic field. The vector $\vec{r}$ is the position vector of an arbitrary point on the illuminated surface relative to the point (x_1, y_1, z_1). A detailed derivation of Equations (2.5) and (2.6) can be found in Section 2 of Reference 1.

It was shown in Reference 1 that the incident magnetic field $\vec{H}_i$ at a field point (x, y, z) produced by a horizontally polarized localizer antenna and its image in the ground plane can be represented approximately as follows:

$$\vec{H}_i = -\hat{e}_z \left(\frac{\varepsilon}{\mu}\right)^{1/2} E_o\, f(\phi)\, \frac{e^{ikR}}{R} \left[1 - e^{2ikzH/D_p}\right] \quad . \qquad (2.10)$$

In Equation (2.10), E_o is an amplitude associated with the localizer antenna while $f(\phi)$ is the horizontal field pattern of the antenna $\left(\phi = \tan^{-1}(y/x)\right)$. The parameters R and D_p denote, respectively, the slant distance and horizontal distance from the localizer to the field point:

$$R = \left[x^2 + y^2 + (z - H)^2\right]^{1/2} \quad , \qquad (2.11)$$

$$D_p = \left[x^2 + y^2\right]^{1/2} \quad . \qquad (2.12)$$

Equation (2.10) provides an accurate representation of $\vec{H}_i$ at field points satisfying the so-called small elevation angle condition:

$$z/D_p \ll 1 \qquad (2.13)$$

It will be assumed in the present work that the inequality (2.13) is satisfied by all points on the surface of the slab.

The vector $\vec{R}$ drawn from the localizer antenna to a point P on the surface of the slab can be represented as follows:

$$\vec{R} = \vec{R}_1 + \vec{r} \qquad (2.14)$$

where $\vec{R}_1 = x_1 \hat{e}_x + y_1 \hat{e}_y + (z_1 - H) \hat{e}_z$ is the position vector of the the midpoint of the base of the slab relative to the antenna and $\vec{r}$ connects the midpoint of the base to the point P. To first order in r/R_1, $R = |\vec{R}|$ can be represented as follows:

$$R \approx R_1 + \hat{R}_1 \cdot \vec{r} \quad , \qquad (2.15)$$

where $\hat{R}_1 = \vec{R}_1 / R_1$. The vector $\vec{r}$ can be expressed in terms of the unit vectors $\hat{n}$ and $\hat{\xi}$ as follows:

$$\vec{r} = \eta \, \hat{n} + \varsigma \, \hat{\xi} \quad , \qquad (2.16)$$

where η ranges from $-L/2$ to $L/2$ (L being the length of the base of the slab) and ς ranges from 0 to h (h being the slant height of the slab). Using Equations (2.1) and (2.2) to express $\hat{n}$ and $\hat{\xi}$ in terms of $\hat{e}_x$, $\hat{e}_y$, and $\hat{e}_z$, Equation (2.16) can be written as follows:

$$\vec{r} = (\eta \cos \theta + \xi \sin \delta \sin \theta) \hat{e}_x + (\xi \cos \theta \sin \delta - \eta \sin \theta) \hat{e}_y$$
$$+ \quad \xi \cos \delta \, \hat{e}_z \quad . \qquad (2.17)$$

For small angles of elevation, the unit vector $\hat{R}_1$ can be written approximately as

$$\hat{R}_1 \approx \cos \psi \, \hat{e}_x + \sin \psi \, \hat{e}_y + \frac{(z_1 - H)}{D_{p1}} \, \hat{e}_z \quad , \qquad (2.18)$$

where $D_{p1} = \sqrt{x_1^2 + y_1^2}$ and ψ is the azimuth angle of the midpoint (cf. Equation (2.4)). Substituting Equations (2.17) and (2.18) into Equation (2.15) yields the following approximate expression for R:

8

$$R \approx R_1 + \eta \cos(\theta+\psi) + \xi \sin \delta \sin(\theta+\psi) + \xi \frac{\cos\delta \ (z_1-H)}{D_{p1}} \qquad (2.19)$$

Introducing the angle of incidence $\gamma = \pi/2 - (\theta+\psi)$, Equation (2.19) can be rewritten more compactly as follows:

$$R \approx R_1 + \eta \sin \gamma + \xi \sin \delta \cos \gamma + \xi \frac{\cos\delta \ (z_1-H)}{D_{p1}} \qquad . \qquad (2.20)$$

The angle γ is just the angle between the projection of $\vec{R}_1$ onto the x-y plane and the projection of the unit normal $\hat{n}$ onto the x-y plane.

The approximate expression for the distance R given in Equation (2.20) can now be substituted into the appropriate complex exponential in Equation (2.10). Some additional approximations will now be made to render the expression for $\vec{H}_i$ given in Equation (2.10) more suitable for the integration indicated in Equation (2.6). Specifically, we will assume that D_{p1} is so much greater than L, the length of the slab, and that $f(\phi)$ is sufficiently slowly varying then $f(\phi)$ can be replaced by $f(\psi)(\psi = \tan^{-1}(y_1/x_1))$ for all points on the surface of the slab. That is to say, we will assume that the horizontal angle subtended by the slab at the localizer antenna is so small that the variations in $f(\phi)$ over the surface of the slab can be ignored.

In like manner, it will be assumed that, to a good approximation, the amplitude factor R^{-1} in (2.10) can be replaced by R_1^{-1} and that the parameter D_p in the expression in parentheses can be replaced by D_{p1}. Incorporating all of these approximations into Equation (2.10), we obtain the following expression for $\vec{H}_i$ on the surface of the slab:

$$\vec{H}_i = 2i\hat{e}_z \left(\frac{\epsilon}{\mu}\right)^{1/2} E_0 f(\psi) \frac{e^{ikR_1}}{R_1} e^{ik\eta \sin \gamma} \cdot e^{ik\zeta \sin \delta \cos \gamma} \cdot$$

$$e^{ikz_1[H+\zeta \cos \delta]/D_{p1}} \cdot \sin \frac{kH}{D_{p1}}[z_1 + \zeta \cos \delta] \cdot \qquad (2.21)$$

Consider now the vector $\vec{R}_2$ from the point (x_1, y_1, z_1) to the observation point (x_2, y_2, z_2). We will denote by D_{p2} the horizontal distance between these two points:

$$D_{p2} = \left[(x_2 - x_1)^2 + (y_2 - y_1)^2\right]^{1/2}$$

Assuming that the elevation angle of the vector $\vec{R}_2$ is very small (i.e. $D_{p2} \gg |z_2 - z_1|$), the unit vector $\hat{R}_2 = \vec{R}_2/R_2$ takes on the approximate form:

$$\hat{R}_2 \approx \cos \sigma \, \hat{e}_x - \sin \sigma \, \hat{e}_y + \frac{(z_2 - z_1)}{D_{p2}} \hat{e}_z , \qquad (2.22)$$

where σ is the angle between the projection of $\vec{R}_2$ onto the x-y plane and the x-axis. Consequently, the quantity $\hat{R}_2 \cdot \vec{r}$ appearing in Equation (2.6) can be written approximately as follows:

$$\hat{R}_2 \cdot \vec{r} = \eta \cos (\sigma - \theta) - \zeta \sin \delta \sin (\sigma - \theta) + \frac{\zeta \cos \delta \, (z_2 - z_1)}{D_{p2}} , \qquad (2.23)$$

where use has been made of Equation (2.17). Introducing the aspect angle $\beta = \pi/2 - (\sigma - \theta)$, Equation (2.23) can be rewritten more compactly as:

$$\hat{R}_2 \cdot \vec{r} = \eta \sin \beta - \zeta \sin \delta \cos \beta + \frac{\zeta \cos \delta \, (z_2 - z_1)}{D_{p2}} . \qquad (2.24)$$

The angle β is just the angle between the projection of $\vec{R}_2$ onto the x-y plane and the projection of $(-\hat{n})$ onto the x-y plane where $\hat{n}$ is the unit inward normal to the surface.

The integral in Equation (2.6) can now be evaluated quite readily. Substituting the expressions for $\hat{n}$, $\vec{H}_i$ and $\hat{R}_2 \cdot \vec{r}$ given respectively, in Equations (2.3) and (2.21), and (2.24) and integrating with respect to η ($-L/2 \le \eta \le + L/2$) and ξ ($0 \le \xi \le h$), we obtain the following result for the scattered field $\vec{E}_s$:

$$\vec{E}_s = - \frac{kL}{2\pi} E_o f(\psi) \frac{e^{ik(R_1+R_2)}}{R_1 R_2} \cos\delta \ \text{sinc} \ \frac{kL}{2} (\sin\gamma - \sin\beta).$$

$$\left[\hat{R}_2 \times (\hat{R}_2 \times \hat{\eta})\right] \cdot \left[I_1 - I_2\right] \qquad (2.25)$$

where $\text{sinc}(x) = \sin x / x$ and I_1 and I_2 are defined as follows:

$$I_1 = \frac{e^{iAh} - 1}{A} , \qquad (2.26)$$

$$I_2 = e^{2ikHz_1/D_{p1}} \left[\frac{e^{iBh} - 1}{B}\right] , \qquad (2.27)$$

where

$$A = k\left[\sin\delta \ (\cos\delta + \cos\beta) + \cos\delta\left\{\frac{(z_1 - z_2)}{D_{p2}} + \frac{(z_1 - H)}{D_{p1}}\right\}\right] , \qquad (2.28)$$

$$B = A + \frac{2kH}{D_{p1}} \cos\delta . \qquad (2.29)$$

For the small angles of elevation considered here, $\vec{E}_s$ is essentially parallel to the ground and its magnitude E_s, is given by:

$$E_s = - \frac{kL}{2\pi} E_o f(\psi) \frac{e^{ik(R_1+R_2)}}{R_1 R_2} \cos\delta \cos\beta \ \text{sinc} \ \frac{kL}{2}(\sin\gamma - \sin\beta).$$

$$\cdot \left[I_1 - I_2\right] . \qquad (2.30)$$

To take into account the image of the slab in the ground plane, the expression for E_s given in Equation (2.30) should be evaluated at the image of the observation point $(x_2, y_2, -z_2)$ and

11

the result subtracted from Equation (2.30). The final result for the total scattered field E_{ST} (direct plus ground reflected) at the receiver is just:

$$E_{st} = E_s(x_2,y_2,z_2) - E_s(x_2,y_2,-z_2) \quad , \tag{2.31}$$

where E_S is given in Equation (2.30).

The expressions for the scattered electric field generated by an elevated, tilted, rectangular slab developed in this section constitute the basic mathematical formulas used in our localizer computer program for treating ILS signal scattering by structures with plane surfaces.

2.3 LOCALIZER SIGNAL SCATTERING BY A RIGHT, CIRCULAR CYLINDER

In this section, localizer signal scattering by a right, circular cylinder is investigated. This problem is of practical importance since cylindrical structures, such as gas storage tanks, are frequently to be found near airport runways.

The geometry of the problem is illustrated in Figure 2.2. The x-y plane is the ground plane which we assume to be perfectly flat and perfectly conducting. The x-axis represents the center line of the runway while the z-axis is perpendicular to the ground plane and points out of the page. The unit vectors in the x, y, and z direction are denoted by $\hat{e}_x$, $\hat{e}_y$, and $\hat{e}_z$, respectively. The coordinates of the localizer relative to the x,y,z coordinate system are $(0,0,H)$. The cylinder is assumed to be perfectly conducting and to be resting on the ground. The radius of the cylinder is denoted by a. The coordinates of the center of the base of the cylinder are denoted by $(x_1,y_1,0)$. The azimuth angle of this center point is denoted by $\psi(\psi=\tan^{-1}(y_1/x_1))$. The point with coordinates (x_2,y_2,z_2) represents the location of the localizer receiver. The vectors $\vec{R}_1$ and $\vec{R}_2$ denote, respectively, the vector connecting the localizer   enna to the point $(x_1,y_1,0)$ and the vector connecting the point $(x_1,y_1,0)$ to the receiver point (x_2,y_2,z_2).

12

$$\vec{R}_1 = x_1 \, \hat{e}_x + y_1 \, \hat{e}_y - H \, \hat{e}_z \quad , \tag{2.32}$$

$$\vec{R}_2 = (x_2 - x_1) \, \hat{e}_x + (y_2 - y_1) \, \hat{e}_y + z_2 \, \hat{e}_z \quad . \tag{2.33}$$

Finally, the angle β is just the obtuse angle between the projections of $\vec{R}_1$ and $\vec{R}_2$ onto the x-y plane.

Equations (2.5) and (2.6) will be used to calculate the scattered electric field in the radiation zone of the cylinder. The vector $\vec{r}$ appearing in Equation (2.6) should now be interpreted as connecting the center point $(x_1, y_1, 0)$ to an arbitrary point P with coordinates (x, y, z) on the illuminated surface of the cylinder. Clearly, the vector $\vec{r}$ can be represented as follows:

$$\vec{r} = a \cos \phi \, \hat{n} + a \sin \phi \, \hat{\xi} + z \, \hat{e}_z \quad , \tag{2.34}$$

where

$$\hat{n} = \cos \psi \, \hat{e}_x + \sin \psi \, \hat{e}_y \quad , \tag{2.35}$$

and

$$\hat{\xi} = - \sin \psi \, \hat{e}_x + \cos \psi \, \hat{e}_y \quad . \tag{2.36}$$

The vector $\hat{n}$ is the unit vector in the direction of the projection of $\vec{R}_1$ onto the x-y plane and the angle ϕ is angle between $\hat{n}$ and the projection of $\vec{r}$ onto the x-y plane. Since we are assuming that the cylinder is in the far field of the localizer, ϕ ranges, to good approximation, from $\pi/2$ to $3\pi/2$ on the illuminated surface of the cylinder. Substituting Equations (2.35) and (2.36) into (2.34), we obtain the following expression for the position vector $\vec{r}$:

$$\vec{r} = a \cos(\phi + \psi) \, \hat{e}_x + a \sin(\phi + \psi) \, \hat{e}_y + z \, \hat{e}_z \quad . \tag{2.37}$$

As in Section 2.2, we will make the small elevation angle approximation so that, to a good approximation, the total incident magnetic field $\vec{H}_i$ (direct plus ground reflected) at a point P on the surface of the cylinder is given by:

15

$$\vec{H}_i = - \hat{e}_z \left(\frac{\varepsilon}{\mu}\right)^{1/2} E_o f(\psi) \frac{e^{ikR_1}}{R_1} \left[1 - e^{2ikzH/D_{p1}}\right] e^{ik\hat{R}_1 \cdot \vec{r}} \quad . \tag{2.38}$$

where $\hat{R}_1 = \vec{R}_1/R_1$ and $D_{p1} = [x_1^2 + y_1^2]^{1/2}$. For small angles of elevation, $\hat{R}_1$ can be represented approximately as follows:

$$\hat{R}_1 \approx \cos \psi \; \hat{e}_x + \sin \psi \; \hat{e}_y - \frac{H}{D_{p1}} \hat{e}_z \quad . \tag{2.39}$$

Consequently, the inner product $\hat{R}_1 \cdot \vec{r}$ becomes simply (cf. Eq. (2.37)):

$$\hat{R}_1 \cdot \vec{r} = a \cos \phi - \frac{zH}{D_{p1}} \quad . \tag{2.40}$$

Substituting Equation (2.40) into (2.38), we obtain the following result for $\vec{H}_i$:

$$\vec{H}_i = 2i \; \hat{e}_z \left(\frac{\varepsilon}{\mu}\right)^{1/2} E_o f(\psi) \frac{e^{ikR_1}}{R_1} e^{ika \cos\phi} \sin \frac{kHz}{D_{p1}} \quad . \tag{2.41}$$

The unit inward normal to the cylindrical surface at the point P is given by:

$$\hat{n} = - \cos (\phi+\psi) \; \hat{e}_x - \sin (\phi+\psi) \; \hat{e}_y \quad . \tag{2.42}$$

For small angles of elevation, the unit vector $\hat{R}_2 = \vec{R}_2/R_2$ can be written approximately as follows:

$$\hat{R}_2 \approx \cos \gamma \; \hat{e}_x - \sin \gamma \; \hat{e}_y + \frac{z_2}{D_{p2}} \hat{e}_z \quad , \tag{2.43}$$

where $D_{p2} = \left[(x_2-x_1)^2 + (y_2-y_1)^2\right]^{1/2}$ and γ is the angle between the x-axis and the projection of $\vec{R}_2$ onto the x-y plane. Consequently, the inner product $\hat{R}_2 \cdot \vec{r}$ can be expressed as follows:

$$\hat{R}_2 \cdot \vec{r} = a \cos (\phi+\psi+\gamma) + \frac{z \, z_2}{D_{p2}} \quad . \tag{2.44}$$
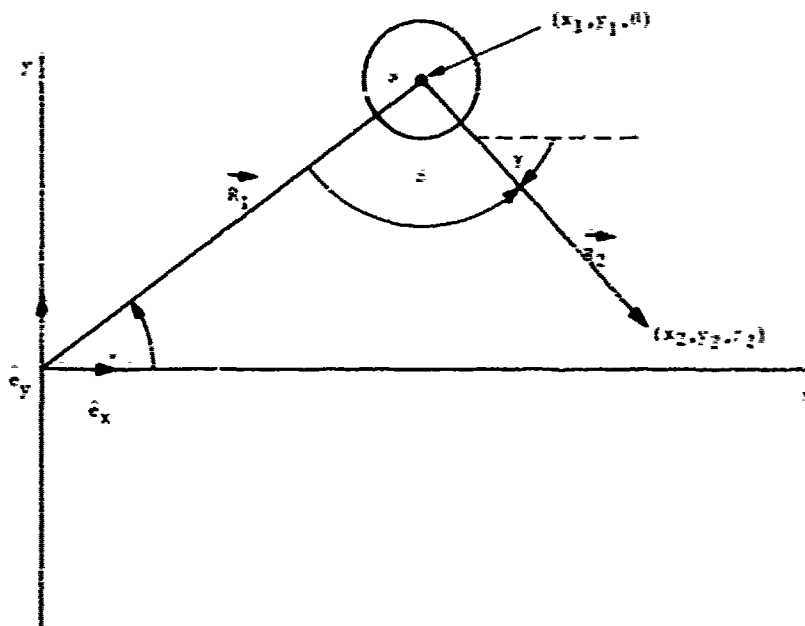
Figure 2-2. Geometry of the Cylinder Scattering Problem

Referring to Figure 2-2, we note that the following identity holds among the angles ϕ, β, and γ:

$$(\phi + \gamma) = \pi - \beta .\qquad(2.45)$$

Substituting Equation (2.45) into (2.44), we obtain the following results:

$$\hat{R}_2 \cdot \vec{r} = -a \cos (\phi - \beta) + \frac{z z_2}{D_{p2}} .\qquad(2.46)$$

The scattering integral (2.6) can now be evaluated quite readily by using the expressions for $\vec{H}_i$, $\hat{n}$, and $\hat{R}_2 \cdot \vec{r}$ given, respectively, in Equations (2.41), (2.42), and (2.46). The integrations are performed with respect to ϕ ($\pi/2 \leq \phi \leq 3\pi/2$) and z ($-h \leq z \leq +h$). The parameter h is the height of the cylinder and the range of the z integration is from -h to +h to take into account the image of the cylinder in the ground plane. We find

15

that for small angles of elevation ($D_{p2} \gg z_2$), $\vec{E}_s$ is polarized essentially parallel to the ground plane and that its magnitude, E_s, is given by:

$$E_S = \frac{ik}{\pi} E_o f(\varphi) \frac{e^{ik(R_1 + R_2)}}{R_1 R_2} \quad a\, h \left[\text{sinc } k\, h \left[\frac{H}{D_{p1}} - \frac{z_2}{D_{p2}} \right] - \right.$$

$$\left. \text{sinc } k\, h \left[\frac{H}{D_{p1}} + \frac{z_2}{D_{p2}} \right] \right] \cdot I(\beta) \quad , \tag{2.47}$$

where

$$I(\beta) = - \int_{-\pi/2}^{3\pi/2} \cos (\varphi - \beta)\, e^{2ika \cos \beta/2 \cos (\varphi - \beta/2)}\, d\varphi \quad . \tag{2.48}$$

The integral $I(\beta)$ can be expressed as an infinite series of Bessel functions as follows:

$$I(\beta) = - \pi i \cos \beta/2\, J_1(v) + 2 \cos^2 \beta/2\, J_0(v)$$

$$- \frac{\sin \beta}{ka(1 + \cos\beta)} \sin [ka \sin \beta]$$

$$- 2 \cos \beta/2 \sum_{n=1}^{\infty} J_{2n}(v) \left[\frac{\cos (2n-1)\beta/2}{2n-1} - \frac{\cos (2n+1)\beta/2}{2n+1} \right] , \tag{2.49}$$

where $v = 2ka \cos \beta/2$ and J_n is the Bessel function of order n. A very efficient subroutine has been developed for calculating $I(\beta)$ to any desired degree of accuracy using the above series representation.

It should be noted that Equation (2.47) represents the physical optics approximation to the scattered field produced by a right, circular cylinder and, consequently, is only valid when $a \gg \lambda$ ($ka \gg 1$).

16

To illustrate the predictions of our cylinder model, we have plotted in Figures 2-3 and 2.4 the microampere deviations (static and dynamic) along the centerline of a runway caused by a cylinder 80 f et in diameter and 50 feet high whose center is located 3260 feet down the runway from a V-Ring localizer and 470 feet off the runway centerline. The abscissa in each figure represents distance from the localizer. The aircraft is assumed to be executing level flight at an altitude of 50 feet.
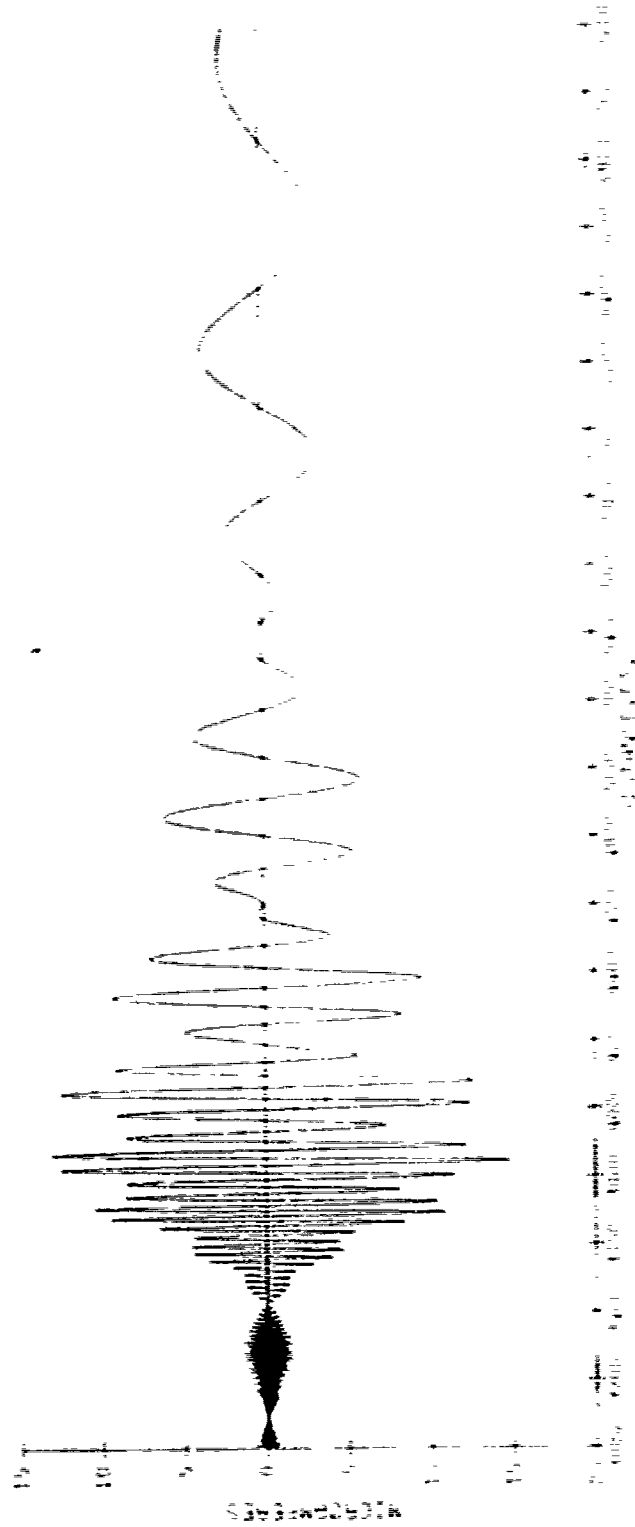
Figure 2-3. On Course CDI Due to a Cylinder 80 Feet In Diameter, 50 Feet
High, Centered at (3260', 470'). Static Response

18
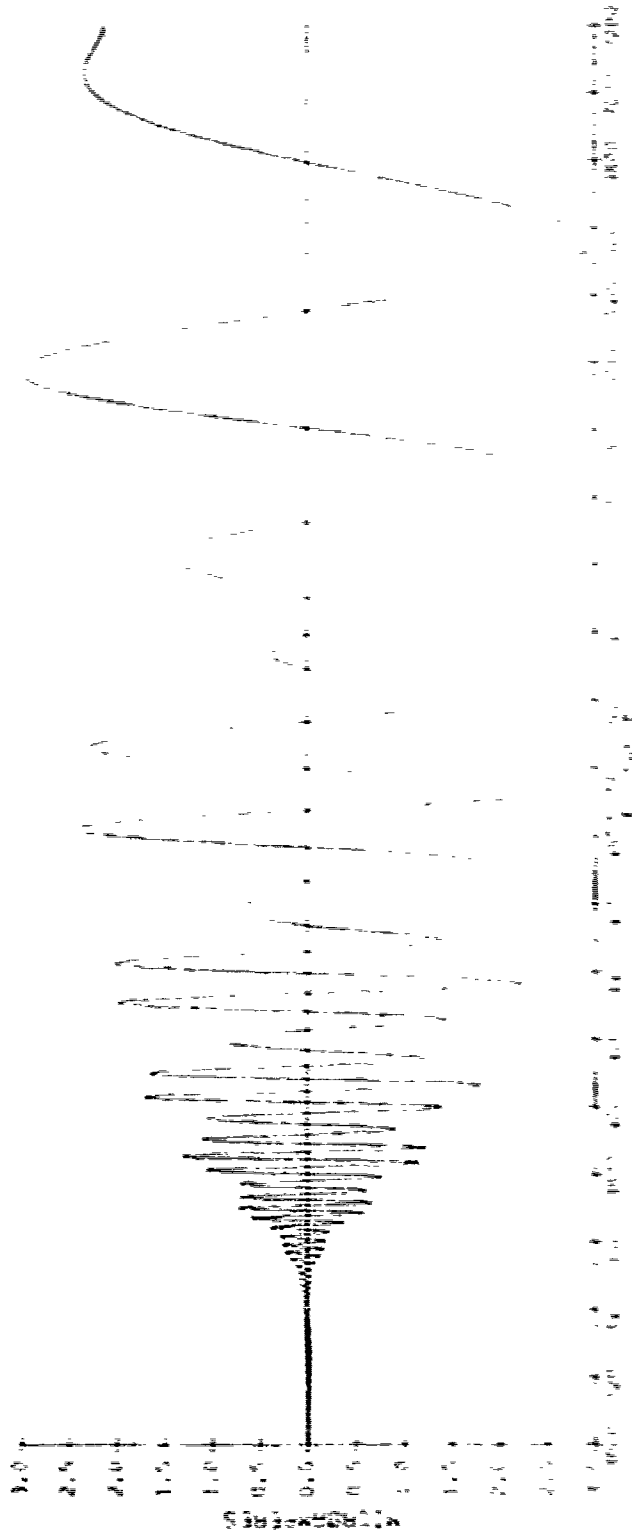
Figure 2-4. On Course CDL Due to a Cylinder 80 Feet in Diameter, 50 Feet
High, Centered at (3260', 470°). Dynamic Response

19

3. GLIDE SLOPE TERRAIN SCATTERING

3.1 INTRODUCTION

The majority of ILS glide slope antenna arrays currently in use are of the image variety. Consequently, the quality of the guidance information provided by these arrays is strongly dependent upon the characteristics of the surrounding terrain. In this report, a mathematical model is developed for predicting the distortions in glide slope antenna patterns produced by certain types of large scale terrain irregularities. Results are presented illustrating glide slope performance for some idealized terrain configurations.

3.2 THEORY

The vertical antenna pattern of an image-type glide slope array is determined by the interference between the direct and ground reflected radiation. The ground reflected or scattered radiation is generated by the charges and currents induced in the ground by the incident radiation from the glide slope array. For simplicity, we will assume that the ground plane is perfectly conducting. For a perfect conductor, the surface current density $\vec{K}$ is given by:

$$\vec{K} = \hat{n} \times \vec{H} \quad , \tag{3.1}$$

where $\hat{n}$ is the unit normal pointing out of the ground and $\vec{H}$ is the total magnetic field:

$$\vec{H} = \vec{H}_i + \vec{H}_s \quad , \tag{3.2}$$

where $\vec{H}_i$ denotes the incident and $\vec{H}_s$ denotes the scattered magnetic field.

Given the surface current density $\vec{K}$ on the ground, the scattered field $\vec{H}_s$ at a receiver above ground is given by the following surface integral:

20

$$\vec{H}_s(\vec{r}_1) = \frac{1}{4\pi} \int_S \vec{K}(\vec{r}) \times \vec{\nabla}G (\vec{r}_1, \vec{r}) \, ds \quad . \tag{3.3}$$

Here $\vec{r}_1$ and $\vec{r}$ denote, respectively, the position vector of the receiver and the position vector of an arbitrary source point on the ground plane S relative to some origin of coordinates. The two-point Green's Function $G(\vec{r}_1, \vec{r})$ is given by

$$G(\vec{r}_1, \vec{r}) = \frac{e^{ik|\vec{r}_1 - \vec{r}|}}{|\vec{r}_1 - \vec{r}|} \quad , \tag{3.4}$$

where $k = 2\pi/\lambda$ and λ is the wavelength of the incident radiation.

To specify the current density $\vec{K}$, we will adopt here the same physical optics model used in Reference 1 for treating high frequency scattering by perfect conductors. Specifically, we will assume that on those portions of the ground not directly illuminated by the array, $\vec{K}$ is identically zero and that on those portions of the ground which are directly illuminated, $\vec{K}$ is given by twice the tangential component of the incident magnetic field:

$$\vec{K} \equiv 0 \text{ on } S_- \quad , \tag{3.5}$$

$$\vec{K} = 2(\hat{n} \times \vec{H}_i) \text{ on } S_+ \quad , \tag{3.6}$$

where S_- and S_+ denote, respectively, the unilluminated and illuminated portions of the ground plane S. The two types of regions are illustrated in Figure 3-1. The current distribution given in Equations (3.5) and (3.6) should be reasonably accurate when the characteristic dimensions of the terrain irregularities are large compared to the wavelength λ. Substituting Equations (3.5) and (3.6) into Equation (3.3), we obtain the following approximate expression for the scattered magnetic field at the receiver point $\vec{r}_1$:

$$\vec{H}_s(\vec{r}_1) = \frac{1}{2\pi} \int_{S_+} \left[\hat{n}(\vec{r}) \times \vec{H}_i(\vec{r}) \right] \times \vec{\nabla}G (\vec{r}_1, \vec{r}) \, ds \quad . \tag{3.7}$$

21
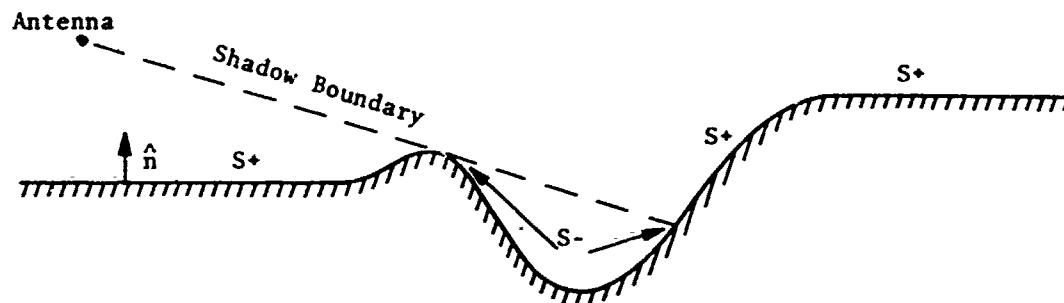
Figure 3-1. Cross Section of Terrain Showing Illuminated
and Unilluminated Regions

In general, the evaluation of the integral in Equation (3.7)
for an arbitrarily irregular ground plane is a prohibitively time-
consuming task even for the most rapid digital computer. However,
terrains characterized by irregularities which vary only along one
coordinate axis can be treated with relative ease. Consequently,
we will confine our attention at present to such one-dimensional
ground planes. Specifically, the touchdown point on the center-
line of the runway will be chosen as the origin of coordinates 0.
The z-axis is chosen to be the vertical axis passing through 0 and
pointing out of the ground while the x- and y-axes lie in the
horizontal plane whose normal parallels the z-axis. The x-axis
points along the centerline of the runway while the y-axis is
perpendicular to the centerline. The one-dimensional irregular-
ities are assumed to vary only with x. That is to say, the equa-
tion of the surface of the ground is of the form $z = f(x)$ and is
independent of variations in y.

Consider now the problem of a horizontal dipole mounted above
such a ground plane and oriented parallel to the y-axis, the
invariant axis of the terrain irregularities. This problem is of

22

fundamental importance since the majority of glide slope antenna systems consist of arrays of such dipoles. The geometry of a typical problem is illustrated in Figure 3-2. In Figure 3-2, the y-axis points into the page. Since the terrain is assumed to be y-invariant, the entire ground plane can be generated by projecting the cross section depicted in Figure 3.2 in the y-direction from $-\infty$ to $+\infty$.

To calculate the scattered field $\vec{H}_s$, generated by a given terrain contour, the ground surface is first divided into a number of connected planar sections which extend from $-\infty$ to $+\infty$ in the y-direction.[2] The side view of such a section is represented by the darkened segment of the contour depicted in Figure 3-2. The points (x_{01}, z_{01}) and (x_{02}, z_{02}) represent the end points of the section. The length L of a given segment is so chosen that the unit normal $\hat{n}$ is essentially constant for $x_{01} \leq x \leq x_{02}$ and $z_{01} \leq z \leq z_{02}$.
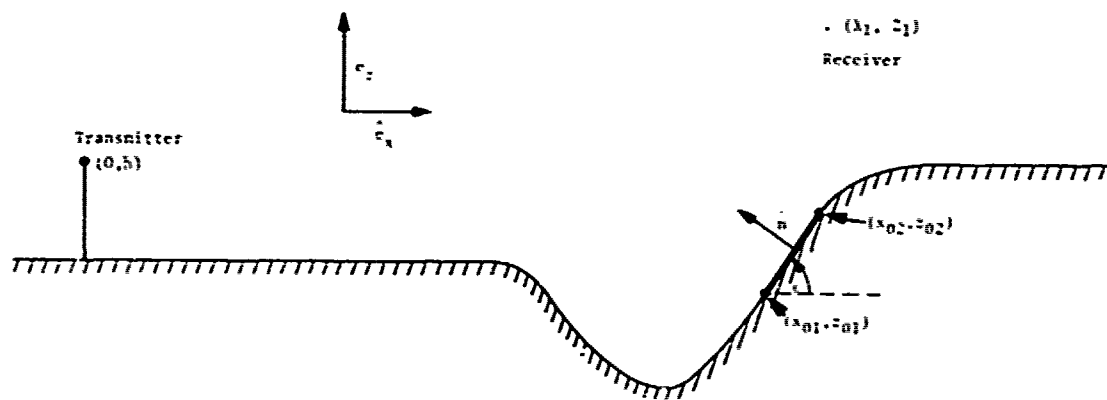
Figure 3-2. Geometry of a Typical One-Dimensional Ground Reflection Problem

23

$$L = \left[(x_{02}-x_{01})^2 + (z_{02}-z_{01})^2\right]^{1/2} \quad . \tag{3.8}$$

Once the contour has been segmented into these planar sections, Equation (3.7) can be applied to each section and the total scattered field $\vec{H}_s$ can then be obtained by summing the contributions from all the sections. We will therefore concentrate upon obtaining an expression for the contribution to the total scattered field $\vec{H}_s$ from a typical planar segment such as the one depicted in Figure 3.2. It will be assumed that only those segments which lie between the transmitter and receiver contribute to $\vec{H}_s$.

Let $\vec{h}_s$ denote the contribution to $\vec{H}_s$ from the planar section shown in Figure 3.2:

$$\vec{h}_s(\vec{r}_1) = \frac{1}{2\pi} \int \left[\hat{n} \times \vec{H}_i(\vec{r})\right] \times \vec{\nabla} G\ (\vec{r}_1,\vec{r})\ ds \quad , \tag{3.9}$$

where the integral is carried out over the surface of the segment (cf. Eq. (3.7)). Let $\hat{e}_x$, $\hat{e}_y$, and $\hat{e}_z$ denote, respectively, the unit vectors in the x, y, and z directions. In terms of these unit vectors, the unit normal $\hat{n}$ is given by:

$$\hat{n} = -\sin \epsilon\ \hat{e}_x + \cos \epsilon\ \hat{e}_z \quad , \tag{3.10}$$

where ϵ is the angle between the planar section and the x-axis (cf. Fig. 3.2). The x,z coordinates of the transmitting dipole and the receiver are denoted by (0,h) and (x_1,z_1), respectively. For simplicity, we will assume that the receiver is above the centerline of the runway so that

$$y_1 = 0. \tag{3.11}$$

The y displacement of the center of the transmitting dipole will be denoted by y_a. Glide slope arrays are generally located several hundred feet from the centerline of the runway.

The incident magnetic field $\vec{H}_i$ produced by the transmitting dipole is given in terms of the volume current density $\vec{J}$ in the dipole by the following formula (Reference,[1] Equation (2.23)).

$$\vec{H}_i(\vec{r}) = \frac{1}{4\pi} \int \left(\vec{J}(\vec{r}') \times \vec{\nabla}'G(\vec{r},\vec{r}')\right) dv' \quad , \tag{3.12}$$

24

where $\vec{\nabla}'$ operates on the primed coordinates. For simplicity, we will assume that all dimensions of the dipole are small compared with the wavelength λ. This assumption is not strictly valid since the dipoles which make up most glide slope arrays are $\lambda/2$ in length. However, the assumption of electrical smallness simplifies the calculations enormously and besides, the exact form of the dipole's azimuthal radiation pattern is not really relevant since we are concerned here with the vertical radiation patterns of glide slope arrays. Consequently, we will assume, for simplicity, that the transmitter is a point dipole:

$$\vec{J}(\vec{r}') = J_o \, \hat{e}_y \, \delta(x') \, \delta(y'-y_a) \, \delta(z'-h) \quad . \tag{3.13}$$

where J_o is some constant and as noted previsously, y_a is the displacement of the dipole from the centerline of the runway. The δ-functions are just the Dirac delta functions. We will make the further assumption that the planar section is many wavelengths distant from the transmitter so that to a good approximation, $\vec{\nabla}'G \, (\vec{r},\vec{r}')$ can be written as follows:

$$\vec{\nabla}'G \, (\vec{r},\vec{r}') \approx - \, ik \, \frac{(\vec{r}-\vec{r}')}{|\vec{r}-\vec{r}'|} \, \frac{e^{ik|\vec{r}-\vec{r}'|}}{|\vec{r}-\vec{r}'|} \quad . \tag{3.14}$$

Substituting Equations (3.13) and (3.14) into Equation (3.12), we obtain the following expression for the incident magnetic field $\vec{H}_i(\vec{r})$:

$$\vec{H}_i(\vec{r}) = \frac{ikJ_o}{4\pi} \, \frac{e^{ikD}}{D^2} \left[x \, \hat{e}_z - (z-h) \, \hat{e}_x \right] \quad , \tag{3.15}$$

where $\vec{r} = x \, \hat{e}_x + y \, \hat{e}_y + z \, \hat{e}_z$ and D is defined as follows:

$$D = \left[x^2 + (y-y_a)^2 + (z-h)^2 \right]^{1/2} \quad . \tag{3.16}$$

Equations (3.10) and (3.16) can now be substituted into Equation (3.9) and the magnetic field $\vec{h}_s$ at the receiving point $\vec{r}_1 = x_1 \, \hat{e}_x + z_1 \, \hat{e}_z$ due to the single planar section of terrain

evaluated. It will be assumed that the receiver is many wavelengths distant from the terrain segment so that $\vec{\nabla}G\,(\vec{r}_1,\vec{r})$ can be written approximately as follows:

$$\vec{\nabla}G\,(\vec{r}_1,\vec{r}) \approx -\,ik\,\frac{(\vec{r}_1-\vec{r})}{|\vec{r}_1-\vec{r}|}\,\frac{e^{ik|\vec{r}_1-\vec{r}|}}{|\vec{r}_1-\vec{r}|}\;. \qquad (3.17)$$

Actually, only the z-component of $\vec{h}_s$ need be calculated since glide slope receivers respond primarily to this component. The z- component of $\vec{h}_s$ will be denoted by h_{sz}. Substituting Equations (3.10), (3.15), and (3.17) into Equation (3.9), we obtain the following expression for h_{sz} at the receiver:

$$h_{sz}(\vec{r}_1) = -\,\frac{k^2 J_o}{8\pi^2}\int \frac{(x_1-x)(x\,\sin\varepsilon - (z-h)\cos\varepsilon)}{D^2\,R^2}\,e^{ik(D+R)}ds, \qquad (3.18)$$

where $R = \left[(x_1-x)^2 + y^2 + (z_1-z)^2\right]^{1/2}$. The element of area ds in (3.18) is equal to dy dη, where η is a variable ranging from 0 to L along the surface of the planar section of terrain perpendicular to the y-axis. The x- and y-coordinates of a point on the surface of the planar section can be expressed in terms of η as follows (cf. Fig. 3-2):

$$x = x_{01} + \eta\,\cos\varepsilon \;,\quad 0 \le \eta \le L \;, \qquad (3.19)$$

$$z = z_{01} + \eta\,\sin\varepsilon \;,\quad 0 \le \eta \le L \;, \qquad (3.20)$$

Substituting Equations (3.19) and (3.20) into (3.18), we find that:

$$h_{sz}(\vec{r}_1) = \frac{k^2 J_o}{8\pi^2}\left[(z_{01}-h)\cos\varepsilon - x_{01}\sin\varepsilon\right]$$

$$\int_0^L \int_{-\infty}^{+\infty} \frac{(x_1-x_{01}-\eta\cos\varepsilon)}{D^2\,R^2}\,e^{ik(D+R)}dy\,d\eta \;, \qquad (3.21)$$

where D and R are expressed as functions of the variables of integration y and η as follows:

$$D = \left[(x_{01}+\eta \cos \varepsilon)^2 + (y-y_a)^2 + (z_{01}-h+\eta \sin \varepsilon)^2\right]^{1/2} \quad , \quad (3.22)$$

$$R = \left[(x_1-x_{01}-\eta \cos \varepsilon)^2 + y^2+(z_1-z_{01}-\eta \sin \varepsilon)^2\right]^{1/2} \quad . \quad (3.23)$$

The integration with respect to y can be performed approximately using the method of stationary phase leaving only an integral with respect to η to be evaluated numerically:[2]

$$h_{sz}(\vec{r}_1) = \frac{k^2 J_o}{\delta_z^2} \left[(z_{01}-h)\cos \varepsilon - x_{01} \sin \varepsilon\right] \lambda^{1/2} e^{i\pi/4} I \quad , \quad (3.24)$$

where

$$I = \int_0^L e^{ikF(\eta)} G(\eta) \, d\eta \quad , \quad (3.25)$$

and F and G are defined as follows:

$$A = \left[(x_1-x_{01}-\eta \cos \varepsilon)^2 + (z_1-z_{01}-\eta \sin \varepsilon)^2\right]^{1/2} \quad ,$$

$$B = \left[(x_{01}+\eta \cos \varepsilon)^2 + (z_{01}-h+\eta \sin \varepsilon)^2\right]^{1/2} \quad ,$$

$$C = \left[1 + \frac{y_a^2}{(A+B)^2}\right]^{1/2} \quad , \quad D = CB, \quad R = CA,$$

$$S = \frac{1}{C^3}\left(\frac{1}{A} + \frac{1}{B}\right) \quad ,$$

$$F = C(A+B) \quad ,$$

$$G = \frac{x_1 - x_{01} - \eta \cos \varepsilon}{D^2 R^2 S^{1/2}} \quad . \quad (3.26)$$

27

The z-component of the total scattered magnetic field at the receiver is obtained by summing up the contributions h_{sz} from all of the illuminated planar sections lying between the transmitter and receiver. Symbolically, this result can be expressed as follows:

$$H_{sz} = \sum h_{sz} \; . \tag{3.27}$$

The contribution h_{sz} from each section is calculated using Equations (3.24), (3.25) and (3.26), the integral in (3.25) being performed numerically.

The z-component of the total magnetic field (direct plus scattered) at the receiver is given by (cf. Equation (3.15)):

$$H_z = \frac{ikJ_o}{4\pi} \frac{e^{ikR_1}}{R_1^2} x_1 + H_{sz} \; , \tag{3.28}$$

where $R_1 = \left[x_1^2 + y_a^2 + (z_1-h)^2 \right]^{1/2}$. The first term in Equation (3.28) is just the z-component of the expression for $\vec{H}_i$ given in Equation (3.15) evaluated at the receiver point $(x_1, 0, z_1)$. To calculate the vertical radiation pattern, it is convenient to use as an origin of coordinates the point $(0, y_a, 0)$, which is the point on the ground directly below the antenna. Let R_0 denote the distance from this point to the receiver:

$$R_0 = \left[x_1^2 + y_a^2 + z_1^2 \right]^{1/2} \; . \tag{3.29}$$

We will assume that the receiver is sufficiently far away from the transmitter so that the amplitude factor R_1^{-2} in (3.28) can be replaced by R_0^{-2}. Under this assumption, Equation (3.28) can be rewritten as follows:

$$H_z = \frac{kJ_o}{4\pi} \frac{e^{ikR_0}}{R_0^2} x_1 \left[ie^{ik(R_1-R_0)} + \frac{4\pi}{kJ_o} \frac{R_0^2}{x_1} e^{-ikR_0} H_{sz} \right] \; . \tag{3.30}$$

28

The expression in brackets in Equation (3.30) represents the vertical radiation pattern $P(\phi)$ of the dipole-terrain system:

$$P(\phi) = i\, e^{ik(R_1-R_0)} + \frac{4\pi}{kJ_0}\, \frac{R_0^2}{x_1}\, e^{-ikR_0}\, H_{sz} \quad . \tag{3.31}$$

The angle ϕ is just the elevation angle of the vector $\vec{R}_0 = x_1\,\hat{e}_x + y_3\,\hat{e}_y + z_1\,\hat{e}_z$ relative to the x-y plane:

$$\phi = \tan^{-1}\left(z_1/(x_1^2 + y_a^2)^{1/2}\right) \quad . \tag{3.32}$$

For an array of such dipoles, one would calculate a $P(\phi)$ for each element and then sum up these individual patterns to obtain the composite pattern of the array-terrain system.

3.5 NUMERICAL RESULTS

In this section, we present some of the preliminary numerical results which have been obtained using the formalism developed in the preceding section.

In Figure 3-3, we have plotted the magnitude of the sideband-only pattern of a null reference glide slope array as a function of the angle of elevation ϕ assuming a perfectly flat ground plane. The glide slope wavelength λ was set at 3 feet and the height h of the sideband antenna was set at 30 feet (h=10λ). The dashed curve represents the ideal sideband-only pattern based upon image theory:

$$|P| = 2\,|\sin\,(20\pi\,\sin\,\phi)| \quad . \tag{3.33}$$

The solid curve represents the sideband-only pattern calculated using Equation (3.31). This pattern was calculated by summing the contributions from the first 5000 feet of ground plane. The close agreement between the two curves obviously indicates that 5000 feet of flat ground plane is quite sufficient to form the null reference SBO pattern.

As a further illustration of the predictions of our model, we have plotted in Figure 3-4 the magnitude of the sideband-only
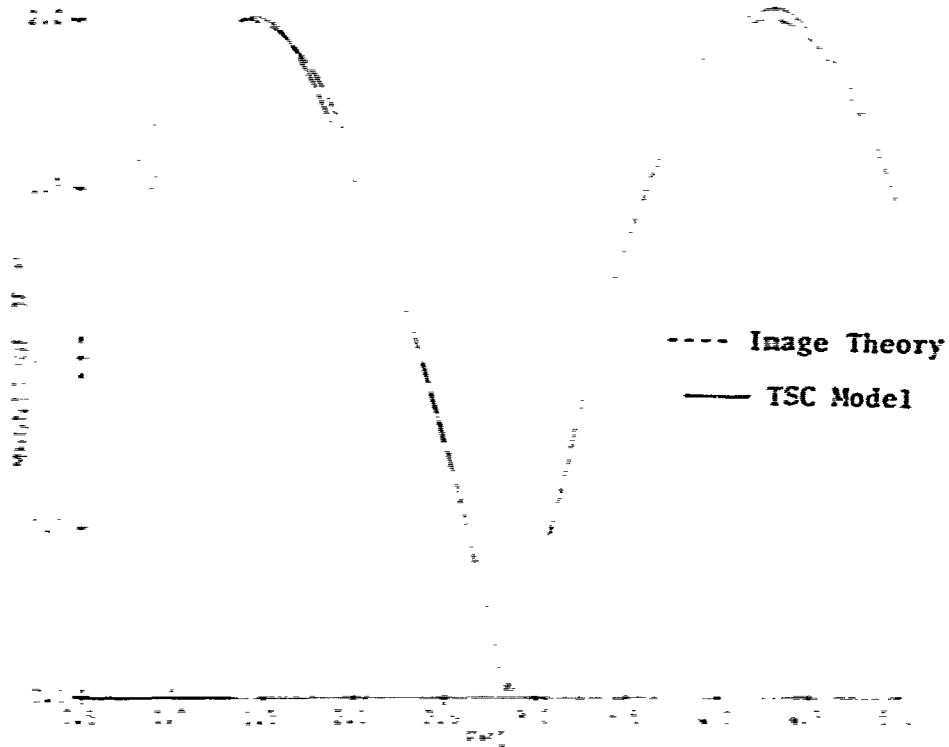
29

---- Image Theory

—— TSC Model

Figure 3-3. Magnitude of Null Reference Sideband-Only
Pattern

---- Image Theory

—— TSC Model
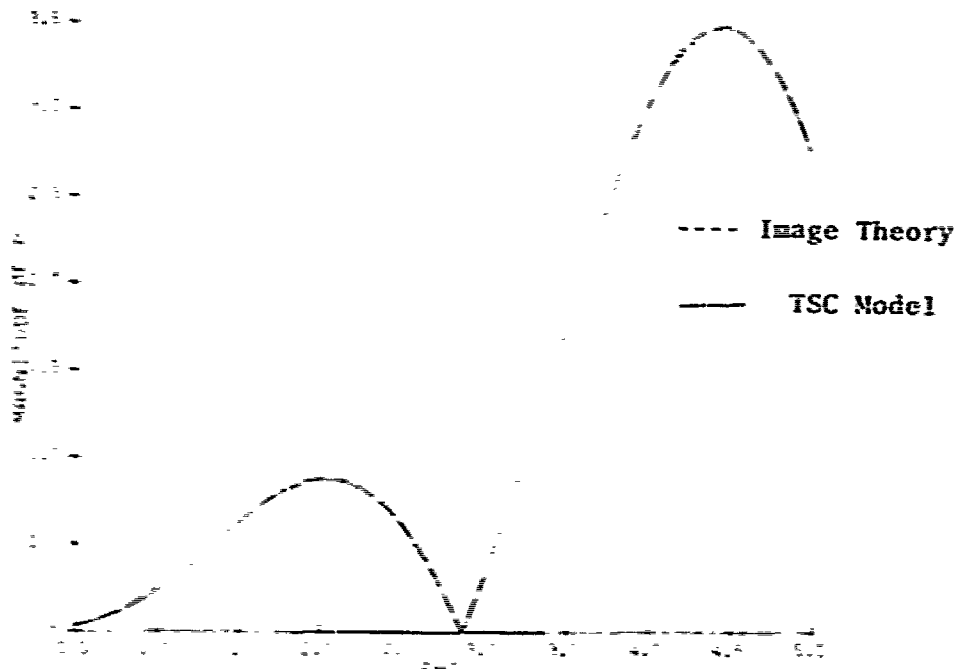
Figure 3-4. Magnitude of Capture Effect Sideband-
Only Pattern

30

pattern of a capture-effect array, again assuming a perfectly flat
ground plane. The capture-effect array consists of three dipoles
placed one above the other at heights which were set at 15, 30,
and 45 feet (5λ, 10λ, and 15λ). All three dipoles are fed sideband-
only signal with the following relative amplitudes: (-.5, 1.0,
-.5). The resulting array pattern according to image theory is
given by:

$$|P| = |2 \sin(20\pi \sin \phi) [1 - \cos(10\pi \sin \phi)]| \quad . \quad (3.34)$$

The dashed curve in Figure 3.4 represents the ideal image theory
pattern of Equation (3.34) while the solid line represents the
pattern obtained by applying Equation (3.31) to each antenna
element and then summing the individual patterns. This calculated
pattern represents the contributions from the first 5000 feet of
ground plane. As in the case of the null reference SBO pattern,
the agreement between the two curves is excellent.

Finally, to illustrate the predictions of our theoretical
model in the case of an irregular ground plane, we applied the
model equation of Section 3.2 to the terrain configuration depicted
in Figure 3.5.

Figure 3-5. Sample Siting Problem

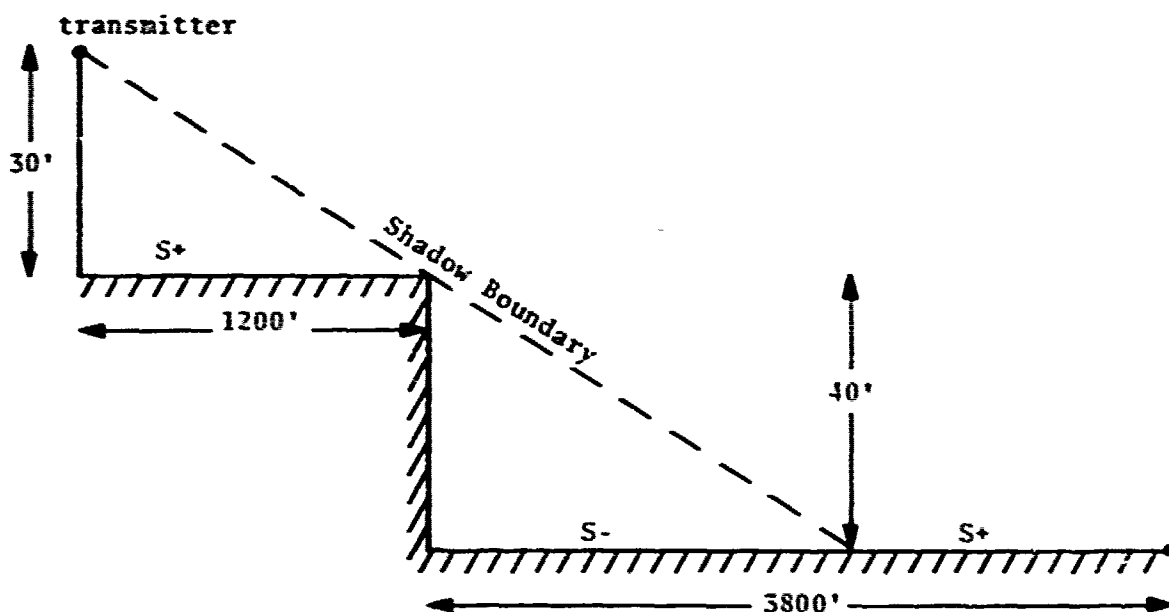Referring to Figure 3.5, which obviously is not drawn to scale, we note that the terrain in front of the antenna consists of 1200 feet of flat ground terminating in a 40-foot drop to a lower plateau which then extends out an additional 3800 feet. This type of siting problem was one of many suggested to us for investigation by the FAA. The sideband antenna of a null reference glide slope array is placed at a height of 30 feet (10λ) above the first plateau and, therefore, at height of 70 feet (23.3λ) above the lower plateau. In Figure 3-6, we have plotted the null reference SBO pattern for this terrain configuration as predicted by our model.

The pattern depicted in Figure 3.6 exhibits features which reflect the two effective antenna heights (30 feet and 70 feet) which arise because of the 40 foot drop-off. The nulls of a null reference SBO antenna pattern occur, according to image theory, at those values of the elevation angle ϕ which satisfy the following equation:

$$\sin (kh \sin \phi) = 0 , \qquad (3.35)$$

where h is the height of the antenna above the ground plane. For small values of ϕ, the first few nulls occur at the following angles:

$$\phi_n = \frac{n\lambda}{2h} , \ n = 0, 1, 2, \cdots . \qquad (3.35a)$$

For $\lambda = 3$ feet and h = 30 feet, the first few nulls occur at multiples of $2.86°$ while for h = 70 feet the first few nulls occur at multiples of $1.23°$. Referring to Figure 3.6, we note that the primary minimum occurs near $2.86°$, the glide path angle corresponding to the 30-foot antenna height. In addition, there is a shallower local minimum near $1.23°$, the glide path angle corresponding to the effective 70-foot antenna height. Note also that there is an inflection point near $2.46°$ which is twice the 70-foot glide path angle.

In summary, the main features of the pattern depicted in Figure 3.6 reflect contributions to the scattered field from the

first 1200 feet of ground plane for which the effective antenna
height is 30 feet (10λ). There are, however, secondary features
which clearly reflect contributions to the scattered field from
the 3800 feet of ground plane beyond the drop-off for which the
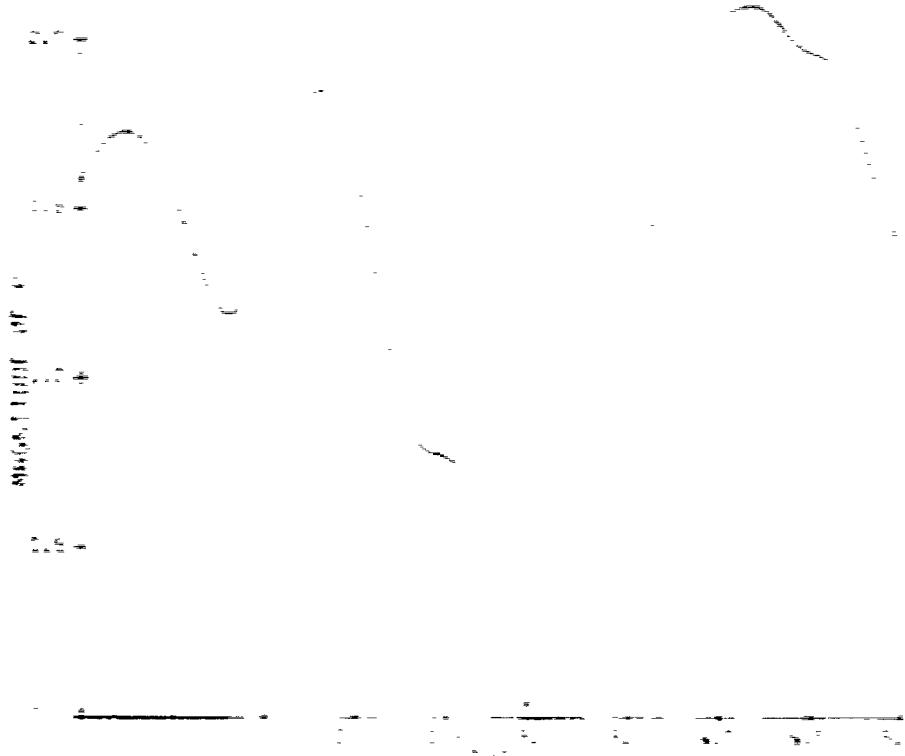effective antenna height is 70 feet (23.3λ).

Figure 3-6. Magnitude of Null Reference Sideband-Only
Pattern for the Terrain Shown in Figure 3-5

4. MODEL OF A PARABOLIC REFLECTOR LOCALIZER SYSTEM

4.1 INTRODUCTION

The introduction of the Texas Instruments (TI) wide aperture parabolic reflector localizer raises a question about the ability of the ILSLOC program[3] to properly predict the Course Deviation Indication (CDI) for arbitrary signal transmitting systems. The program has a provision for accepting measured course and clearance signal amplitudes to characterize arbitrary array patterns. This method assumes that the measured fields are generated by linear arrays elevated to a discrete height above the ground plane. For such a case there should be no anomalous phase variations between the carrier-plus-sidebands and sidebands-only signal components as azimuth angle is varied.

In contrast, the parabolic screen of the TI antenna represents a vertically-extended source with a vertical pattern which cannot be described by a discrete point image formula. Moreover, it is not clear that sidebands-only and carrier-plus-sidebands signals are generated so as to have a common center of phase. These considerations raised the question of whether the use of measured TI arrary patterns without detailed phase information would lead to incorrect results in CDI calculations.

To explore these questions, an approximate theoretical model of the TI wide aperture parabolic localizer system was developed. This model was then applied to the prediction of CDI for a potential installation at San Francisco International Airport and compared to predictions for the same installation based on measured patterns.

4.2 THE TEXAS INSTRUMENTS PARABOLIC ANTENNA SYSTEM

Figure 4-1 illustrates the positioning of the components of the TI localizer system. The radiating system consists of seven directional radiating elements and a parabolic reflecting screen. Three of the elements form the "directive" array and radiate
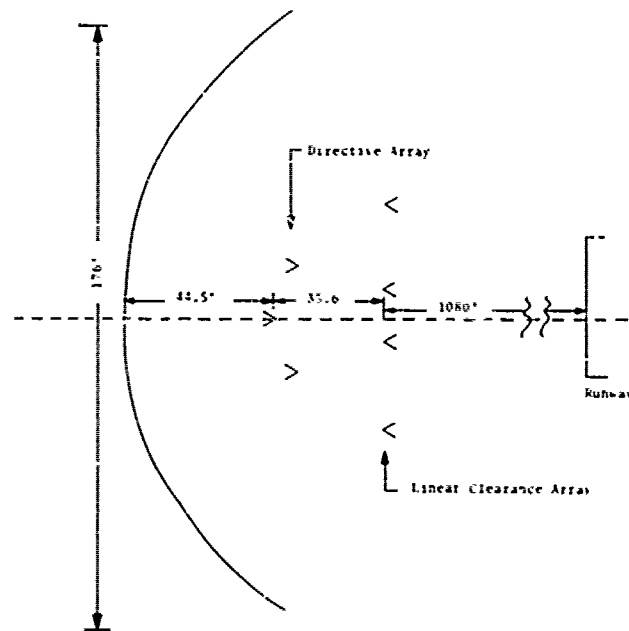
Figure 4-1. Sketch of Parabolic Localizer Layout

primarily by reflection from the screen. The remaining four elements are arranged in a linear array and are oriented so as to radiate directly to the landing approach path. The parabola has a focal length of 44.5 feet (5λ), an aperture of 176 feet (20λ) and a height of 18.5 feet (~2λ). The center element of the directive array, located at the parabolic focus, generates the course carrier plus sidebands signal. The course sidebands-only signal is radiated by the directive array side elements, which are placed slightly in back of the focal plane.

A detail of the spacing of the array elements is shown in Figure 4-2. Each element, except the center element of the directive array, consists of a radiator and a reflector. This type of antenna has been given the designation "V-frame" by the manufacturer. The center element of the directive array is of the same type with an additional component, a "director," to give it a narrower pattern. The pattern of the V-frame elements of the linear array, as deduced from graphs furnished by the manufacturer,

35
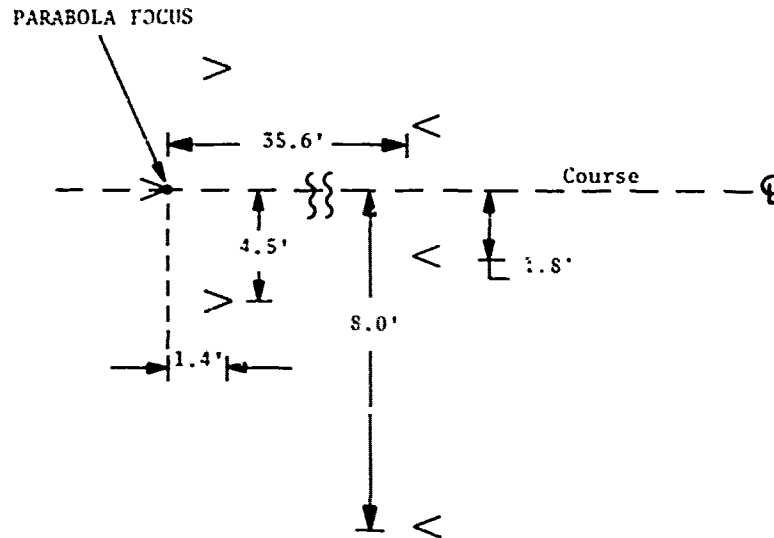
Figure 4-2. Detail of V-Frame Element Positioning

is tabulated in Table 4-1. The element patterns of the directive array are treated differently as will be indicated below.

The clearance signal is generated by the combination of the directive and linear arrays. The contribution of the center element of the directive array may be adjusted so that the clearance C+S signal has a near null on the course line. This has the virtue of enhancing the capture effect rejection of clearance multipath interference.

Patterns claimed by the manufacturer for a system so adjusted are shown in Figure 4-3. To achieve these patterns the signal amplitudes fed to the various elements of the directive and linear arrays are adjusted so that:

1. The on-course strength of the linear array C+S radiation is 10 dB below the course C+S signal from the directive array.

2. The clearance C+S of the directive array is adjusted to

TABLE 4-1   V-FRAME HORIZONT.   **RADIATION PATTERN**

Angle	Relative Amplitude		Angle	Relative Amplitude
0	1.000		70	.695
±10	.998		80	.630
±20	.976		90	.588
30	.954		100	.559
40	.912		110	.549
50	.842		120	.524
60	.772		150	.417
-	-		180	.455

cancel the linear array C+S signal on course.

3. The relative amplitudes fed the four elements of the linear array are:

C+S: 0.0   .33/0°   .33/0°   0.0

SO: .165/270° .33/270° .33/90°   .165/90°

4. The clearance SO signal radiated by the directive array is adjusted to equal the linear array SO signal at 5°. The resultant clearance signal radiation patterns are given in Figure 4-4.

4.5 MATHEMATICAL ANALYSIS OF REFLECTION FROM A PARABOLIC SCREEN

The radiation contributions of the four element linear array can be calculated in the usual way by standard array equations. In order to generate the radiation pattern of the directive array, we require approximate formulas for diffraction by the parabolic screen. The screen is formed by a closely spaced horizontal wire grid. We assume that it may be treated as a solid perfect reflector
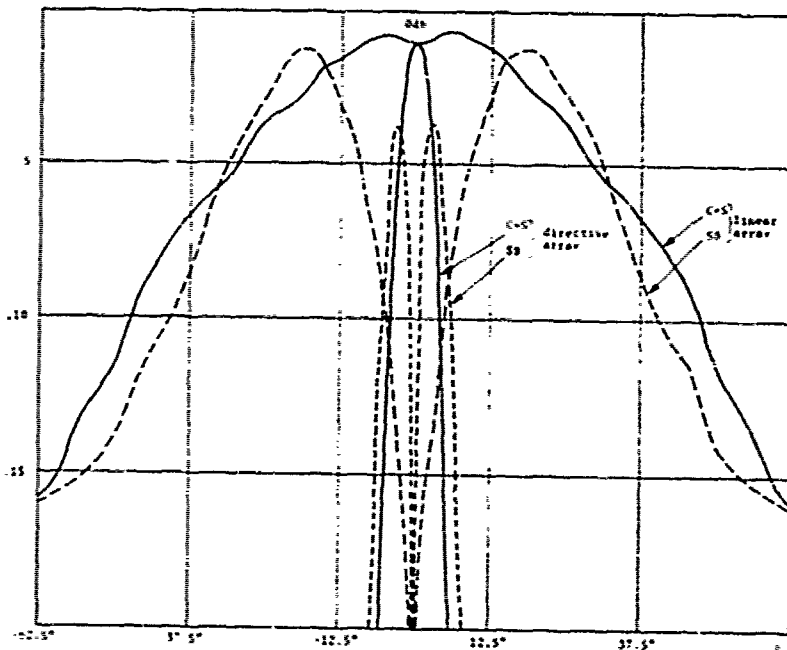
Figure 4-3.   Directive and Linear Array Clearance
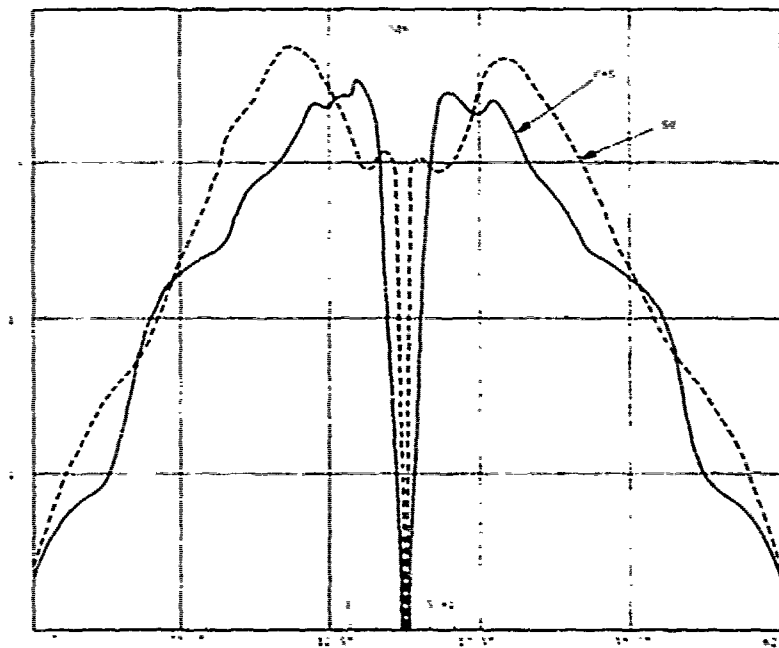Radiation Patterns

Figure 4-4.   Combined Clearance Radiation Pattern

38

to the horizontally polarized radiation of the directive array. The elements of the array are treated as point source. elevated 9 feet above the ground plane and positioned as shown in Figure 4-2.

To develop the approximate far-field radiation pattern for a point source reflected by the parabola, we adopt the coordinate system shown in Figure 4-5. The reference origin is established at the point where the parabola focal line intercepts the ground plane. From this point the vector $\vec{r}'$ gives the position of the source element; the vector $\vec{r}$ gives the observation point, and the vector r_p defines a variable point on the parabola surface. It is always considered that $|\vec{r}| \gg |\vec{r}_p| \gg |\vec{r}'|$. The unit normal reference vector on the parabola $\hat{n}$ is taken to point <u>away</u> from the local center of curvature.

The reflected electric field amplitude $\vec{E}(\vec{r})$ at the observation point is taken to be given by a vector Kirchhoff integral:[4]

$$\vec{E}(\vec{r}) = \frac{i}{\lambda} \sqrt{\frac{\mu}{\varepsilon}} \, \hat{r} \times \left[\hat{r} \times \int (\hat{n} \times \vec{H}_i) \, \psi \, dS \right] . \qquad (4.1)$$

Here $\vec{H}_i(\vec{r}_p)$ is the magnetic field amplitude incident on the parabola due to the source element, ψ is the Green's Function:

$$\psi = e^{ik|\vec{r}-\vec{r}_p|} \Big/ |\vec{r}-\vec{r}_p| \, , \qquad (4.2)$$

and dS is the increment of integration area. The integral in (4.1) can be recast using the radiation field relation:

$$\sqrt{\frac{\mu}{\varepsilon}} \, \vec{H}_i = \hat{n}_i \times \vec{E}_i \, , \qquad (4.3)$$

where $\hat{n}_i$ is a unit vector giving the direction of incidence and $\vec{E}_i(\vec{r}_p)$ is the incident electric field amplitude. The integral then becomes

$$\vec{E}(\vec{r}) = \frac{i}{\lambda} \, \hat{r} \times \left[\hat{r} \times \int \hat{n} \times (\hat{n}_i \times \vec{E}_i) \, \psi \, dS \right] . \qquad (4.4)$$

We assume that the incident electric field is horizontally polarized and may be expressed in the general form:
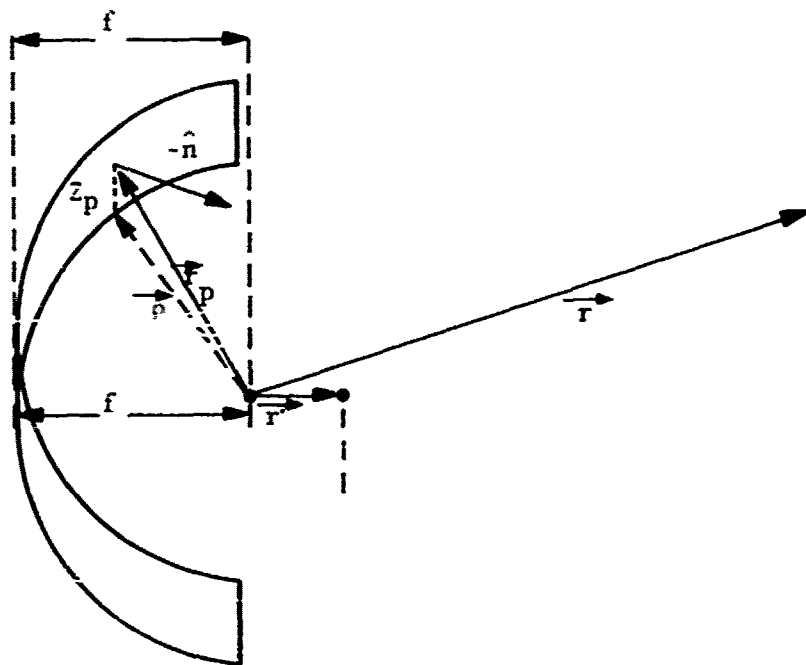
39

Figure 4-5. Coordinate Nomenclature for Parabolic
Screen Reflection Analysis

$$\vec{E}_i(\vec{r}_p) = \psi_s \, A(\hat{n}_i) \, \hat{n}_i \times \hat{k} \quad , \tag{4.5}$$

where

$$\psi_s = e^{ik|\vec{r}_p - \vec{r}'|} \Big/ |\vec{r}_p - \vec{r}'| \quad . \tag{4.6}$$

$A(\hat{n}_i)$ gives the field amplitude radiated by the source as a function of direction. Introduction of this form into (4.4) leads to a multiple-vector product which may be reduced under the assumptions that $\hat{n}$ is horizontal and $\hat{r}$ and $\hat{n}_i$ are nearly so:

$$\hat{r} \times \left(\hat{r} \times \left(\hat{n} \times \left(\hat{n}_i \times \left(\hat{n}_i \times \hat{k} \right) \right) \right) \right)$$

$$= \hat{r} \times \hat{k} \; \hat{r} \cdot \hat{n} \; - \; \hat{r} \times \hat{n}_i \; \hat{n}_i \cdot \hat{k} \; \hat{n} \cdot \hat{r}$$

$$+ \; \hat{r} \times \hat{n} \left(\hat{n}_i \cdot \hat{k} \; \hat{n}_i \cdot \hat{r} \; - \; \hat{r} \cdot \hat{k} \right)$$

$$= \hat{r} \times \hat{k} \; \hat{r} \cdot \hat{n} \quad . \tag{4.7}$$

This allows (4.4) to be written as

$$\vec{E}(\vec{r}) = \frac{i}{\lambda} \, \hat{r} \times \hat{k} \int d\mathfrak{z} \; \hat{r} \cdot \hat{n} \; A(\hat{n}_i) \; \psi_s \; \psi \quad . \tag{4.8}$$

We next simplify the arguments of the functions ψ_s and ψ, i.e. $|\vec{r}_p - \vec{r}'|$ and $|\vec{r} - \vec{r}_p|$, recalling the assumption $r' \ll r_p \ll r$. It is convenient to put $\vec{r}_p = \vec{\rho} + z_p \hat{k}$, with ρ the horizontal projection of $\vec{r}_p$, and then:

$$|\vec{r}_p - \vec{r}'| = \rho - \frac{\vec{r} \cdot \vec{\rho}}{\rho} + \frac{(z_p - z')^2}{2\rho} + \ldots \tag{4.9}$$

$$|\vec{r} - \vec{r}_p| = r - \hat{r} \cdot \vec{\rho} - z_p \, \hat{r} \cdot \hat{k} + \ldots \tag{4.10}$$

where terms such as $|\vec{r}'|^2 / \rho$ have been rejected as negligible. In order to factor the integrand of (4.8), we further simplify the product $\psi_s \, \psi$ after inserting the approximations above and we obtain:

41

$$\psi_s \psi = \frac{1}{\rho r} \, e^{ikr} \, e^{ik\left(\rho - \left(\hat{r} + \frac{\vec{r}'}{\rho}\right)\cdot\vec{\rho}\right)} \, e^{ik\left(z_p - z' - \rho\hat{r}\cdot\hat{k}\right)^2/2\rho} \quad . \tag{4.11}$$

Negligible terms have been introduced in the third exponential factor in order to complete the square appearing there. Since the vector $\vec{\rho}$ describes a point on a parabola, it satisfies the exact relations:

$$\rho_x = \frac{\rho_y^2}{4f} - f \tag{4.12}$$

$$\rho = \rho_x + 2f \quad . \tag{4.13}$$

In order to obtain a manageable integral, we need to make in certain places the approximation $\rho_x = -f$. The element of integration combined with the factor $\hat{r}\cdot\hat{n}$ can be reduced in the following manner:

$$dS \, \hat{r}\cdot\hat{n} = \hat{k} \cdot d\vec{\rho} \times \hat{r} \, dz_p$$

$$= \left((\hat{r})_y \, d\rho_x - (\hat{r})_x \, d\rho_y\right) dz_p$$

$$= \left((\hat{r})_y \, \frac{\rho_y}{2f} - (\hat{r})_x\right) d\rho_y \, dz_p \quad . \tag{4.14}$$

Incorporating these results into the integral (4.8), we obtain the form:

$$\vec{E}(\vec{r}) = \frac{i}{\lambda} \, \frac{e^{ik\left(r + (1+a_x)f\right)}}{r} \, \hat{r} \times \hat{k} \, F_H \, F_V \quad , \tag{4.15}$$

where

$$F_H = \int_{-2f}^{2f} d\rho_y \left[(\hat{r})_y \frac{\rho_y}{2f} - (\hat{r})_x\right] \frac{A(\hat{n}_i)}{\rho} \, e^{ik\left[(1-a_x)\frac{\rho_y^2}{4f} - a_y\rho_y\right]} \tag{4.16}$$

42

$$F_V = \int_0^{h_p} dz_p \; e^{i\frac{\pi}{2}\frac{2}{\lambda f}(z_p - z' - f\;\hat{r}\cdot\hat{k})^2} \tag{4.17}$$

$$\vec{a} = \hat{r} + \vec{r}'/f$$

$$= (a_x, a_y, a_z) \; . \tag{4.18}$$

The vertical integral F_V is a Fresnel integral which is easily put into standard form by introducing the variable

$$u = \sqrt{2/(\lambda f)}\;(z_p - z' - f\;\hat{r}\cdot\hat{k}) \; . \tag{4.19}$$

However, up to this point, this integral does not account for any reflections from the ground plane. Terms must be added to include the image of the source in the incident field and the image of the screen in the reflected field. With these terms F_V can be reduced to:

$$F_V = \int_{-h_p}^{h_p} dz_p \left\{ e^{i\beta_V(z_p - z' - f\;\hat{r}\cdot\hat{k})^2} - e^{i\beta(z_p + z' - f\;\hat{r}\cdot\hat{k})^2} \right\} \tag{4.20}$$

with

$$\beta_V = k/2f \; .$$

The horizontal integral F_H is not as easily treated. We note, however, that if the expression $1-a_x$ is sufficiently small the quadratic term of the exponential can be ignored. This appears to be the case when the deviation angle from the course to the receiver is as much as $14°$. This is a large enough range to cover most of the sector in which the radiation of the directive array is significant. Therefore, we proceed by dropping the quadratic term of the exponent, which allows F_H to be treated as a Fourier integral. Putting $\rho = 2f$ and assuming an expansion of $A(\hat{n}_i)$:

$$A(\hat{n}_i) = A_0 + A_2(\rho_y/2f)^2 + \cdots \tag{4.21}$$

43

we have:

$$F_H = \int_{-1}^{1} du \left[(\hat{r})_y \, u - (\hat{r})_x \right] \left[A_0 + A_2 u^2 \right] e^{-i\beta_H u} \qquad (4.22)$$

where $u = \rho_y/(2f)$ and $\beta_H = k \, a_y$. Equations (4.15), (4.20) and
(4.22) are the basic relationships that were programmed to calcu-
late the field of a single antenna reflecting from a parabolic
screen. The parameters A_0 and A_2 are chosen so as to approximate
the angular patterns and relative amplitudes of the fields radiated
by the "V-frame" source elements.

One calculation is made for the carrier-plus-sidebands field
of the center element. Calculations for two elements placed
symmetrically off-center are combined to obtain the sidebands-only
field of the directive array. For the C+S field the A values are
taken to be $A_0 = 1$, $A_2/A_0 = -2.60$. For SO field, $A_2/A_0 = -1.92$
and A_0 is adjusted to obtain the proper "tailored" course width.
The integral in F_H is taken only over the ranges of u for which
$A_0 + A_2 u^2$ is positive to simulate the different V-frame pattern
widths of these two cases.

4.4   APPLICATION AND CONCLUSIONS

As indicated earlier, the above model for reflected radiations
from a parabolic screen has been applied to the prediction of
performance for a proposed installation on runway 28R at San
Francisco International Airport. In this instance, the tailored
course width is 5.8°. The combined theoretical patterns of the
directive and linear arrays derived from the model are as shown in
Figure 4-6. (See also Section 5.)

On the question of possible anomalous phase effects it can
be concluded that any such problems will occur in the vicinity
of 5-6° off course which is the capture-effect transition region.
From a check of the phases of the clearance field components
calculated with the model at 5.8°, it turns out that phase dif-
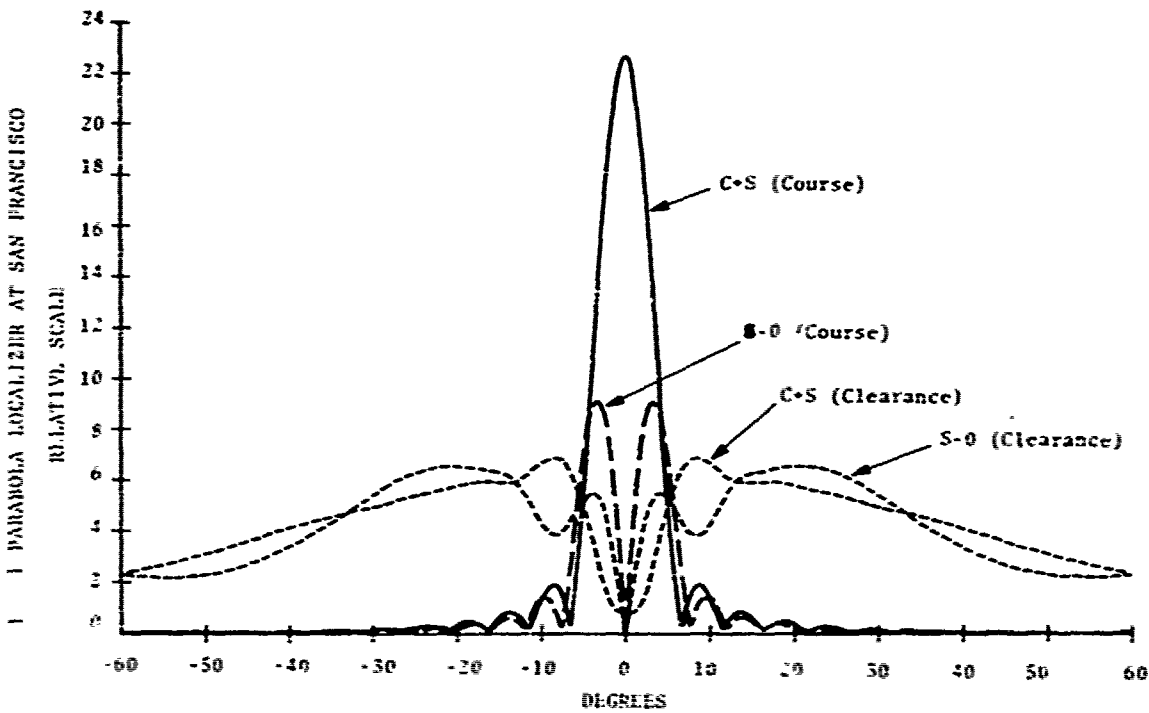ferences between the directive array and linear array contributions

Figure 4-6: Theoretical Course and Clearance
Signal Patterns

range up to about 6°. Such differences are not serious. To
confirm this, the theoretically calculated parabolic localizer
patterns were inputted to the ILSLOC program as measured patterns
with no assumed phase differences. The resulting orbit CDI com-
pared with the model generated orbit CDI shows no significant dif-
ference (Figure 4-7).

All of this suggests that the TI parabolic localizer signal
patterns can be adequately generated in the ILSLOC program from
measured data. If this approach is taken the vertical dependence
of the simulated radiation will correspond to a discrete antenna
height. Reduction of the theoretical vertical dependence (Equa-
tion (4.20)) in the limit of small elevation angles indicates that
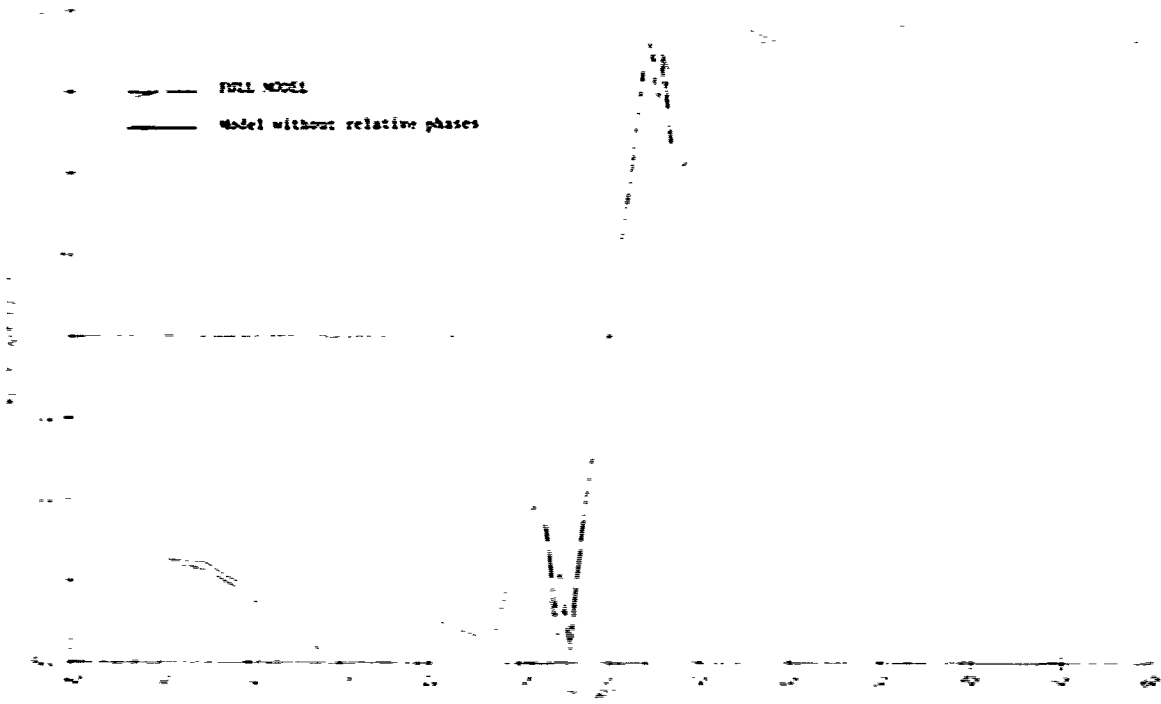the height of the V-frame elements above the ground plane is the
correct choice.

Figure 4-7. Orbit CDI Pattern According to
Theoretical Parabolic Localizer Model

46

5. APPLICATIONS OF ILS PERFORMANCE PREDICTION MODEL

5.1 INTRODUCTION

The Transportation Systems Center ILS localizer performance prediction model was used to predict ILS localizer performance at several different airports. Specifically, the model:

1. Was applied to Syracuse-Hancock International Airport to obtain model validation

2. Was used to determine which type of localizer was needed to produce acceptable course structure in the presence of a large 747 hangar located near runway 28 at the San Francisco Airport

3. Was used to predict what the ILS localizer performance would be if a proposed limited access roadway were to be constructed in front of the localizer antenna at the New Orleans Airport

4. Was used to determine comparative ILS localizer performance for a proposed airport layout at the Dallas/Fort Worth Airport site.

These varied applications of the model illustrate the potential usefulness of the model:

1. As an aid to airport planners and architects by being able to predict the effect a proposed airport layout has on ILS performance and suggesting possible modifications (e.g., Dallas/Fort Worth)

2. As an aid to particular airport managers in predicting the effect a proposed new hangar or roadway has on ILS performance and suggesting specific location or orientation modifications of the proposed structure for acceptable ILS performance (e.g., New Orleans)

3. As an aid to the FAA regions in deciding on the relative performance of different ILS localizer antenna candidates for runway instrumentation or runway upgrading (e.g.,

47

San Francisco and Syracuse Airports). Each of these
applications of the model will now be discussed (more
extensive information may be found in individual reports
previously issued).[5-8]

5.2 INPUT DATA REQUIRED

The input data to the computer program for these applications
follow the general format outlined below, (see Reference 3 for a
complete description and listing of the computer program).

The particular localizer antenna desired is chosen first. We
have the choice of a V-ring, 8-loop, waveguide; a measured pattern
(single or capture-effect system) and a theoretical pattern (single
or capture effect system). We then choose the transmitter fre-
quency (usually 110 MHz). We place the chosen antenna at the ori-
gin and input the distance between antenna and runway threshold.
This is used for both flight path orientation and for course width
determination. The antenna height above the ground is next required
as well as the flight path distance, the desired spacing between
sample points, the angle of approach of the aircraft, the glide
angle and the height of the aircraft at threshold. For an orbit
run, the starting and ending angle are input as well as the desired
angular spacing between sample points and the radius and height of
the orbit. The velocity of the aircraft is chosen next which is
used to calculate the Doppler effect on the receiver.

After inputting the antenna patterns used at the location
studied as well as the assumed trajectory of the aircraft, the
location and orientation of the derogating surfaces are next
delineated. The shape of the scatterer is input first, rectangular
or cylindrical, followed by the location coordinates of the scat-
terer. The angle made by the base of the object relative to the
runway centerline (orientation) is input next, followed by the angle
of tilt of the object and its width and height. Walls that are
too large are automatically divided into smaller ones based on a
minimum error criterion.

After the input of this data, the electric field at the surface of the scatterer due to the direct and ground reflected signals is calculated. Following this, the electric field at each point along the flight path, due to the direct, ground scattered and building scattered signals, is calculated. The program then loops back permitting the summation of the effects of many scatterers. Finally, the program calculates the CDI that would be seen at each receiver point.

The looping permits the repetition of a run with changes in some or all of the variables. For example, a run may be repeated with the same antenna but with a new set of scatterers or with the same set of scatterers but with a different antenna.

A second (mini) program takes the output tape generated by this main program and converts it to the observed CDI by simulating the effect of a low pass filter (to so-called "dynamic" results as opposed to the "static" or instantaneous CDI values obtained as output from the main program). The receiver time constant and aircraft speed must be inputted into this program.

Finally, a plotting routine program generates a variety of graphs of the static and dynamic CDI's as well as of the antenna patterns.

5.3 SYRACUSE-HANCOCK INTERNATIONAL AIRPORT

In the case of Syracuse-Hancock International Airport, flight test recordings were available against which the model could be compared. Syracuse Airport is an example of an airport with a moderately complex environment as shown in Figure 5-1, whose instrumented runway number 28 is FAA rated for Category I instrumented flights. Pictured in Figure 5-1 are a number of structures near runway 28, numbered from 1 to 18, which are sources of scattered ILS localizer radiation. Since the localizer radiation striking and being reflected from these structures makes an angle other than zero with the runway centerline, the radiation striking an aircraft receiver antenna which is on line with the runway centerline will contain unbalanced 150 Hz and 90 Hz modulations.
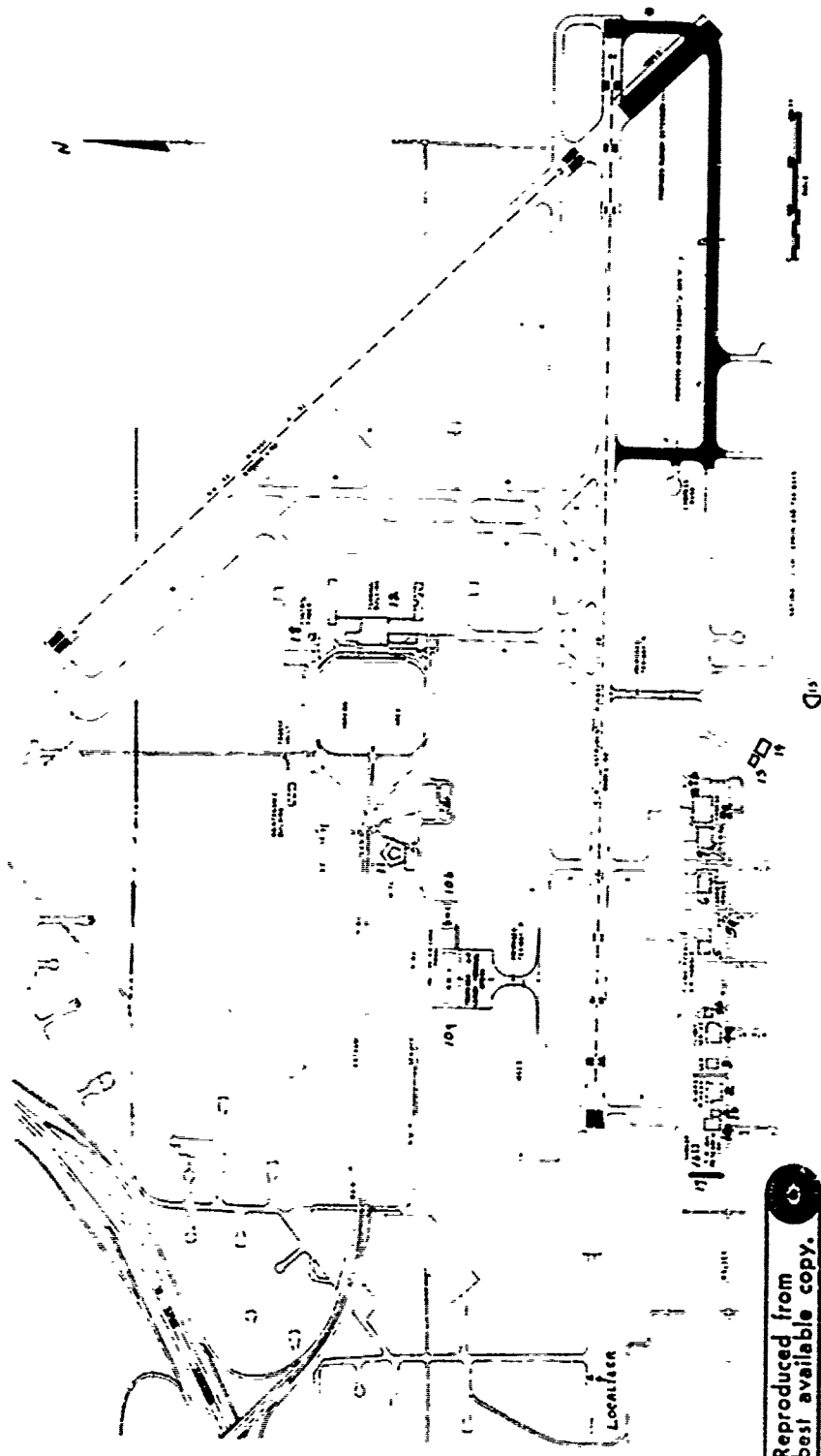
49

Figure 5-1. Syracuse-Hancock International Airport Layout Showing Instrumented Runway 28
and Surrounding Structures

50

Thus, the aircraft will receive indications of an off-centerline approach due to the combination of these reflected signals with the direct on-course signal. In order to approximate the amount of derogation caused by the signals reflected from the buildings shown in Figure 5-1, the buildings were modeled as perfectly reflecting rectangular walls.

The localizer is an eight-loop antenna located 2000 feet beyond the end of the runway at an effective height of 12 feet above ground. The tailored course width is 3.64°, and the glide path is 2.5°. With this data, the course deviation indication (CDI) in microamperes was calculated and compared with a flight recording taken in January, 1972. This is shown in Figure 5-2. The agreement is good, differences being due to any of a number of causes:

o   The approximation of perfectly reflecting walls;

o   The assumption that the aircraft was precisely on a 2.5° glide path and was travelling at 120 knots on a runway centerline approach;

o   The assumption that all building doors were closed.

The CDI flight test recordings and theoretical predictions show that runway 28 meets Category I FAA requirements but not Category II. The eight-loop localizer antenna used at Syracuse Airport has a rather broad azimuthal beam which illuminates many of the buildings shown in Figure 5.1 causing the reflections responsible for the indicated course deviation. If an antenna whose radiation pattern fell off more rapidly with azimuthal angle were used, several of the buildings which are now illuminated by the eight-loop might fall outside the range of the narrower azimuthal beam antenna leading to a better course structure for the runway.

It is known that the V-ring antenna pattern energy falls off more rapidly with azimuthal angle than does the eight-loop antenna. The V-ring antenna was therefore substituted for the eight-loop in the theoretical model and the CDI recalculated. As expected,

51
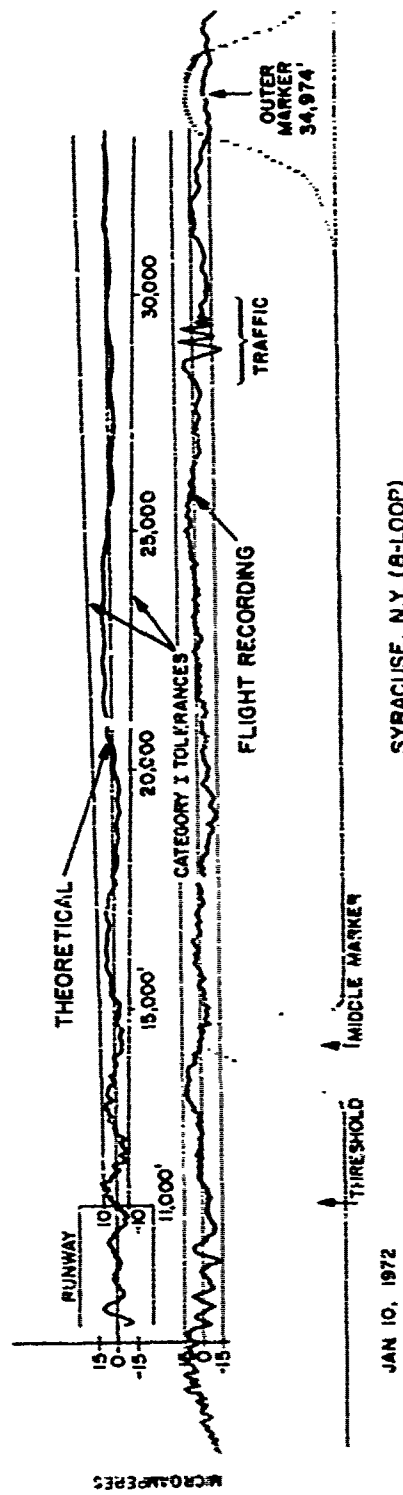
Figure 5-2. Comparison Between Flight Recording and Theoretical Prediction of Course Structure, Runway 28, Syracuse-Hancock Airport

52

the recalculated CDI is considerably reduced from that which was obtained with the eight-loop as shown in Figure 5-3. In fact, runway 28 at Syracuse-Hancock Airport may be upgraded from an instrumented Category I runway to one which meets FAA requirements for Category II by replacing the existing eight-loop localizer with a V-ring localizer.
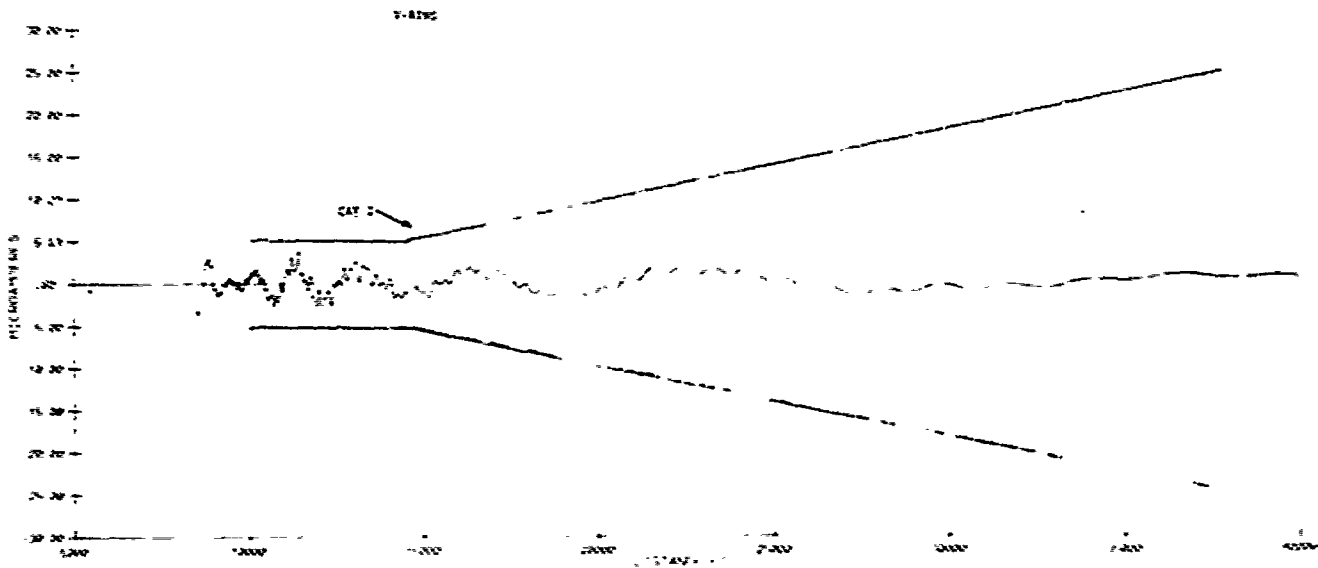
5.4 DALLAS/FORT WORTH STUDY

In the case of Dallas/Forth Worth Airport, input data for the model were obtained from a set of architectural drawings of the proposed four instrumented runways and Phase 1 building construction plans. This data was used to predict and compare ILS localizer performance using capture effect and non-capture effect localizer antenna systems for the four runways. The proposed airport layout plan is shown in Figure 5-4. Runways 17R and 35L running north and south are located to the west of the north-south (eighteen lane) highway shown flanked by terminal buildings (semicircles in Figure 5-4) located in the areas marked as 0W, 0E, 1W, 1E, etc. In the Phase 1 building plan, only terminal buildings in the areas marked 2E, 2W, 3E and 4E will be constructed. In addition to the construction of these large 3000-foot terminal buildings, a 124-foot high, 320- by 60-foot hotel will be constructed in location 3W, as well as a 175-foot high tower located symmetrically between the 17R/35L and 17L/35R runways and a Braniff and a Delta hanger located as shown in the figure. Runways 17L/35R also run north and south and are located to the east of the highway. The x-marks in the figure represent the proposed locations of the localizer antennas. The x-mark circumscribed by a circle represents a proposed Category II installation serving runway 17L.

The performance of a V-ring localizer and an Alford 1B localizer were compared for the four runways. The CDI was predicted along a centerline aircraft approach at a 2.5° glide path. A representative result comparing an Alford 1B and a V-ring localizer for runway 35L is shown in Figures 5-5 and 5-6 (the complete study may be found in Reference 5). These two figures show the dynamic CDI's (assuming a receiver time constant of 0.4 and an aircraft
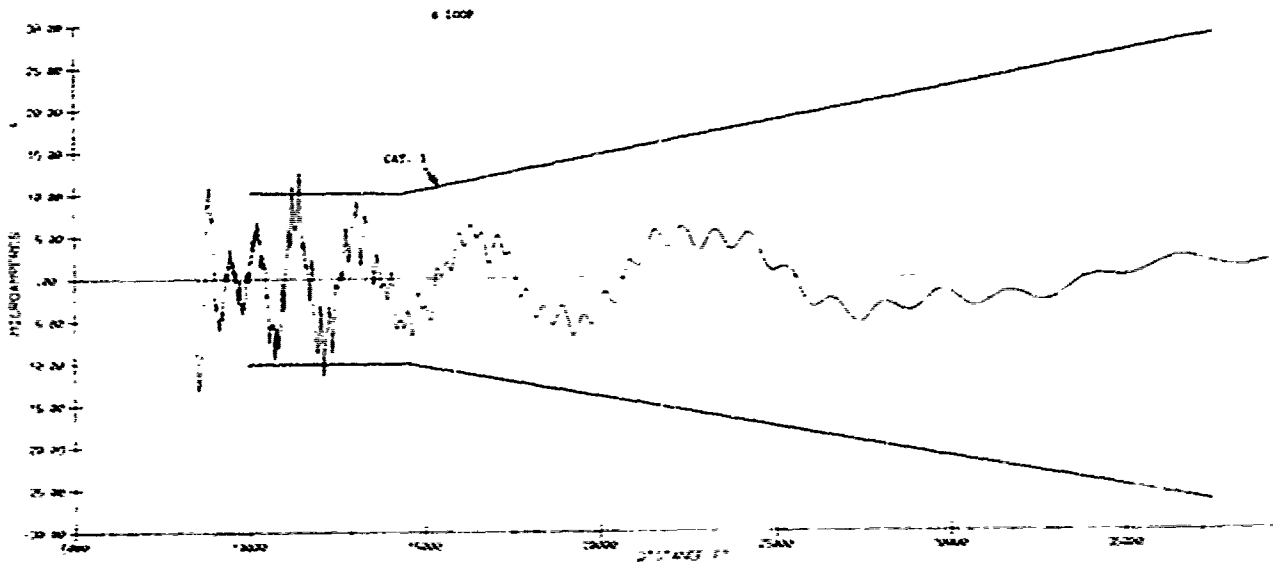
Theoretical CDI's at Syracuse-Hancock Airport
Using an 8-Loop Localizer

Theoretical CDI's at Syracuse-Hancock Airport
Using a V-Ring Localizer

Figure 5-3.   Comparison Between Course Structures Using
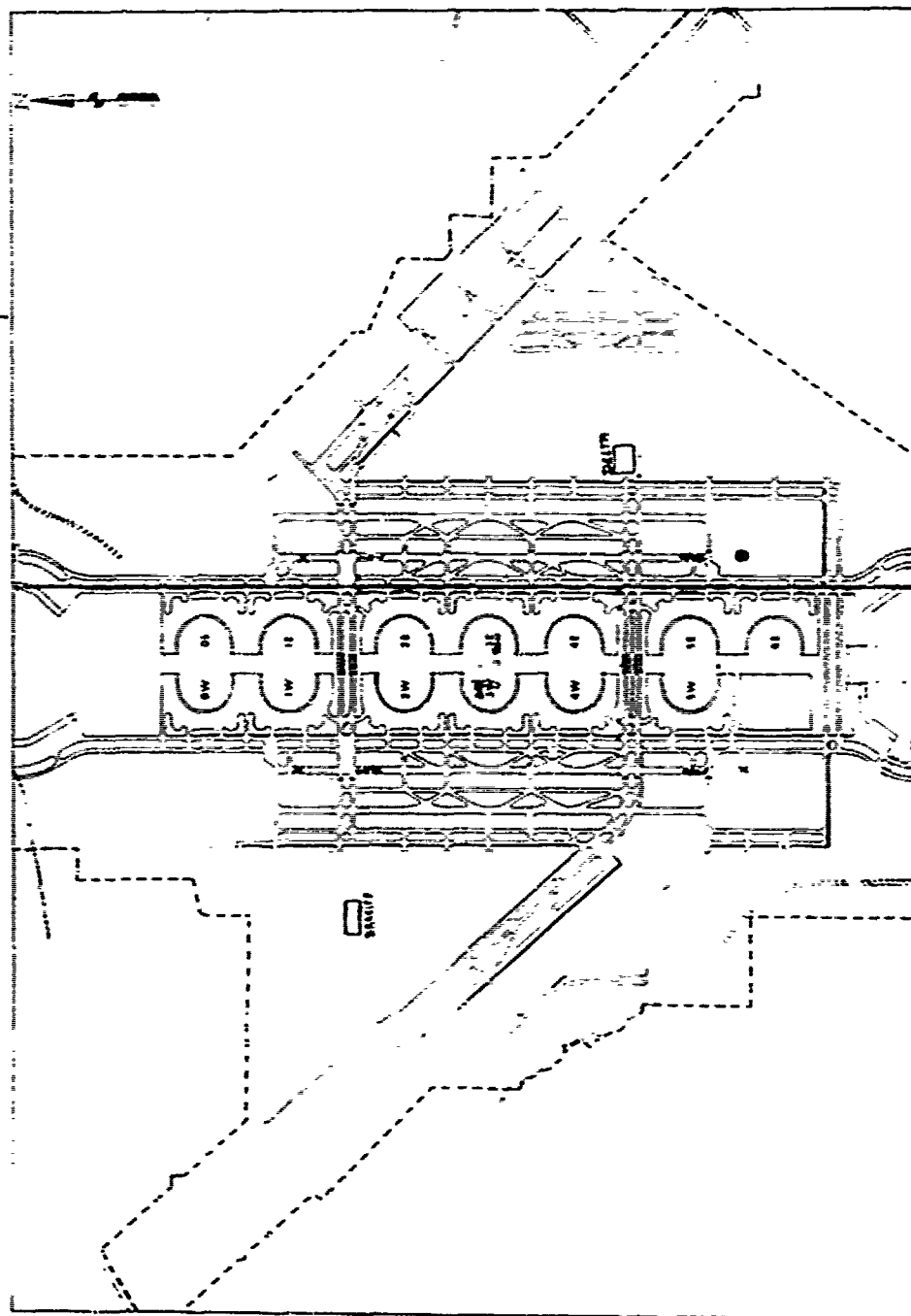a V-Ring and 8-Loop Localizer Antenna
Array

54

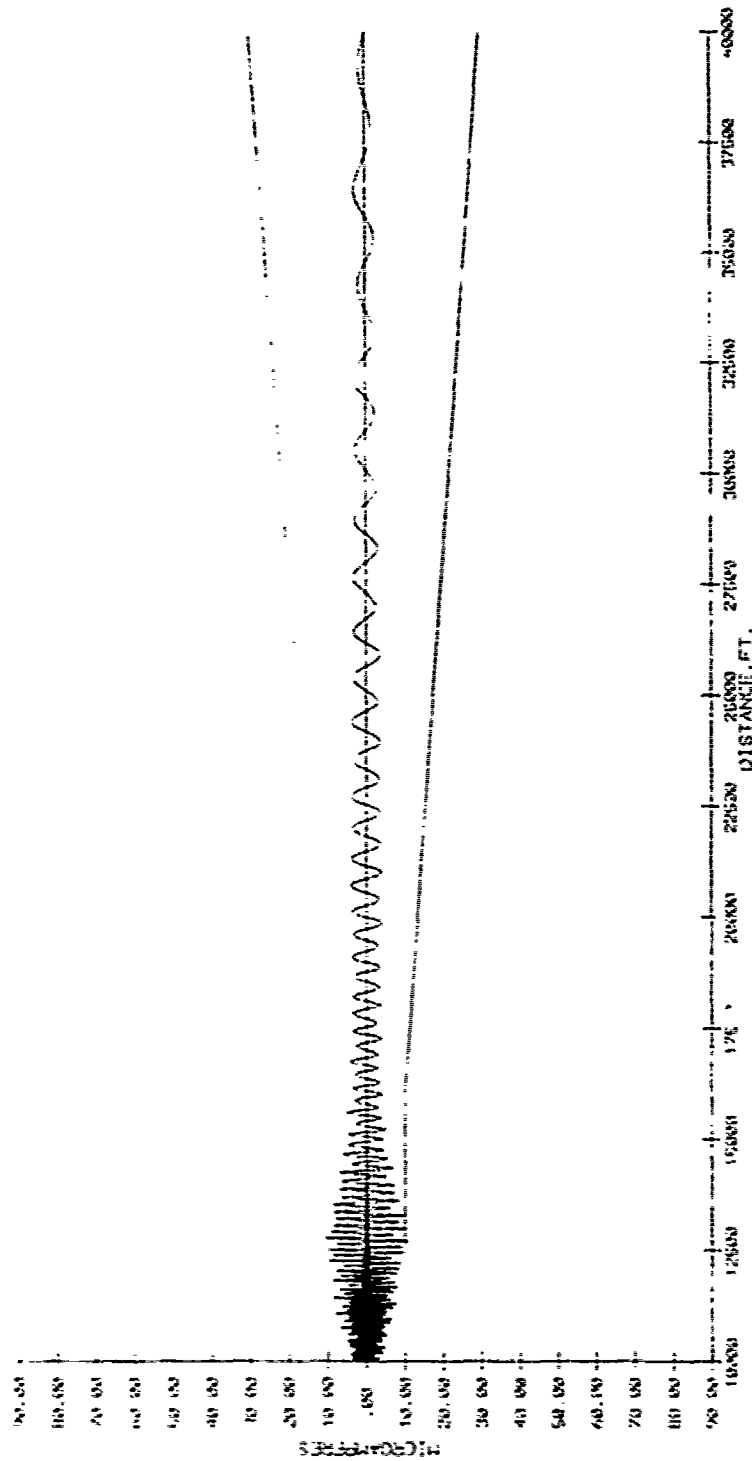Figure 5-4. Proposed Dallas/Fort Worth Airport Layout Plan

Figure 5-5. Predicted Course Structure in Presence of Terminals, Hotel and Tower Using a V-Ring Array for Runway 35L, Dallas/Fort Worth Airport
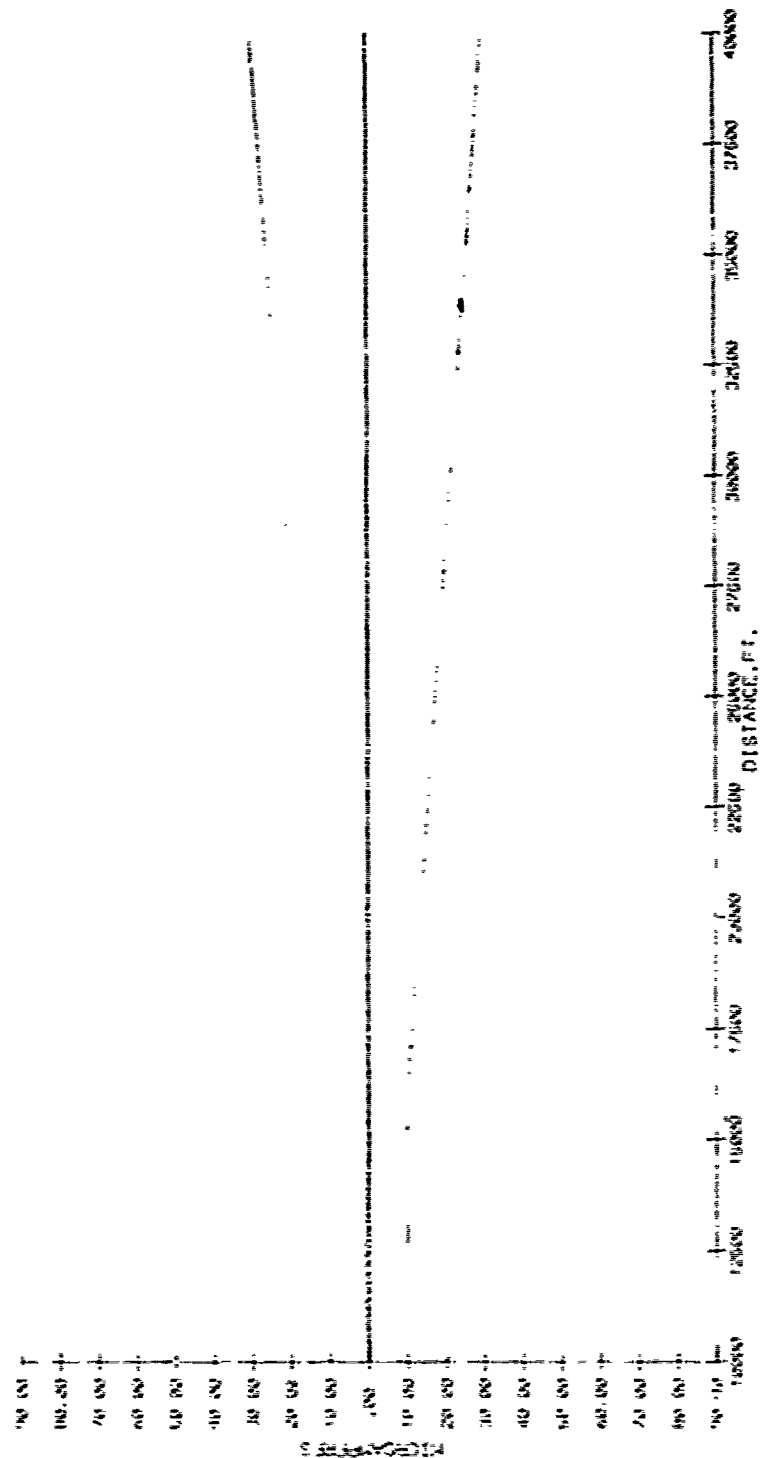
Figure 5-6. Predicted Course Structure in Presence of Terminals, Hotel and Tower Using an Alford 1B Localizer

speed of 120 knots) predicted by the model in the presence of terminals 2E, 2W, 3E and 4E, the hotel and the tower. Additional derogation due to the Braniff hangar when using the Alford 1B array is shown in Figure 5-7. The derogation due to the hangar is small. (The information on the Delta and Braniff hangars came too late to include in the original CDI prediction containing the terminal buildings, hotel and tower shown in Figures 5-5 and 5-6. At worst, the effect of the two hangars (only the Braniff hangar is shown here) will be to add to the total CDI shown in Figures 5-5 and 5-6, and using an Alford 1B, their effect should be negligible.)

The next two figures, 5-8 and 5-9, show the orbit clearance for runway 35L taken for an aircraft flying 600 feet above the ground and 25,000 feet from the localizer. Both the V-Ring and Alford array patterns meet the FAA specifications, yielding a CDI of 150 microamperes or more within the azimuthal sectors $\pm35°$.

We concluded from the application of the model to the Dallas/ Fort Worth Airport plan that the capture effect system (Alford 1B) should be used in preference to the V-Ring to insure that FAA Category I and Category II requirements be met on their respective runways under the Phase 1 construction plan.

5.5 SAN FRANCISCO AIRPORT STUDIES

The Transportation Systems Center model was also applied to runway 28 at the San Francisco Airport in order to help determine an acceptable localizer antenna for the course. Large derogation to the ILS localizer performance was expected here because of the presence of a large 747 American Airlines hangar located relatively close to the runway. Several different localizer systems were tried: A V-ring, the Alford 1B or 14/6 array, an Alford 2A or 22/8 array and the Texas Instrument Parabolic localizer antenna. In addition, the Alford and Texas Instruments antennas were operated at different capture effect ratios than is normally done in order to improve their performance.

The scattering situation is depicted in Figure 5-10. The hangar size is 560 feet by 456 feet, 135 feet high and is oriented

58
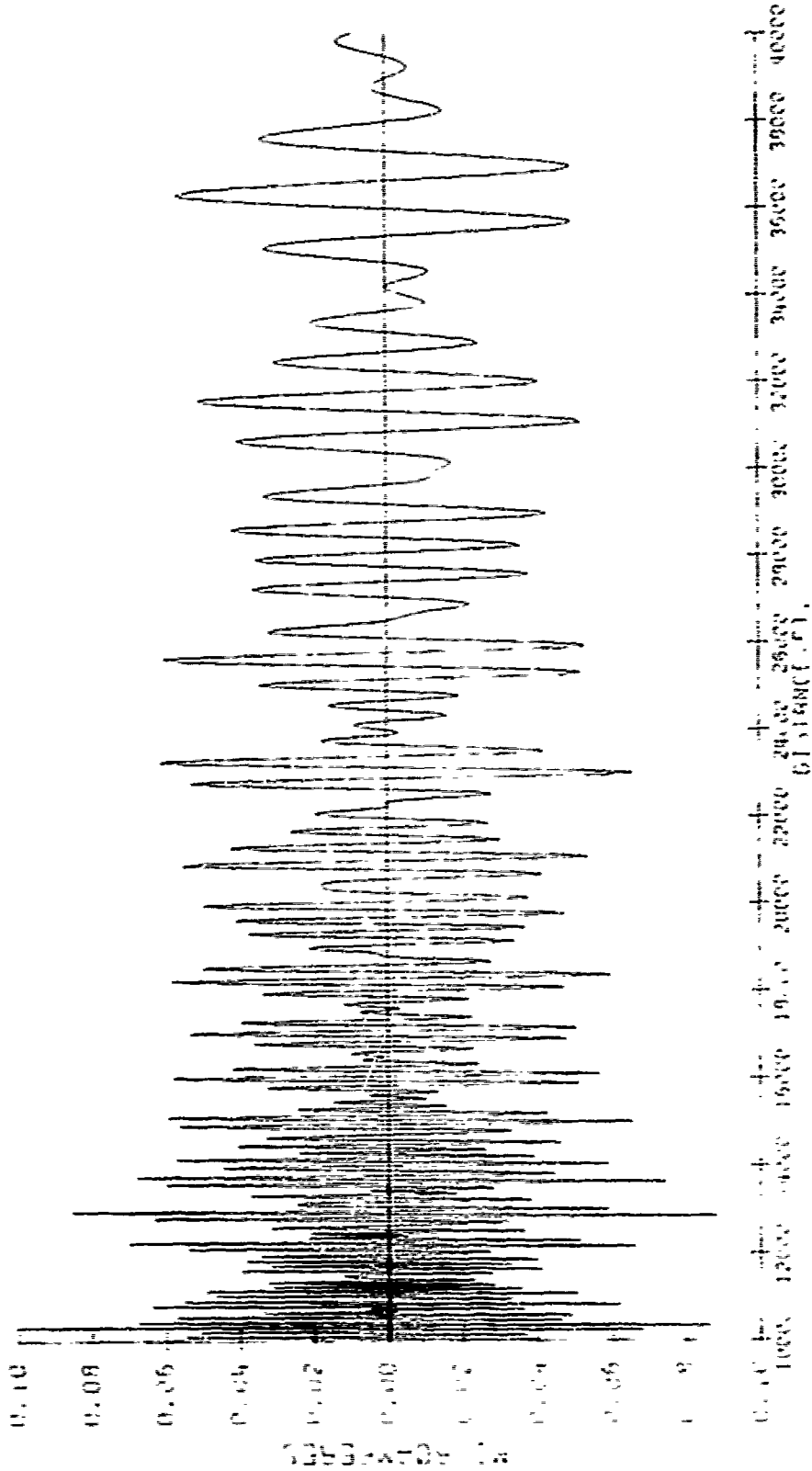
Figure 5-7. Predicted Course Structure in Presence of Braniff Hangar
Using an Alford 1B Localizer for Runway 35L, Dallas/
Fort Worth Airport
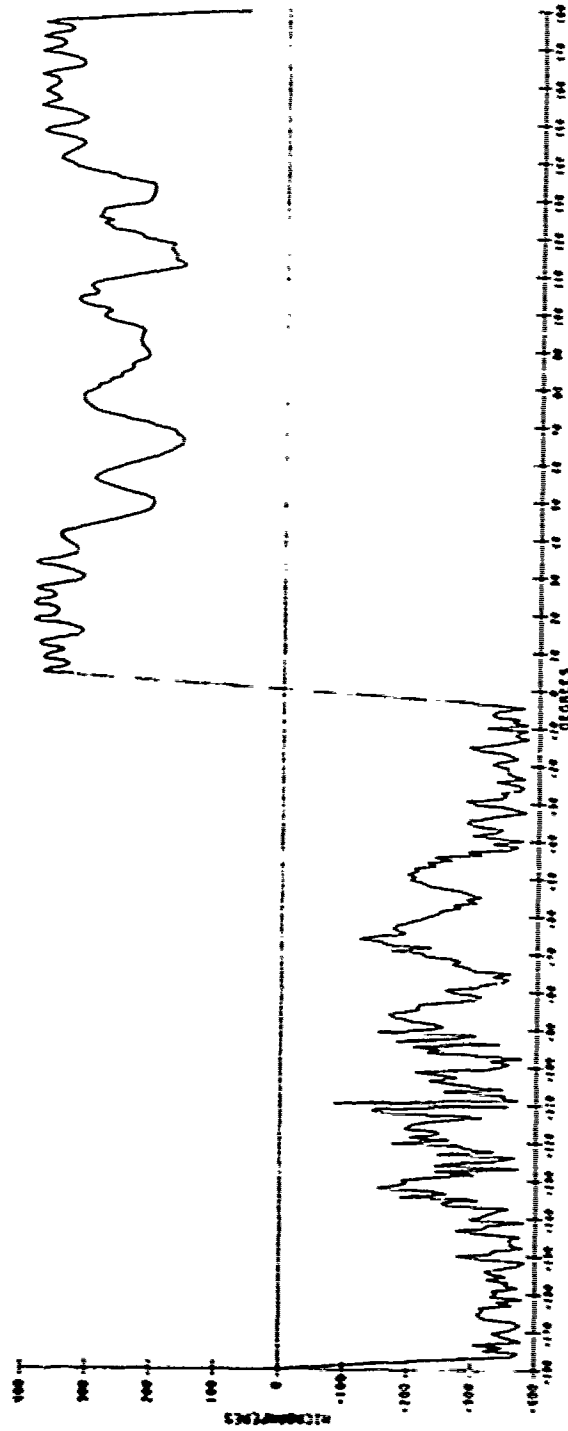
Figure 5-8. Predicted Orbit Clearance Structure in Presence of Terminals, Hotel and Tower Using a V-Ring Array for Runway 35L, Dallas/Fort Worth Airport

Figure 5-9. Predicted Orbit Clearance Structure in
Presence of Terminals, Hotel and Tower
Using an Alford 1B Localizer

AMERICAN AIRLINES HANGER
a= 560'
b=456'
HEIGHT IS 135'

LOCALIZER

RUNWAY
CENTERLINE

Figure 5-10. Schematic of Scattering Situation for
Runway 28, San Francisco Airport

parallel to and 1328 feet away from the runway centerline. The CDI was predicted for an aircraft flying a 2.5° glide slope centerline approach.

Figure 5-11 shows the predicted CDI when a V-ring is used. The course is very poor with this antenna owing to the large amount of sideband energy reflected from the hangar into the flight path of the aircraft. The reason for this is because of th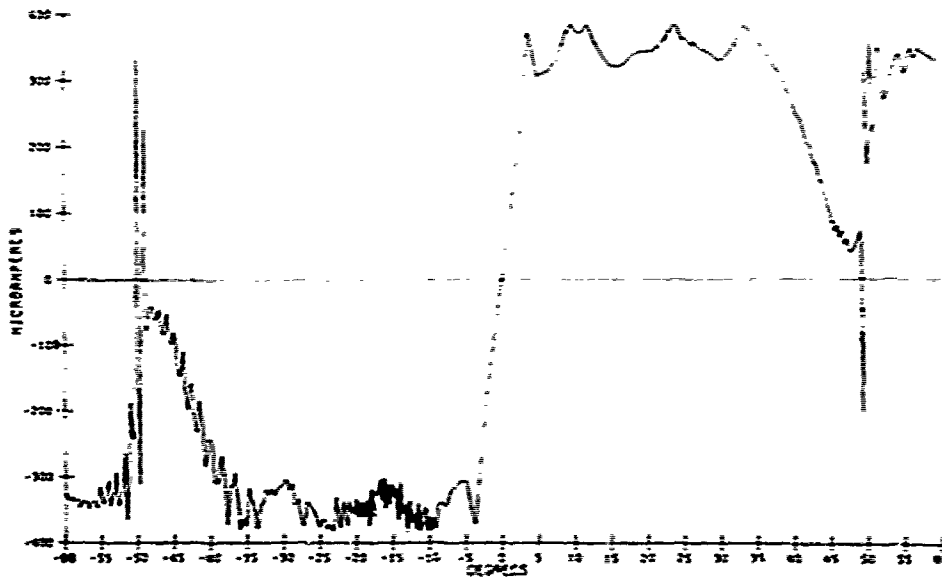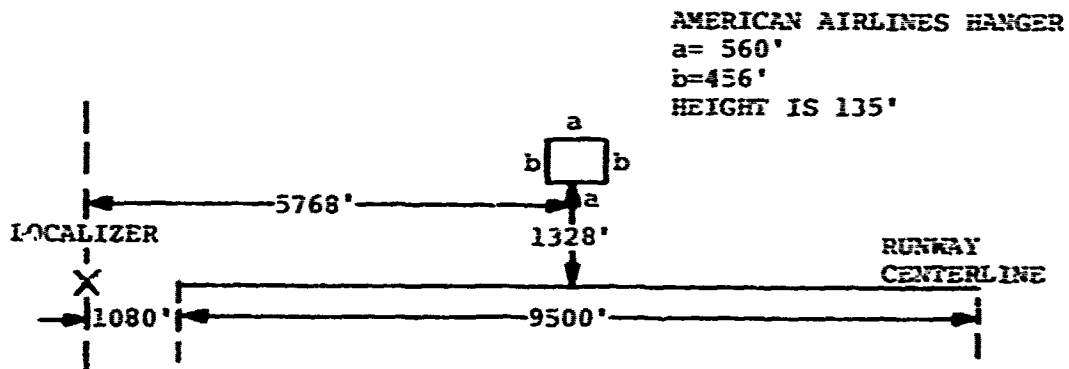e relatively large V-ring sideband radiation energy existing at 13°, the approximate angular position of the hangar off centerline.

Figures 5-12, 5-13 and 5-14 show the predicted CDI when using, in the normal mode of operation, an Alford 14/6, an Alford 22/8 and the Texas Instruments localizer antenna, respectively. The course structure has improved significantly in using these capture effect systems, but still remains poor. In order to further improve the course structure, we operated the Alford 22/8 array and the Texas Instruments Parabolic localizer at a higher course to clearance capture effect ratios than is normally done. We raised the capture effect rati from 10 db of normal operation to 16 db. The results are shown in Figures 5-15 and 5-16. The results show that significant improvement is attained in this higher capture effect ratio mode of operation. A localizer performance is predicted which allows FAA Category I requirements to be met, and, marginally, also Category II requirements. However, we caution that it has not been established that either the Texas Instruments Parabolic antenna or the Alford 22/8 array can function reliably at the higher 16 db capture effect ratio used in our theoretical model. Whether or not such operation is possible has to be determined in the light of the power output limitations of the course and clearance transmitters.

5.6 NEW ORLEANS AIRPORT STUDY

In the case of New Orleans Airport, we were asked to predict the performance of an Alford 1B localizer for runway 10 under the assumption that a roadway would be built in front of this localizer. The roadway would be a limited access road containing automobile traffic which could conceivably derogate localizer performance.

V-Ring: Dynamic Flyability Run

DYNAMIC RESPONSE
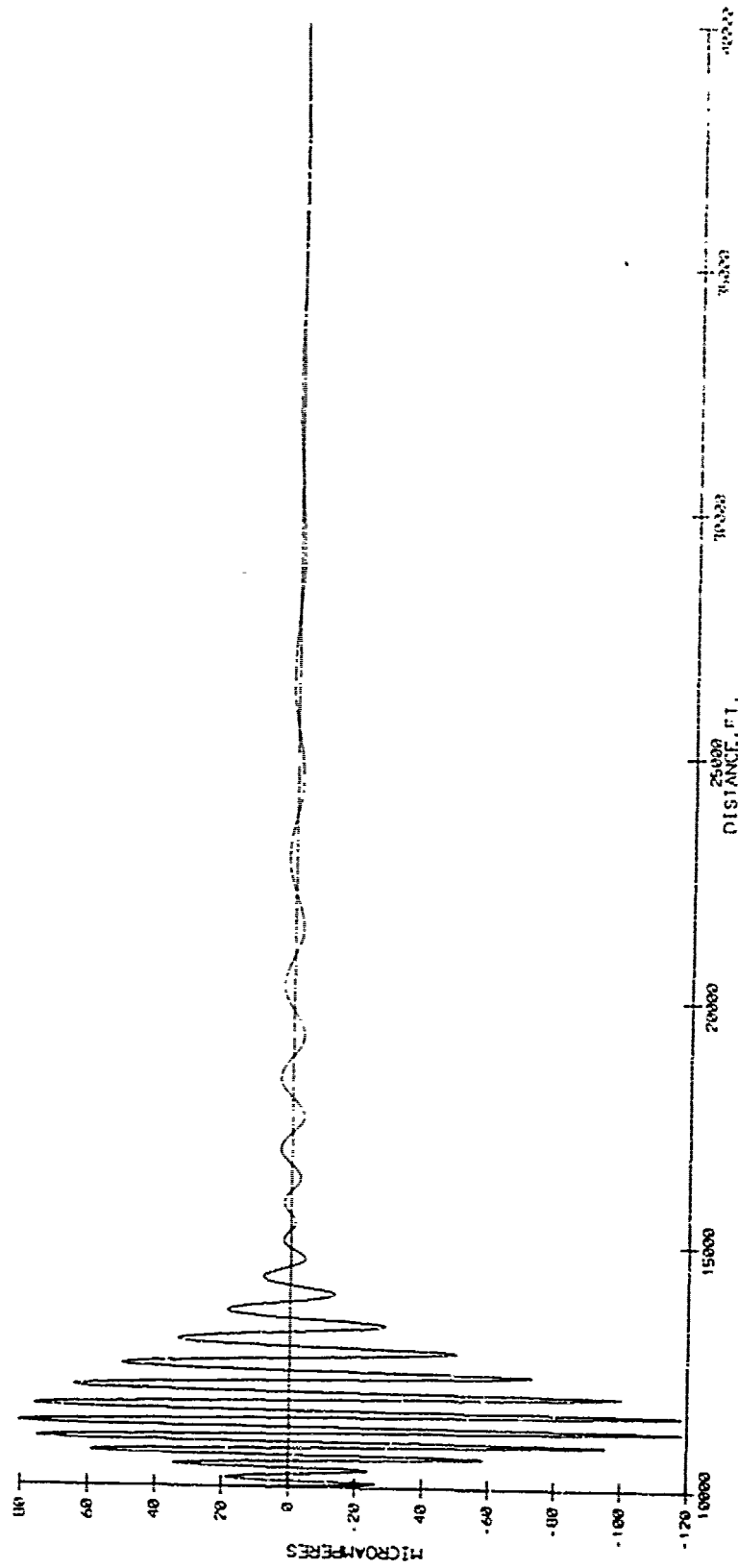
Figure 5-11. Predicted Course Structure Using a V-Ring Localizer,
Runway 28, San Francisco Airport

DYNAMIC RESPONSE
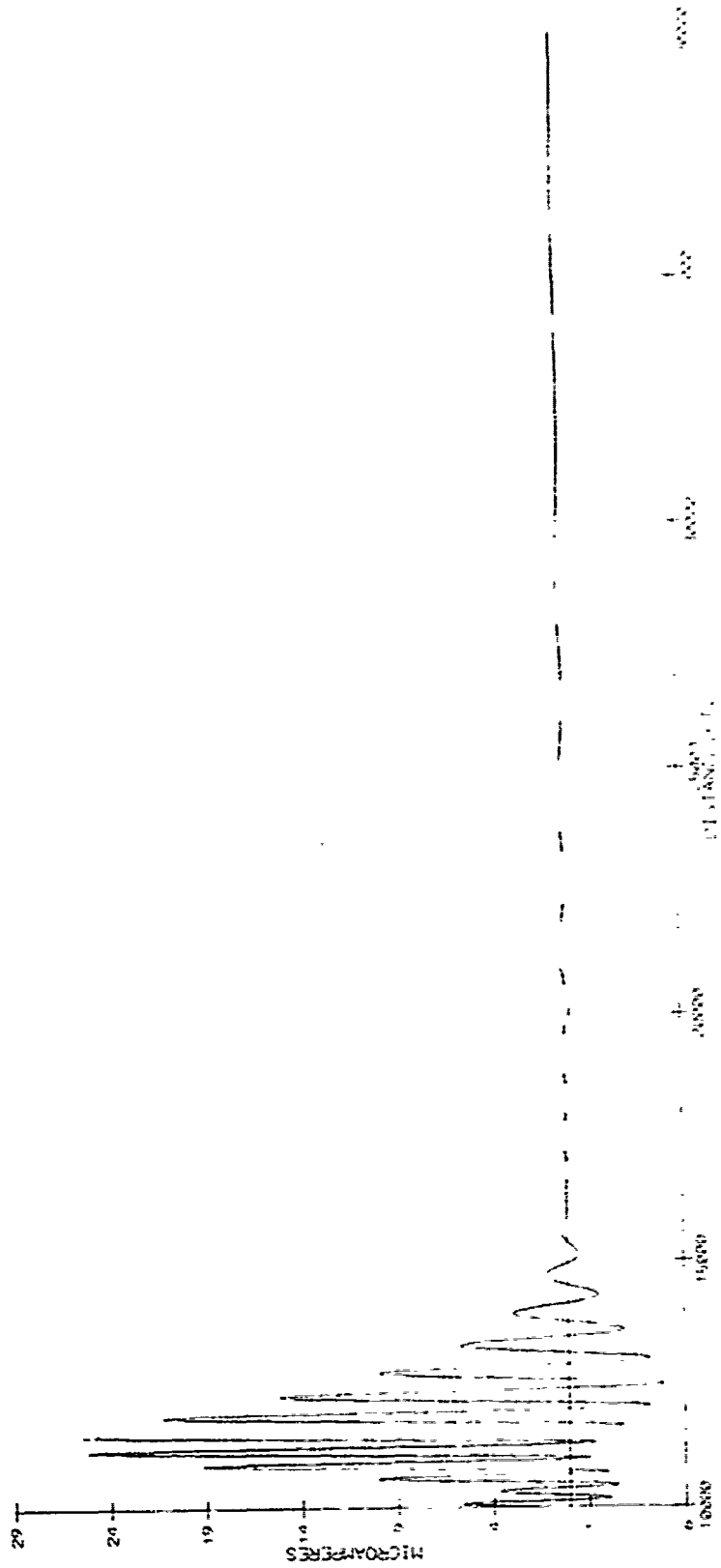
Figure 5-12. Predicted Course Structure Using an Alford 1B Localizer Operating with a 10 dB Capture Effect Ratio, Runway 28, San Francisco Airport

Alford 22/8: Dynamic Flyability Run: 10 db Course to Clearance Ratio

Figure 5-13. Predicted Course Structure Using an Alford 2A Localizer, Operating with a 10 dB Capture Effect Ratio, Runway 28, San Francisco Airport

Figure 5-14. Predicted Course Structure Using the
Texas Instrument's Parabolic Antenna
Operating with a 10 dB Capture Effect
Ratio, Runway 28, San Francisco Airport

66

Alford 22/8: Dynamic Flyability Run. 16 db Course to Clearance
Ratio.

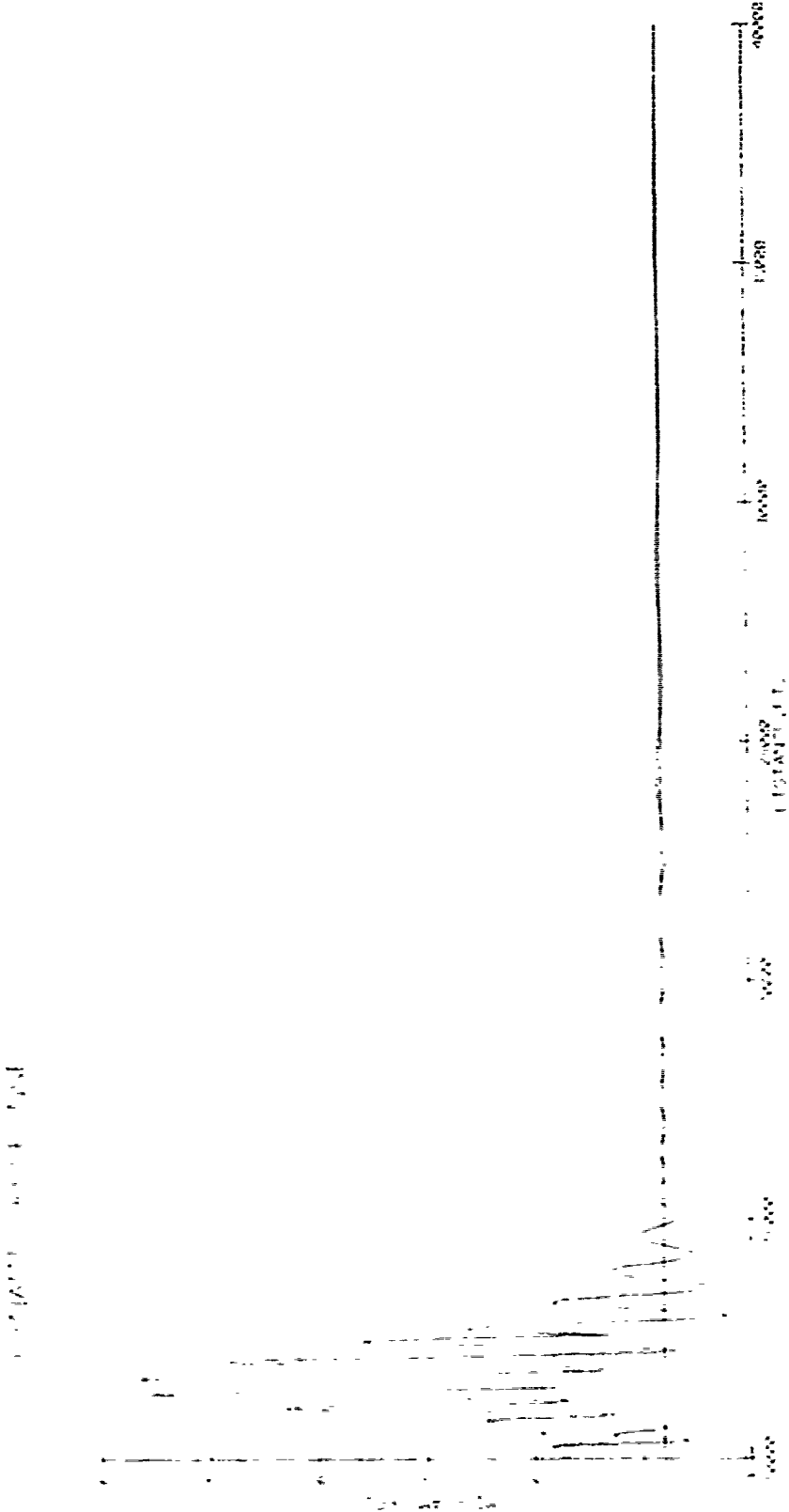Figure 5-15. Predicted Course Structure Using the Alford 2A Localizer,
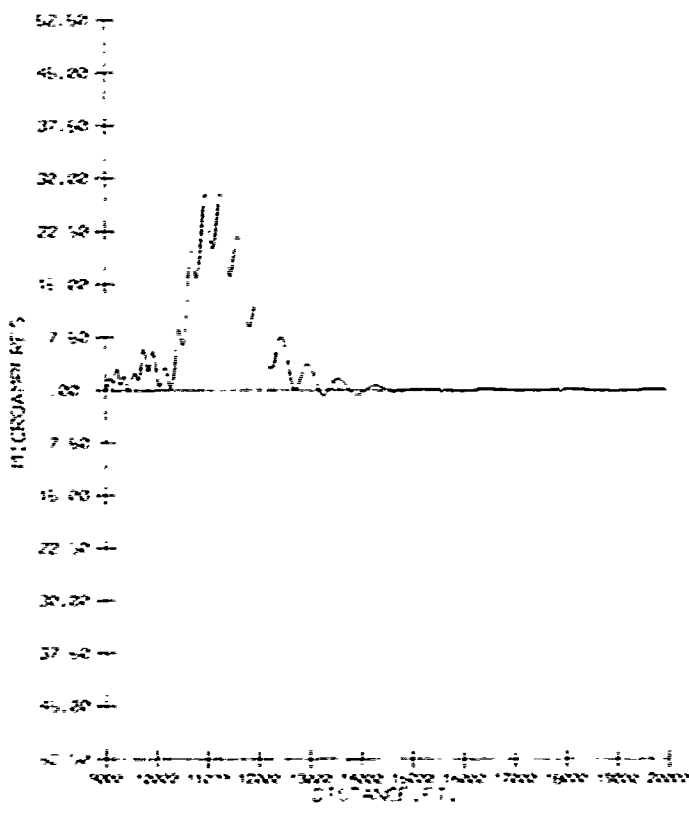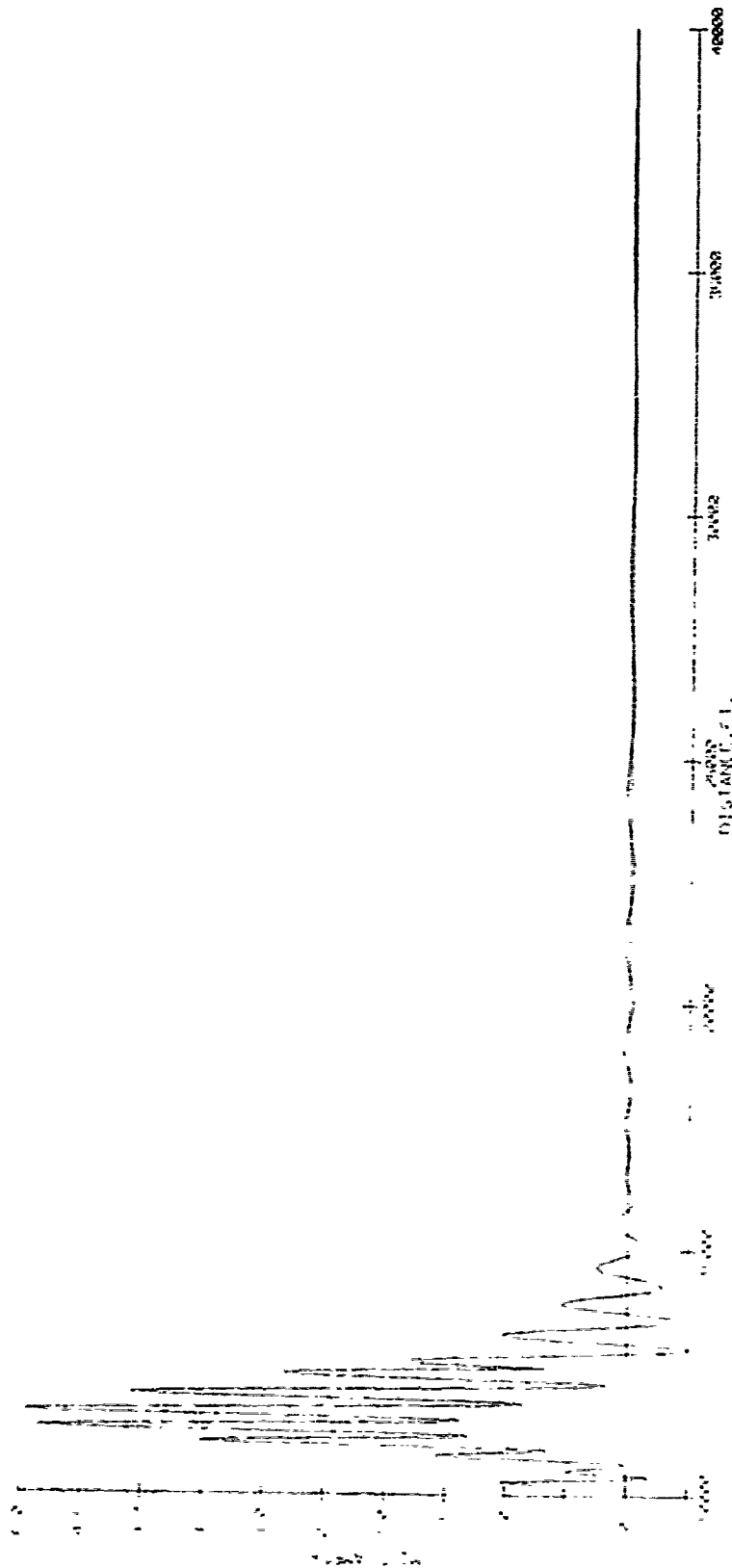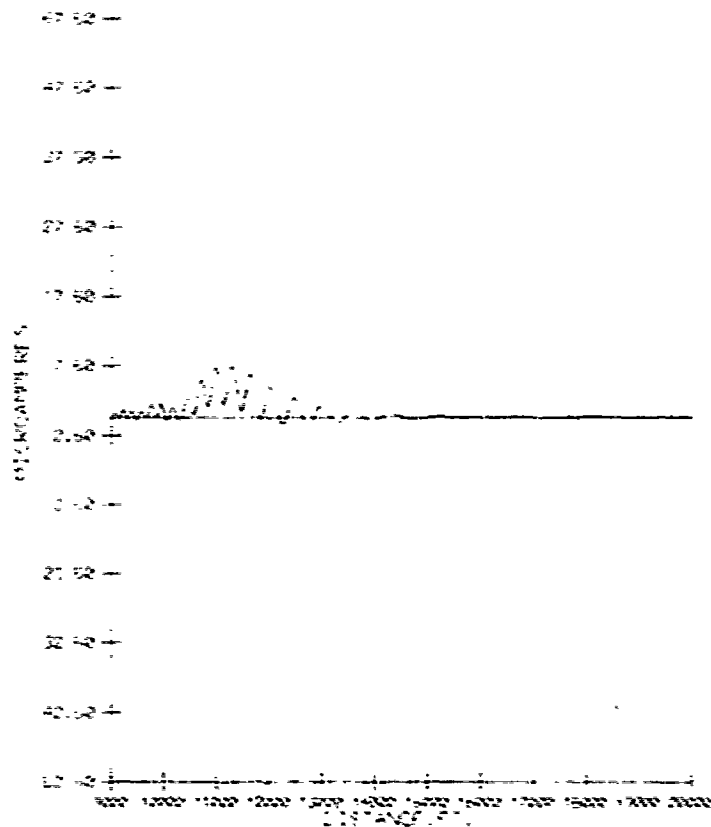Operating with a 16 dB Capture Effect Ratio

Figure 5-16. Predicted Course Structure Using the Texas Instruments Parabolic Antenna Operating with a 16 dB Capture Effect Ratio

68

Three alternate installations were proposed for the roadway, one in which the road was level with the ground, and two in which the road would be located at different depths below ground level. Only the level roadway was considered in this study.

Figure 5-17 shows a partial airport layout with the proposed limited access road running in a north-south direction perpendicular to the instrumented runway number 10. The localizer sketched in the figure is to be an Alford 1B array located 850 feet from the roadway centerline at its closest point. Various types of automobile traffic and one case of a single trailer truck were assumed and the resulting Alford 1B localizer operating with a 3.59° course width and a 10 dB capture effect ratio, was predicted for an aircraft flying a centerline, 2.5° glide slope approach.

The types of vehicular traffic for which the localizer performance was predicted consisted of a single perfectly-reflecting two-sided car, 20 feet by 8 feet and 6 feet high located on the road so as to give a worse case single-car result.[8]

A single perfectly-reflecting two-sided trailer truck 45 feet by 8 feet and 13 feet high was also modeled for comparison purposes with the car.[8]

A traffic jam along part of the roadway was also considered. The traffic jam situation was modeled as a long perfectly-reflecting wall 6 feet high.[8]

Finally, a worse case car spacing (called "Fresnel cars") was considered. Each car in this traffic spatial distribution is assumed to have two perfectly-reflecting sides 20 feet by 8 feet and 6 feet high, located as shown in Figure 5-18a.

The CDI's for these vehicular traffic situations were calculated along the flight path from a distance of 25,000 feet from the localizer to within 2000 feet of it. In all cases the derogation due to the presence of the representative traffic distributions modeled, is very small, indicating that the proposed (level) roadway carrying predominately automobile traffic will add only insignificant amounts of additional derogation to the course
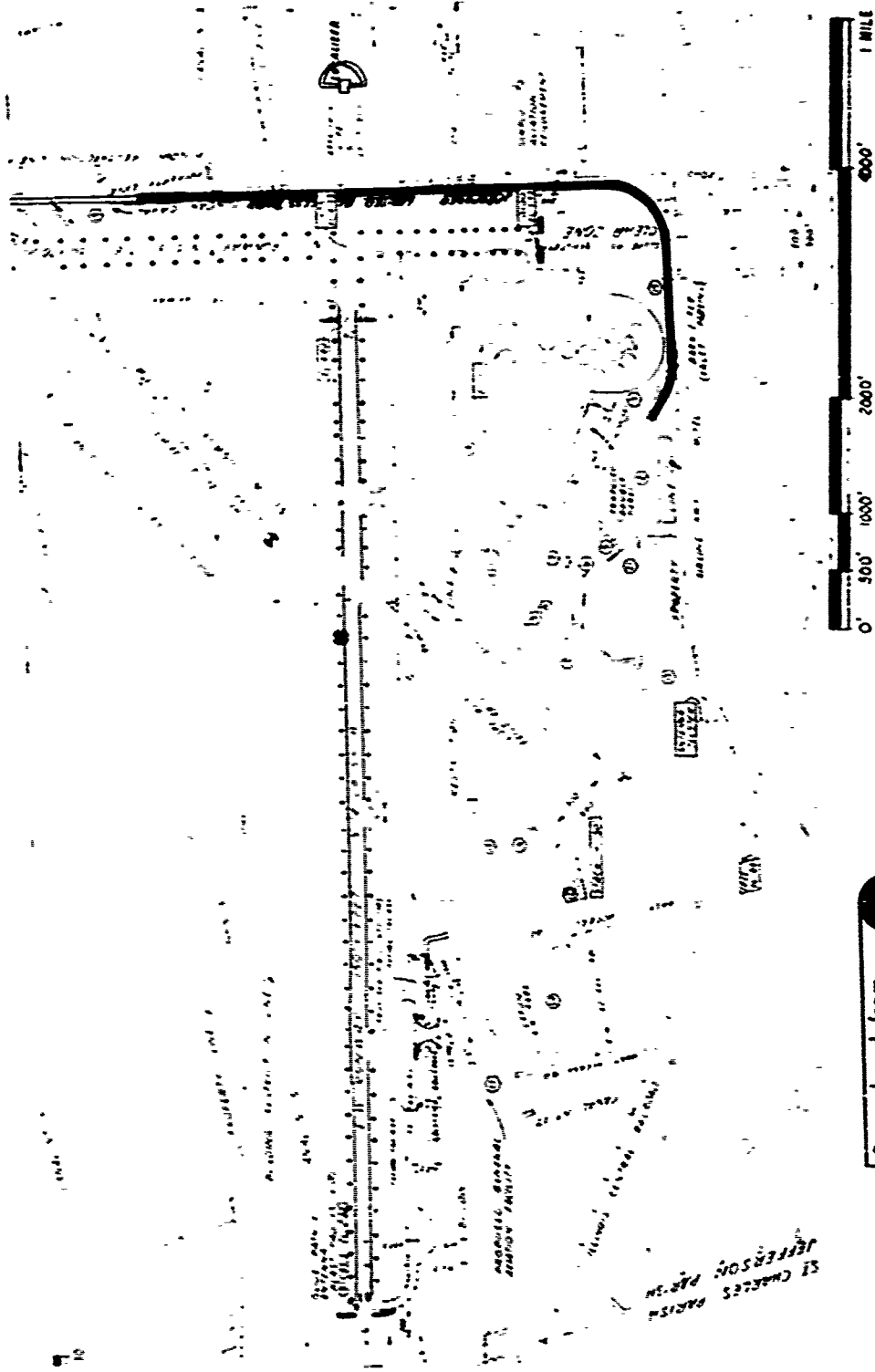
Figure 5-17. New Orleans Airport Layout Showing the Proposed Roadway and Instrumented
Runway 10

structure for runway 10 using an Alford 1B localizer. The predicted CDI in the presence of the "Fresnel Car Spacing" is shown in Figure 5-18b.

As noted in the report on the New Orleans study,[8] care must be taken in accepting these results without additional confirmation. This is because the TSC model was developed for the prediction of ILS performance when the main derogation is caused by scattering from large objects such as hangars where diffraction effects are of secondary importance. In the present problem, ILS derogation is due to scattering from small objects (small compared to several wavelengths) where diffraction effects are important. It is therefore difficult to predict how accurate the TSC model is in this case and independent validation is necessary.

5.7 SUMMARY OF APPLICATIONS

In summary, the examples of the applications of the model cited indicate the potential usefulness of the model.

- In a relatively inexpensive way we were able to suggest that a Category II operation of the instrumented runway at Syracuse-Hancock Airport is possible with the replacement of the present eight-loop localizer antenna array by a V-ring antenna array.

- For the Dallas/Fort Worth Airport we showed that the proposed Phase I construction plan was commensurate with acceptable ILS localizer performance when a capture effect system (Alford 1B) localizer antenna array was used.

- For runway 28 at the San Francisco Airport, we made a comparative study of different localizer antenna systems and,in a conservative estimate assuming that the derogator was perfectly reflecting, we showed that Category I FAA requirements would be met only by a capture effect system operating at a higher capture effect ratio than is normally done.

71
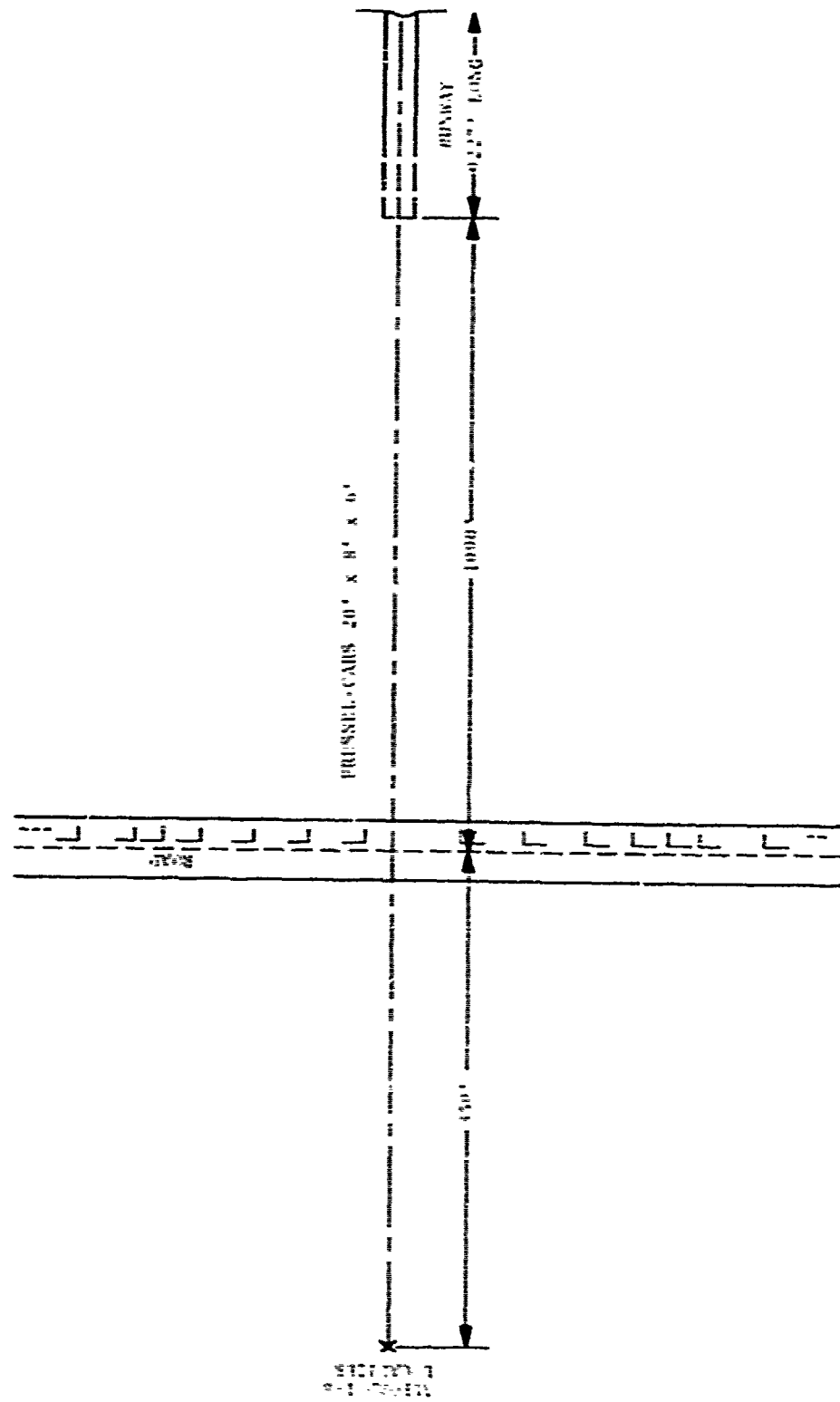
Figure 5.18a. Schematic of "Fresnel Car Spacing" Scattering Situation
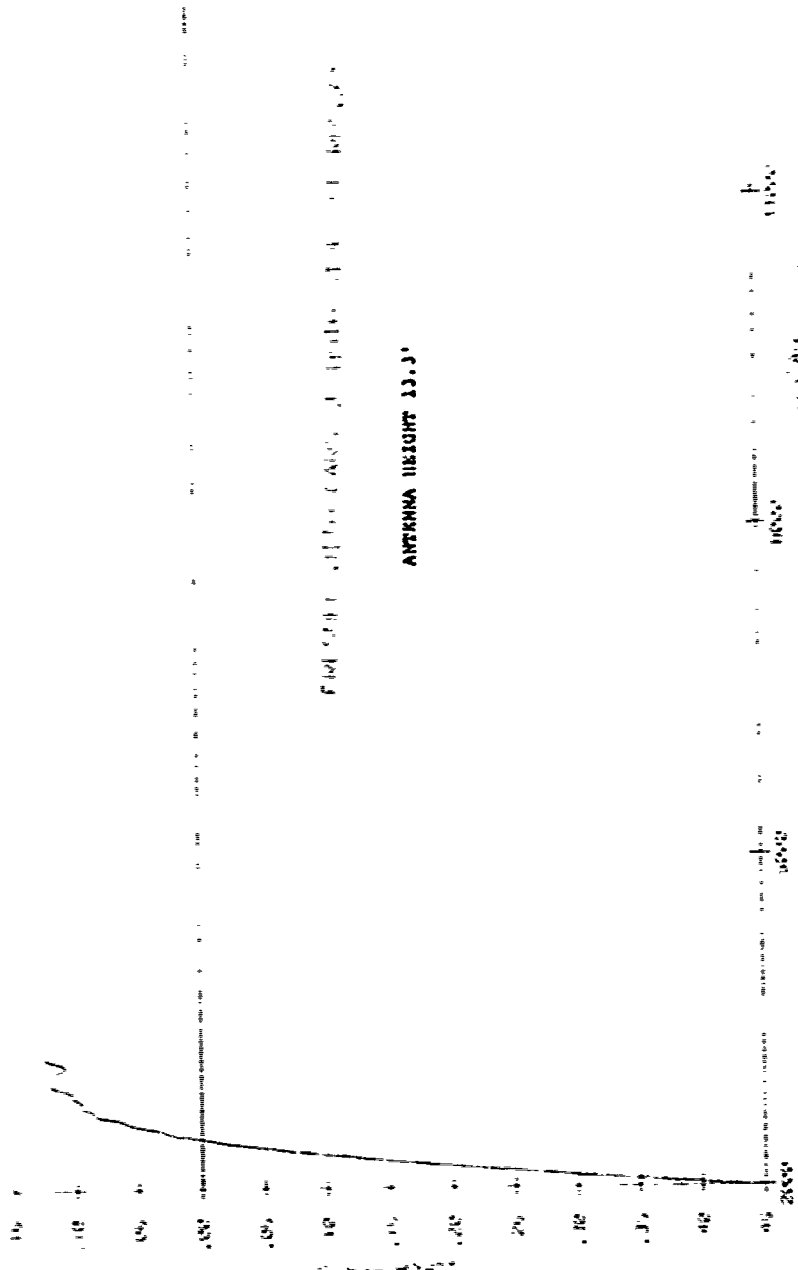
Figure 5-18b.   Predicted Course Structure Using an Alford 1B Localizer for the Situation
Depicted in Figure 5.18 a

- Finally, for New Orleans Airport we suggested that the proposed roadway could be built without causing significant derogation to the operation of a capture effect localizer system though additional confirmation was necessary in this case.

APPENDIX A

SCATTERING FROM A PERFECTLY CONDUCTING VERTICAL
CIRCULAR CYLINDRICAL SECTION ELEVATED ABOVE GROUND

In Section 2.3, localizer signal scattering by a right, circular cylinder situated on the ground was investigated. In this Appendix the scattering formulas appropriate to a cylinder which is elevated above ground level are derived. Figure A-1 shows the geometry for this scattering calculation. The reference point, O, is on the midpoint of the axis of the cylinder with section length Δz. z_1 is the height of the reference point above a flat infinitely conducting ground plane. P is a point on the surface of the cylinder and $\vec{r}$ is the vector from O to P. It is convenient to set up the coordinate system x', y', z' on the cylinder such that y' is an extension of $\vec{D}_{p1}$ (the ground projection of $\vec{R}_1$) and x' is perpendicular to $\vec{D}_{p1}$ (see Figure A-2a). As shown in Reference 1 for small elevation angles of the rays to the scattering surface, the incident electric field is given by:
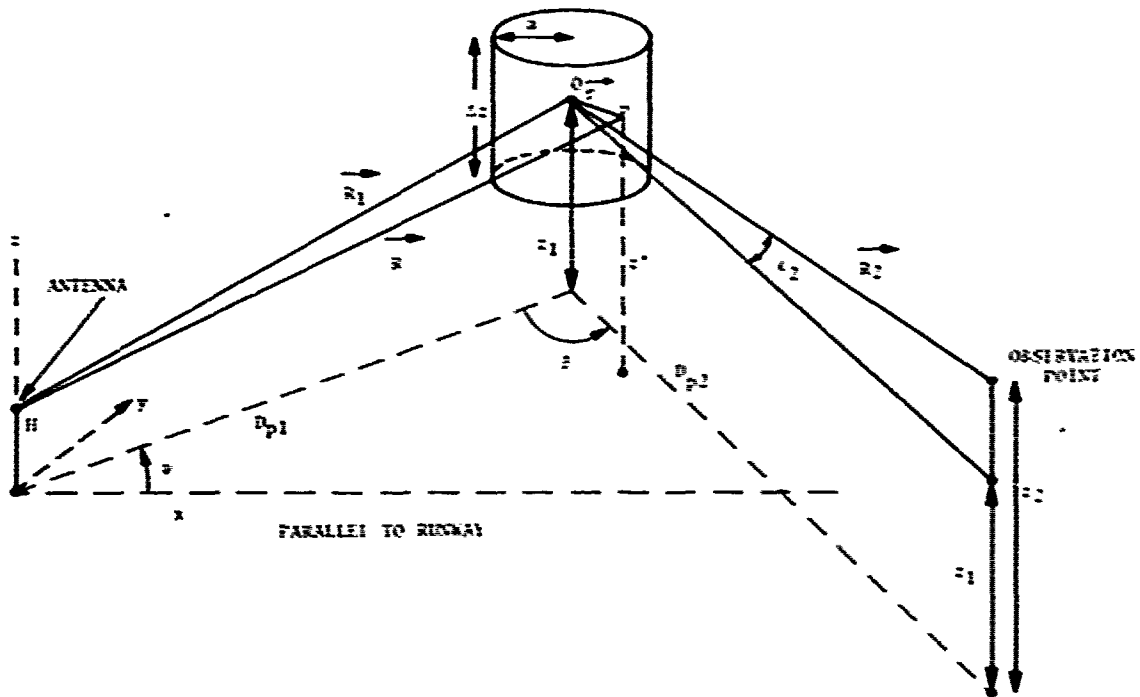
Figure A-1. Geometry for Scattering from
Vertical Circular Cylinder

75

$$\vec{E}_i \cong \hat{U} \, E_o \, f(\psi') \, \frac{e^{ikR}}{R} \left[1 - e^{2ikz'H/D}_{pl} \right] \qquad (A-1)$$

Where $\hat{U}$ is a unit vector giving the direction of electric field polarization and $f(\psi')$ is the horizontal antenna gain. The angle ψ' is the angle between the ground projection of $\vec{R}$ and the runway (ψ' is approximated by ψ the angle between the ground projection $\vec{R}_1$ and the runway). The variable z' is the distance of the field point P above the ground plane and may be expressed as:

$$z' = z_1 + z_c$$

where z_c is the distance of the field point P above a horizontal plane cutting the center of the cylinder as shown in Figure A-2b. The quantity kR may be expanded as:

$$kR = kR_1 + k\hat{R}_1 \cdot \vec{r} + \frac{k\left[r^2 - (\hat{R}_1 \cdot \vec{r})^2\right]}{2R_1} + \cdots \qquad (A-2)$$

where k is 2π divided by the wavelength λ. Then, under the restriction that:

$$\frac{kr^2}{2R_1} = \frac{\pi r^2}{\lambda R_1} \ll 1 \qquad (A-3)$$

we will approximate kR by the first two terms on the right hand side of Equation (A-2). In accordance with the geometry shown in Figures A-1 and A-2 the following equation is obtained:

$$\hat{R}_1 \cdot \vec{r} = - a \sin \phi' \cos \theta_1 + z_c \sin \theta_1 \qquad (A-4)$$

where ϕ' is the angle between x' and the projection of $\vec{r}$ onto the horizontal plane through the reference point, and where θ_1 is the angle between $\vec{R}_1$ and the projection of $\vec{R}_1$ on the ground plane.

The electric field incident at point P may then be written as:

76
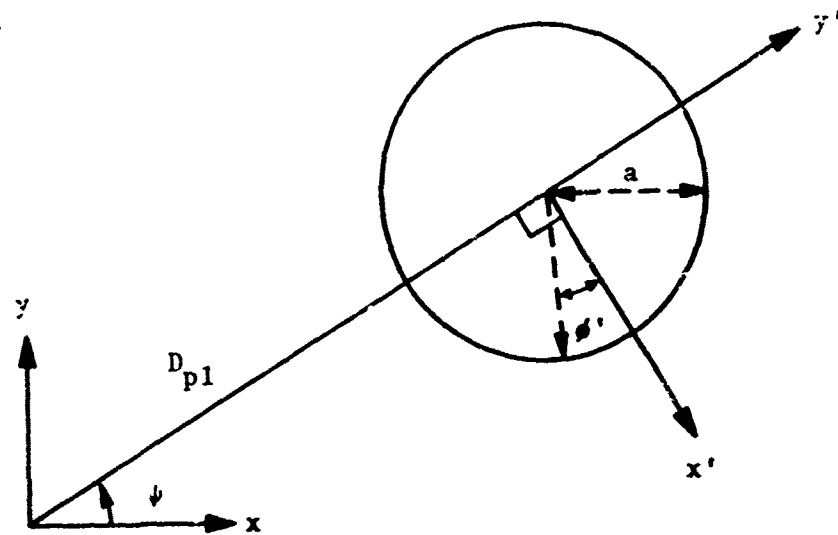
a. Top View of Circular Cylinder
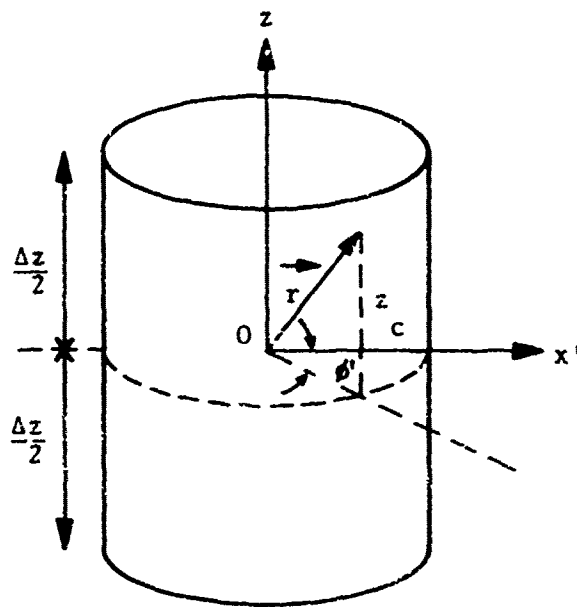
b. Another View of Circular Cylinder

Figure A-2. Circular Cylinder

77

$$\vec{E}_i \cong \hat{U} \, E_o \, f(\psi) \, \frac{e^{jkR_1}}{R_1} \, e^{-ika \sin \phi' \cos \theta_1}$$

$$\cdot \, e^{i \, kz_c \sin \theta_1} \left(1 - e^{2ik(z_1 + z_c)H/D_{p1}} \right) \tag{A-5}$$

The incident magnetic field is given by:

$$\vec{H}_i = |\vec{E}_i| \, \sqrt{\epsilon/\mu} \, (\hat{R} \times \hat{U}) \tag{A-6}$$

where $\sqrt{\mu/\epsilon}$ is the wave impedance of the medium. We assume $\hat{U}$ to be a horizontal vector and thus obtain:

$$\vec{H}_i = |\vec{E}_i| \, \sqrt{\epsilon/\mu} \, \left\{ - \frac{D_p}{R} \hat{e}_z + \left(\frac{(z'-H)}{R} \right) \left(\frac{x \, \hat{e}_x + y \, \hat{e}_y}{D_p} \right) \right\} \tag{A-7a}$$

$$\vec{H}_i \cong |\vec{E}_i| \, \sqrt{\epsilon/\mu} \, \left(- \cos \theta_1 \, \hat{e}_z + \sin \theta_1 \, \hat{e}_y \right) \tag{A-7b}$$

where:

$$\sin \theta_1 = (z_1 - H)/R_1 \tag{A-8}$$

$$\cos \theta_1 = D_{p1}/R_1 \tag{A-9}$$

$$R_1 = \left[D_{p1}^2 + (z_1 - H)^2 \right]^{1/2} \tag{A-10}$$

and D_p is the ground projection of R and $\hat{e}_x$, $\hat{e}_y$ and $\hat{e}_z$ are the unit vectors in the x, y, and z directions, respectively. In all subsequent calculations the small elevation angle approximation is made so that the second term on the right hand side of Equation (A-7b) may be neglected.

The surface current is given by:

$$\vec{J} = \vec{H}_{total} \times \hat{n} \tag{A-11}$$

where $\hat{n}$ is the unit normal vector pointing into the surface. To calculate the scattered f r field we require the Schelkunoff

78

radiation vector:

$$\vec{N} = \int dS \ \vec{J} \ e^{-ik(\hat{R}_2 \cdot \vec{r})} \tag{A-12}$$

where the integration is over the cylinder surface. When the diameter is much larger then the wavelength of the radiation we can use Kirchoff's approximation in which the tangential component of the total magnetic field is approximated by twice the tangential component of the incident magnetic field on the illuminated side and the very small field on the shadow side is approximated by a null field.

Then for the integration on the illuminated side we require the following:

$$\vec{J} \cong 2H_{zi} \ \hat{e}_z \times \hat{n} \tag{A-13}$$

where H_{zi} is the vertical component of the incident magnetic field as given by Equation (A-7). The x' and y' components of $\vec{J}$ are then (see Figures A-2a and A-2b)

$$J_x \cong -2H_{zi} \ \sin \phi' \tag{A-14a}$$

$$J_y \cong -2H_{zi} \ \cos \phi' \tag{A-14b}$$

where we have dropped the primes on the x and y subscripts in the expressions (A-14a) and (A-14b). We also have the relation:

$$\hat{R}_2 = \hat{\xi} \cos \varepsilon_2 \sin \beta - \hat{n} \cos \varepsilon_2 \cos \beta + \hat{e}_z \sin \varepsilon_2 \tag{A-15}$$

where $\hat{\xi}$, $\hat{n}$ and $\hat{e}_z$ are the unit vectors in the x', y' and z directions, respectively, and where:

$$\sin \varepsilon_2 = (z_2 - z_1)/R_2 \tag{A-16a}$$

$$\cos \varepsilon_2 = D_{p2}/R_2 \tag{A-16b}$$

$$R_2 = \left[D_{p2}^2 + (z_2 - z_1)^2 \right]^{1/2} \qquad \text{(A-16c)}$$

Since:

$$\vec{r} = a \cos \phi' \, \hat{\xi} - a \sin \phi' \, \hat{n} + z_c \, \hat{e}_z \qquad \text{(A-17)}$$

we have

$$\hat{R}_2 \cdot \vec{r} = a \cos \epsilon_2 \sin \beta \cos \phi' + a \cos \epsilon_2 \cos \beta \sin \phi'$$

$$+ z_c \sin \epsilon_2 \quad . \qquad \text{(A-18)}$$

The components of the Schelkunoff radiation vector in x' and y' directions are given by:

$$N_x = - 2 \int dS \, H_{zi} \sin \phi' \, e^{-ik(\hat{R}_2 \cdot \vec{r})} \qquad \text{(A-19a)}$$

$$N_y = - 2 \int dS \, H_{zi} \cos \phi' \, e^{-ik(\hat{R}_2 \cdot \vec{r})} \qquad \text{(A-19b)}$$

where

$$\int dS = a \int_{-\Delta z/2}^{\Delta z/2} dz_c \int_0^{\pi} d\phi' \quad .$$

From Equations (A-5), (A-7), (A-18), and (A-19) the following are calculated:

$$Y = N_x \cos \beta + N_y \sin \beta \qquad \text{(A-20a)}$$

$$= a\gamma_0 \, I \, I_\phi \qquad \text{(A-20b)}$$

where

$$\gamma_0 = 2 \sqrt{\frac{\epsilon}{\mu}} \cos \theta_1 \, E_0 \, f(\psi) \, e^{ikR_1} \big/ R_1 \quad , \qquad \text{(A-21)}$$

$$I = \Delta z \left\{ \text{sinc}\left[k(\sin\theta_1 - \sin\epsilon_2)\Delta z/2\right] \right.$$

$$\left. - e^{i2kHz_1/D_{p1}} \text{sinc}\left[k(\sin\theta_1 - \sin\epsilon_2 + 2H/D_{p1})\Delta z/2\right]\right\} \quad , \qquad \text{(A-22)}$$

where

$$\text{sinc } x = \sin x/x, \qquad \text{(A-23)}$$

and

$$I_\phi = \int_0^T d\phi' \, \sin(\phi'+\beta) \, e^{i(\alpha_0 \sin \phi' + \beta_0 \cos \phi')}, \quad \text{(A-24a)}$$

with

$$\alpha_0 = - ka(\cos \theta_1 + \cos \epsilon_2 \cos \beta) \qquad \text{(A-24b)}$$

$$\beta_0 = - ka \cos \epsilon_2 \sin \beta . \qquad \text{(A-24c)}$$

Using the identities to define C and G:

$$\alpha_0 \sin \phi' + \beta_0 \cos \phi' = C \cos (\phi'-G) \quad , \qquad \text{(A-25a)}$$

$$= C \sin \left(\frac{\pi}{2} - \phi' + G\right) \qquad \text{(A-25b)}$$

we may express I_ϕ as

$$I_\phi = \cos \beta \, I_6 + \sin \beta \, I_7 \quad . \qquad \text{(A-26)}$$

Dropping the prime on ϕ', we have

$$I_6 = \int_0^T d\phi \, \sin \phi \, \cos\left[C \sin\left(\frac{\pi}{2}+G-\phi\right)\right] + i \int_0^\pi d\phi \, \sin \phi \, \sin\left[C \cos(\phi-G)\right]$$

$$\text{(A-27)}$$

Using the expansion (Reference 9)

$$\cos{(C \sin \theta)} = J_o(C) + 2 \sum_{K=1}^{\infty} J_{2K}(C) \cos{(2K\theta)}, \qquad (A\text{-}28)$$

where J_n is the Bessel function of 1st kind of order n, we obtain for the real part of I_6:

$$R_e(I_6) = J_o(C) \int_0^{\pi} d\phi \sin \phi + 2 \int_0^{\pi} d\phi \sin \phi \cos(2K\phi)J_{2K}(C).$$

$$\cos\left[2K\left(\frac{\pi}{2} + G\right)\right]$$

$$+ 2 \int_0^{\pi} d\phi \sin \phi \sin(2K\phi)J_{2K}(C) \sin\left[2K\left(\frac{\pi}{2} + G\right)\right] \quad ,$$

from which is obtained:

$$R_e(I_6) = 2 J_o(C) + \sum_{K=1}^{\infty} 2 \left[\frac{1 - (-1)^{1+2K}}{1 - (2K)^2}\right] J_{2K}(C) \cos\left[2K\left(\frac{\pi}{2} + G\right)\right] \quad (A\text{-}29)$$

Likewise using the expansion:

$$\sin(C \cos \theta) = 2 \sum_{K=0}^{\infty} (-)^K J_{2K+1}(C) \cos\left[(2K + 1)\theta\right] \qquad (A\text{-}30)$$

we obtain for the imaginary part of I_6:

$$IM(I_6) = J_1(C) \pi \sin G \quad . \qquad (A\text{-}31)$$

For I_7 in Equation (A-26) we obtain

$$I_7 = \int_0^{\pi} d\phi \cos \phi \cos\left[C \sin\left(\frac{\pi}{2}+G-\phi\right)\right] + i \int_0^{\pi} d\phi \cos \phi \sin\left[C \cos(\phi - G)\right] .$$

$$(A\text{-}32)$$

82

Again using Equations (A-28) and (A-30) we obtain:

$$R_e(I_7) = J_0(C) \int_0^\pi d\phi \cos \phi + 2J_{2K}(C) \int_0^\pi d\phi \cos \phi \cos(2K\phi).$$

$$\cos\left[2K\left(\frac{\pi}{2} + G\right)\right]$$

$$+ 2 J_{2K}(C) \int_0^\pi d\phi \cos \phi \sin(2K\phi) \sin\left[2K\left(\frac{\pi}{2} + G\right)\right] \quad .$$

The first two terms are zero so that:

$$R_e(I_7) = 2 \sum_{K=1}^\infty J_{2K}(C)\left\{ \frac{2K\left[1 - (-1)^{2K+1}\right]}{(2K)^2 - 1} \right\} \sin\left[2K\left(\frac{\pi}{2} + G\right)\right] \qquad \text{(A-33)}$$

and similar calculations yield:

$$\text{Im}I_7 = J_1(C) \ \pi \cos G \quad . \qquad \text{(A-34)}$$

According to Equation (A-25a) where the constants C and G were introduced, we have:

$$C = \left(\alpha_0^2 + \beta_0^2\right)^{1/2} \qquad \text{(A-35a)}$$

$$= ka\left[\cos^2 \theta_1 + 2 \cos \theta_1 \cos \varepsilon_2 \cos \beta + \cos^2 \varepsilon_2\right]^{1/2} \ , \\ \text{(A-35b)}$$

$$\sin G = \alpha_0/C \qquad \text{(A-36a)}$$

$$\cos G = \beta_0/C \qquad \text{(A-36b)}$$

where β_0 and α_0 are given by Equations (A-24b) and (A-24c), and

$$G = \text{Im}\left[\ell n\left(\cos G + i \sin G\right)\right] \qquad \text{(A-37)}$$

so that I_ϕ (Equation (A-26)) is now known and the Schelkunoff radiation may be computed.

The induced voltage on a horizontal loop receiving antenna (vertical magnetic dipole) is given by

$$V = c_0 \left(\hat{e}_z \cdot \vec{H}_s \right) \sqrt{\mu/\epsilon} \qquad (A-38)$$

where c_0 is a constant, characteristic of the antenna and its loading. The scattered magnetic far field is given by:

$$\vec{H}_s = \frac{-ik}{4\pi R_2} e^{ikR_2} \left(\vec{N} \times \hat{R}_2 \right) \qquad (A-39)$$

and the scattered electric far field is given by:

$$\vec{E}_s = - \frac{ik\sqrt{\mu/\epsilon}}{4\pi} \frac{e^{ikR_2}}{R_2} \hat{R}_2 \times \left(\hat{R}_2 \times \vec{N} \right) . \qquad (A-40)$$

From Equations (A-38) and (A-39) we obtain the induced voltage:

$$V = c_0 \frac{ik}{4\pi R_2} e^{ikR_2} \cos \epsilon_2 \sqrt{\mu/\epsilon} \left(N_x \cos \beta + N_y \sin \beta \right) \qquad (A-41)$$

The preceding equations, (A-38) - (A-41) are essentially as given by Redlich in Reference 10.

The contribution to the induced voltage from the image of the cylindrical section is given by:

$$V_{im} = c_0 \left(\hat{e}_z \cdot \vec{H}_{im} \right) \sqrt{\mu/\epsilon} \qquad (A-42)$$

where $\vec{H}_{im}$ is the scattered magnetic field due to the image electric currents at the receiver location. The contribution from the image of the cylinder is then given by

$$V_{im} = - c_0 \frac{ik}{4\pi R_2'} e^{ikR_2'} \cos \epsilon_2' \left(\sqrt{\frac{\mu}{\epsilon}} Y_0 I_i I_{i\phi} \right) \qquad (A-43)$$

84

where R_2' is the distance from the reference point on the cylinder to the image of the receiver point,

$$R_2' = \left[D_{p2}^2 + (z_2 + z_1)^2 \right]^{1/2} \tag{A-44}$$

and where

$$\sin \varepsilon_2' = (z_2 + z_1)/R_2' \tag{A-45}$$

And $I_i = I$ (see Equation A-22) when $\sin \varepsilon_2'$ replaces $- \sin \varepsilon_2$ there. Also $I_{i\phi} = I_\phi$ in Equations (A-24) when

$$\cos \varepsilon_2' = D_{p2}/R_2' \tag{A-46}$$

replaces $\cos \varepsilon_2$ there. Finally, γ_c is given in Equation (A-21).

The total induced voltage is given by the sum of the contributions from the cylinder and its image:

$$V_{total} = V + V_{im} . \tag{A-47}$$

The scattering from the complete elevated cylinderical object is then obtained by simply summing up the contributions from each of the cylindrical sections treated in this appendix.

APPENDIX B

(1) SCATTERING FROM A SLANTED PERFECTLY
CONDUCTING TRIANGULAR SLAB ELEVATED
ABOVE GROUND

(2) SCATTERING FROM A SLANTED PERFECTLY
CONDUCTING DISK ELEVATED ABOVE
GROUND

B.1 SCATTERING FROM A SLANTED TRIANGLE

In a previous report, Reference 1, Section 4.4, a general
formulation for the scattering from a perfectly-conducting rectan-
gular flat surface was developed. That formulation is modified to
obtain the scattering from an elevated, slanted right triangular
slab having one edge parallel to the ground plane. The slab is
placed above a flat perfectly-conducting ground plane. In Equation
(4.97) of Reference 1 the voltage induced in a horizontal loop
antenna at the observation point by the scattered field from a
flat slab is given by:

$$V = - c_o I_b \cos \varepsilon_2 \left[\cos \theta_1 \sin \varepsilon \cos \beta - \sin \theta_1 \cos \varepsilon \cos(\beta + \gamma) \right] \quad \text{(B-1)}$$

(Note that the minus sign on the right hand side of this equation
was inadvertently omitted in Equation (4.97) of Reference 1).
Equations (4.82), (4.83) and (4.86) of Reference 1 give:

$$I_b = \frac{ik E_o f(\psi)}{2\pi} \exp\left[ik(R_2 + R_1) \right] I_c / R_2 R_1 \quad \text{(B-2)}$$

and

$$I_c = \int dn d\xi \left\{ \exp\left[ik(\hat{R}_1 \cdot \vec{r}) \right] \left[1 - \exp(ik \, 2z' \, H/D_{pl} \right] \right. \quad \text{(B-3)}$$

$$\left. \cdot \exp(-ik\hat{R}_1 \cdot \vec{r}) \right\} \quad \text{(B-3a)}$$

or,

$$I_c = \int dn \, \exp\left[ik(A - \eta_o)\eta \right] \cdot \left\{ \int d\xi \, \exp\left[ik(B - \xi_o)\xi \right] \right.$$

$$\left. - \exp T \int d\xi \, \exp\left[ik\left(B - \xi_o + \frac{2H \sin \varepsilon}{D_{pl}} \right) \xi \right] \right\} \quad \text{(B-3b)}$$

36

(the parameters in Equation (B-3b) are given in Equations (B-5) through (B-13) below).

For the case of the slanted triangle we specify the boundaries of the surface integration in Equation (B-3). Figure B-1 shows the general geometric relations for the problem. Figure B-2a, b, c and d show four orientations for the slanted right triangle. The reference point, O, is taken to be on the midpoint of the side that is parallel to the ground plane. For all four cases the η integration goes from $-\frac{L}{2}$ to $+\frac{L}{2}$:

$$\int_{-L/2}^{L/2} d\eta \ .$$

CASE 1. Acute angles pointing to the left and upwards (as shown in Figure B-2a). In the right hand side of Equation (B-3) the parameter ξ is integrated from 0 to $h(\eta/L + 1/2)$. We obtain:

$$I_c = (i/k) \left\{ - (1/B') \ e^{ikB''h/2} \ L \ \text{sinc} \ (W \ L/2) \right.$$

$$+ (1/B'') \ e^T \ e^{ikB''h/2} \ L \ \text{sinc} \ (W'L/2)$$

$$\left. + L \ \text{sinc} \left[k(A-\eta_0)L/2 \right] \left[\frac{1}{B'} - \frac{1}{B''} \ e^T \right] \right\} , \qquad (B-4)$$

where:

$$B'' = B - \xi_0 + 2H \sin \epsilon / D_{p1} \qquad (B-5)$$

$$B' = B - \xi_0 \qquad (B-6)$$

$$B = \cos \theta_1 \cos \epsilon \cos \gamma + \sin \theta_1 \sin \epsilon \qquad (B-7)$$

$$\xi_0 = - \cos \epsilon_2 \cos \beta \cos \epsilon + \sin \epsilon_2 \sin \epsilon \qquad (B-8)$$

$$\eta_0 = \cos \epsilon_2 \sin \beta \qquad (B-9)$$

87
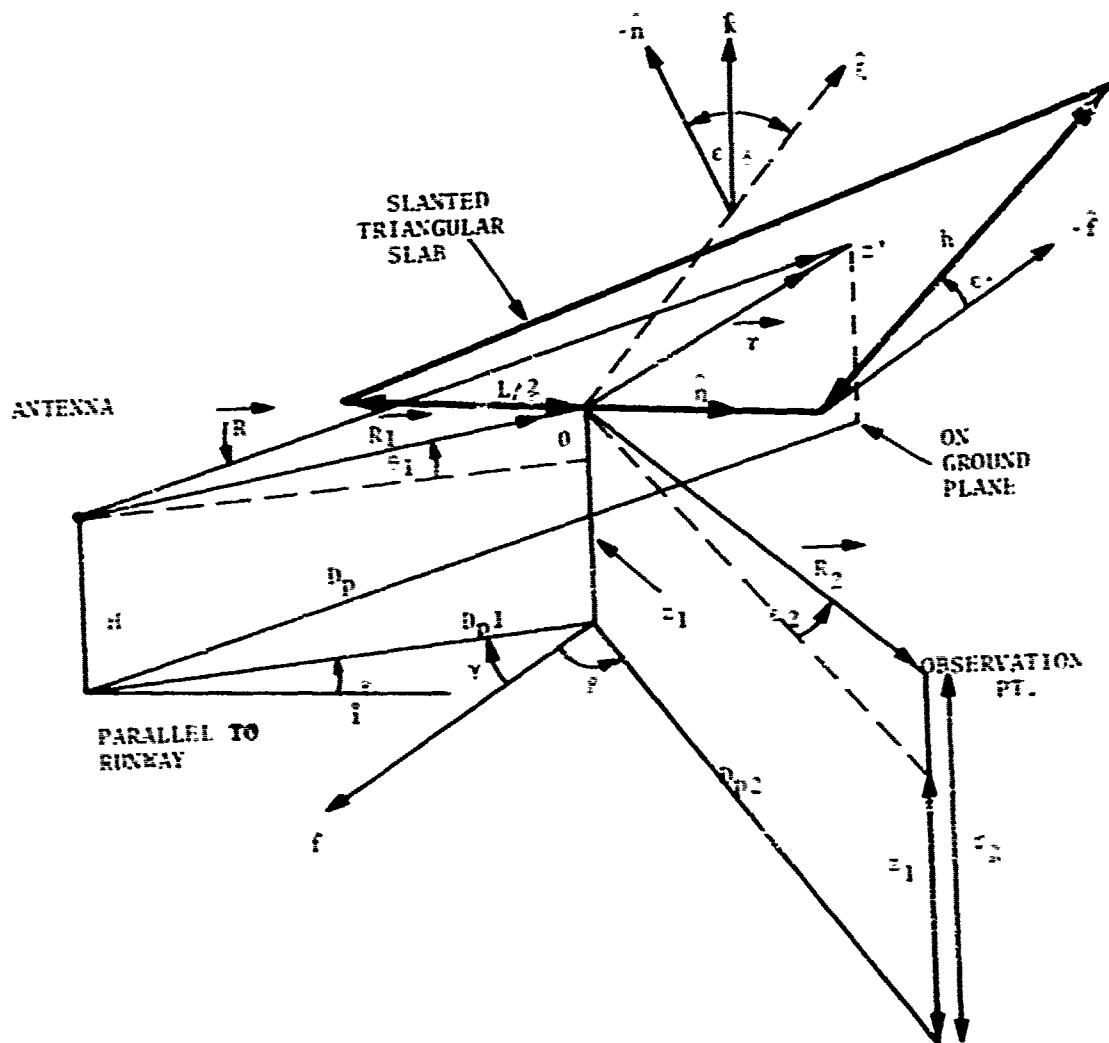
Figure B-1. Geometric Relations for Scattering from a Slanted Right Triangular Slab With One Edge Parallel to the Ground Plane
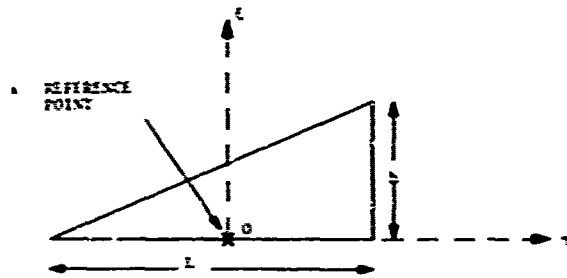
a. Slanted Right Triangle
   Pointing to the Left
   and Upward
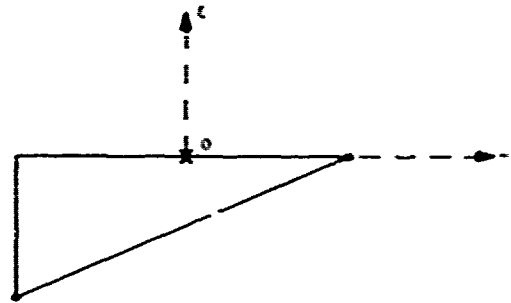
b. Slanted Right Triangle
   Pointing to the Right
   and Downward
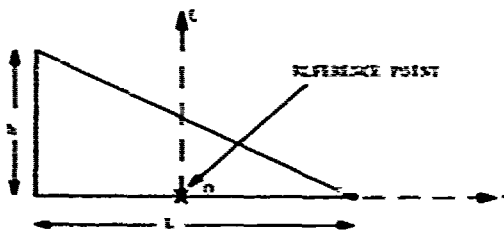
c. Slanted Right Triangle
   Pointing to the Right
   and Upward
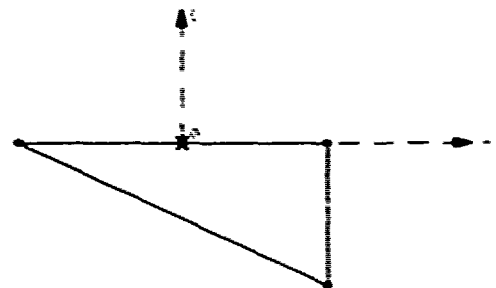
d. Slanted Right Triangle
   Pointing to the Left
   and Downward

Figure B-2. Four Orientations for the Slanted Right
             Triangle

$$W = k\left(A - \eta_0 + B'h/L\right) \tag{B-10}$$

$$W' = k\left(A - \eta_0 + B''h/L\right) \tag{B-11}$$

$$A = \cos\theta_1 \sin\gamma \tag{B-12}$$

$$T = 2\,ik\,z_1\,H/D_{p\ell} \tag{B-13}$$

$$\text{sinc } x = \sin x/x \tag{B-14}$$

CASE 2. Acute angles pointing to the right and downwards (Figure B-2b). The parameter ξ is integrated from $h(\eta/L - 1/2)$ to 0. We obtain:

$$
\begin{aligned}
I_c = (i/k)\Big\{ & (1/B')\,e^{-ikB'h/2}\,L\,\text{sinc }(W\,L/2) \\
& - (1/B'')\,e^{T-ikB''h/2}\,L\,\text{sinc }(W'L/2) \\
& + L\,\text{sinc}\left[k(A-\eta_0)L/2\right]\left(\frac{-1}{B'} + \frac{1}{B''}\,e^T\right)\Big\}
\end{aligned}
\tag{B-15}
$$

CASE 3. Acute angles pointing to the right and upwards (Figure B-2c). The parameter ξ is integrated from 0 to $h(-\eta/L + 1/2)$. We obtain:

$$
\begin{aligned}
I_c = (i/k)\Big\{ & (-1/B')\,e^{ikB'h/2}\,L\,\text{sinc }(Y\,L/2) \\
& + (1/B'')\,e^{T+ikB''h/2}\,L\,\text{sinc }(Y'L/2) \\
& + L\,\text{sinc}\left[k(A-\eta_0)L/2\right]\left(\frac{1}{B'} - \frac{1}{B''}\,e^T\right)\Big\},
\end{aligned}
\tag{B-16}
$$

where

$$Y = k\left(A - \eta_0 - B'\,h/L\right) \tag{B-17}$$

$$Y' = k\left(A - \eta_0 - B''\,h/L\right) \tag{B-18}$$

CASE 4. Acute angles pointing to the left and downward (Figure B-2d). The parameter ξ is integrated from $- h(\eta/L - 1/2)$ to 0. We obtain:

$$I_c = (i/k) \left\{ (1/B') \, e^{-ikB'h/2} \, L \, \text{sinc} \, (Y \, L/2) \right.$$

$$- (1/B'') \, e^{T-ikB''h/2} \, L \, \text{sinc} \, (Y'L/2)$$

$$\left. + L \, \text{sinc} \left[k(A-\eta_o)L/2 \right] \left(\frac{-1}{B'} + \frac{1}{B''} \, e^T \right) \right\}. \tag{B-19}$$

As in the case of the slanted rectangular scattering formulation, the present formulation for the triangle is also restricted to the case when:

$$\frac{r^2}{\lambda} \frac{\pi}{R_1} \quad \text{and} \quad \frac{\pi}{\lambda} \frac{r^2}{R_2} << \quad 1 \tag{B-20}$$

where λ is the radiation wavelength.

B.2 SCATTERING FROM AN ELEVATED SLANTED PERFECTLY CONDUCTING DISK

In this problem we take the reference point 0 (see Figure B-3) to be at the center of the disk. The boundary of the disk $\xi'(\eta)$ of radius a, is given by:

$$\xi'(\eta)^2 + \eta^2 = a^2 \tag{B-21a}$$

or

$$\xi'(\eta) = \pm \sqrt{a^2 - \eta^2} \tag{B-21b}$$

From Equation (B-3b) we have:

$$I_c = \int_{-a}^{a} d\eta \, \exp(ikA') \cdot \left[\int_{-\sqrt{a^2 - \eta^2}}^{\sqrt{a^2 - \eta^2}} d\xi \, \exp(ikB'\xi) \right.$$

$$- \exp T \int_{-\sqrt{a^2 - \eta^2}}^{\sqrt{a^2 - \eta^2}} d\xi \, \exp(ikB''\xi) \Bigg] \quad , \qquad (B\text{-}22a)$$

where $A' = A - \eta_0$. $\qquad$ $\qquad$ (B-22b)

Integrating over ξ we obtain:

$$I_c = \frac{2I_d}{kB'} - \frac{2 \exp T \; I_e}{kB''} \quad , \qquad (B\text{-}23)$$

where

$$I_d = \int_{-a}^{a} d\eta \; f(\eta) \quad , \qquad (B\text{-}24a)$$

and

$$I_e = \int_{-a}^{a} d\eta \; F(\eta) \quad , \qquad (B\text{-}24b)$$

with

$$f(\eta) = \exp(ikA'\eta) \; \sin\left(kB' \sqrt{a^2 - \eta^2}\right) \quad , \qquad (B\text{-}25a)$$

$$F(\eta) = \exp(ikA'\eta) \; \sin\left(kB'' \sqrt{a^2 - \eta^2}\right) \qquad (B\text{-}25b)$$

The integrals I_d and I_e may be approximated by the following scheme:

$$I_d = \sum_{i=1}^{8} f(\eta_i) a/4 \qquad (B\text{-}26a)$$

$$I_e = \sum_{i=1}^{8} F(\eta_i) a/4 \qquad (B\text{-}26b)$$
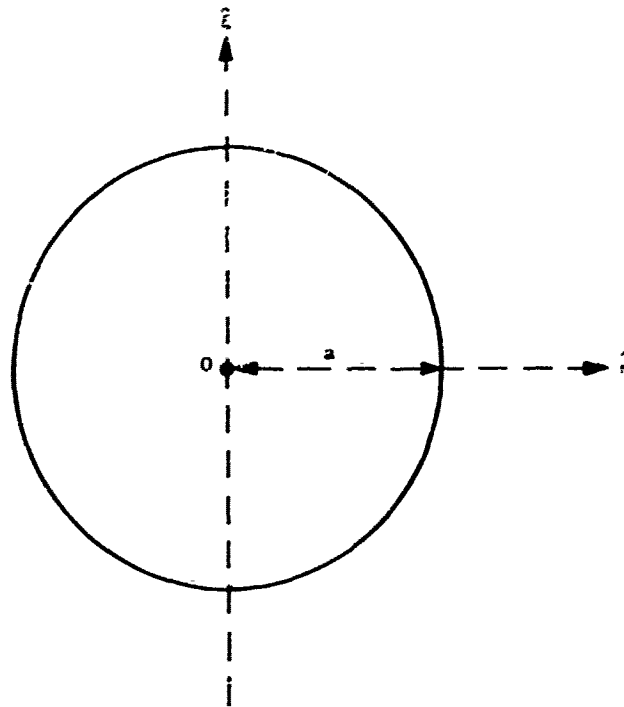
Figure B-3. Diagram Showing Coordinate Origin of ξ and η Axis at Center of Slanted Disk. Orientation $\hat{\eta}$ and $\hat{\xi}$ Are Same as Shown in Figure B-1

$$
\left.\begin{array}{l}
\eta_1 = -7\,a/8 \\[4pt]
\eta_2 = -5\,a/8 \\[4pt]
\eta_3 = -3\,a/8 \\[4pt]
\eta_4 = -a/8 \\[4pt]
\eta_5 = -\eta_4 \\[4pt]
\eta_6 = -\eta_3 \\[4pt]
\eta_7 = -\eta_2 \\[4pt]
\eta_8 = -\eta_1
\end{array}\right\} \tag{B-27}
$$

The present calculation is restricted to the case when:

$$
\frac{\pi}{\lambda}\frac{a^2}{R_1} \text{ and } \frac{\pi}{\lambda}\frac{a^2}{R_2} \ll 1 . \tag{B-28}
$$

APPENDIX C

GLIDE SLOPE SCATTERING FROM HORIZONTAL
CYLINDRICAL SURFACES

The computer program developed by the Ohio University (O.U.) group[11] to treat glide slope signal scattering by aircraft fuselages unfortunately requires excessively long running times for its execution even on the most rapid digital computers. In an effort to reduce the execution time of this program, the TSC group has been investigating approximate techniques for evaluating the various integrals which appear in the O.U., formulation of the fuselage scattering problem. Some progress has been made in this area and some of our preliminary results will now be presented.

The O.U. researchers simulate the fuselage of an aircraft by a circular cylinder. In formulating the problem of glide slope signal scattering from such a cylinder, they are required to evaluate a series of integrals of the following general form:

$$J = \int_{\pi/2}^{3\pi/2} D(\phi) \, e^{ikaf(\phi)} d\phi \quad , \tag{C-1}$$

where $k = 2\pi/\lambda$, λ is the glide slope wavelength (~ 3 ft.), a is the radius of the cylinder, and ϕ is the angular, circular, cylindrical coordinate. The numerical evaluation of these integrals is very time consuming. Our group has found, however, that, in some cases, they can be evaluated approximately with considerable accuracy using the method of stationary phase. The savings in time resulting from the use of the method of stationary phase as opposed to direct numerical integration are considerable.

The method of stationary phase is a technique for obtaining asymptotic series representations for integrals of the type given in Equation (C-1) when (ka) is a large parameter. These series expansions are in powers of $(ka)^{-1}$. The technique is based upon the fact that when (ka) is large, the principal contributions to the integral come from the vicinities of the end points of the range of integration (i.e., $\phi = \pi/2$ and $\phi = 3\pi/2$) and from the

vicinities of those points ϕ_0 within the range of integration at which the phase function $f(\phi)$ is stationary:

$$f'(\phi_0) = 0 \quad . \tag{C-2}$$

A detailed development of the method of stationary phase can be found in the monograph Asymptotic Expansions by A. Erdelyi.[12] Applying Erdelyi's general results to integrals of the type in Equation (C-1), we obtained the following approximate representation which applies when $f(\phi)$ has only one stationary point ϕ_0 within the range of integration and when $f''(\phi_0) < 0$:

$$J \approx A_1 \; (ka)^{-1/2} + A_2 \; (ka)^{-1} + A_3 \; (ka)^{-3/2} \quad , \tag{C-3}$$

where:

$$A_1 = \left(\frac{2\pi}{|f''(\phi_0)|}\right)^{1/2} D(\phi_0) \; e^{i\left(kaf(\phi_0)-\pi/4\right)} \quad , \tag{C-4}$$

$$A_2 = i \left[\frac{D(\pi/2)}{f'(\pi/2)} e^{ikaf(\pi/2)} - \frac{D(3\pi/2)}{f'(3\pi/2)} e^{ikaf(3\pi/2)}\right] \quad , \tag{C-5}$$

$$A_3 = \left\{\frac{\sqrt{\pi}}{4} D(\phi_0) \left[\frac{\sqrt{2}}{2} \frac{f^{(4)}(\phi_0)}{|f''(\phi_0)|^{5/2}} + \frac{5\sqrt{2}}{6} \frac{\left(f^{(3)}(\phi_0)\right)^2}{|f''(\phi_0)|^{7/2}}\right]\right.$$

$$+ \frac{\sqrt{\pi}}{2} D'(\phi_0) \left(\frac{2}{|f''(\phi_0)|}\right)^{1/2} \frac{f^{(3)}(\phi_0)}{\left(f''(\phi_0)\right)^2}$$

$$\left. + \frac{\sqrt{\pi}}{4} D''(\phi_0) \left(\frac{2}{|f''(\phi_0)|}\right)^{3/2}\right\} e^{i\left(kaf(\phi_0) - 3\pi/4\right)} \quad . \tag{C-6}$$

If $f''(\phi_0)$ is positive, the factors $e^{-i\pi/4}$ and $e^{-3i\pi/4}$ which appear, respectively, in Equation (C-4) and (C-6) should be replaced by their complex conjugates. Equations (C-3), (C-4), (C-5), and (C-6) represent the leading terms in the asymptotic series expansion of the integral J for large values of ka. The first and third terms in Equation (C-3) represent contributions to J from the

95

vicinity of the stationary point ϕ_0 while the second term represents contributions from the vicinities of the end points $\pi/2$ and $3\pi/2$. As one might infer from the complexity of the coefficient A_3 in Equation (C-6), the generation of any additional terms in the asymptotic expansion of J is a Herculean task. Nevertheless, we have been able to obtain reasonably good results using just the three terms shown in Equation (C-3). As an example, consider the case in which $D(\phi)$ and $f(\phi)$ are defined as follows:

$$D(\phi) = \sin \phi \left(x_0 - H_A - a \sin \phi \right) \sin \left(\frac{kx_0}{r} - \frac{kaz_2}{r} \sin \phi \right) , \quad \text{(C-7)}$$

$$f(\phi) = \frac{(x_0 - H_A)}{p} \sin \phi - \left(\frac{A}{p} + \cos \beta \right) \cos \phi + \frac{aA^2}{2p^3} \cos^2 \phi . \quad \text{(C-8)}$$

The various parameters appearing in Equations (C-7) and (C-8) are defined below:

x_0 = height of the axis of the cylinder above the ground

H_A = height of the transmitting antenna above the ground

z_2 = height of the receiving antenna above the ground

β = aspect angle between the normal to the surface of the cylinder and the position vector of the receiver relative to the cylinder

r = distance from the cylinder to the receiver

p = distance from the transmitter to the center of the cylinder

A = p multiplied by the cosine of the angle of incidence.

Let J_N denote the value of the integral (C-1) with D and f defined as in Equations (C-7) and (C-8) obtained by direct numerical integration using Simpson's rule and let J_A denote the corresponding asymptotic approximation to the integral obtained using the series expansion (C-3). In Table C-1, values of J_N and J_A are compared for several values of the aspect angle β and for ka = 21. The running times required on the PDP-10 computer to obtain each number is also indicated.

96

TABLE C-1. NUMERICAL INTEGRATION AND SERIES EXPANSION COMPARISONS

$\beta = 80$:	$J_N = -.783 - i(.824)$:	time	1320 ms
	$J_A = -.748 - i(.762)$:	time	11.7 ms
$\beta = 60$:	$J_N = -.531 - i(.801)$:	time	1360 ms
	$J_A = -.535 - i(.776)$:	time	10 ms
$\beta = 40$:	$J_N = -.337 - i(.480)$:	time	1300 ms
	$J_A = -.329 - i(.468)$:	time	10 ms
$\beta = 20$:	$J_N = .0868 - i(.581)$:	time	1460 ms
	$J_A = .0867 - i(.594)$:	time	11.7 ms

As can be seen from the table, the asymptotic approximation yields fairly good results over a wide range of aspect angles. The savings in time which result from the use of this approximate technique are clearly enormous. Much more work will be required, however, before the technique is fully perfected.

APPENDIX D

REFLECTION FROM UNEVEN GROUND IN
FRONT OF A LOCALIZER ANTENNA ARRAY

In this Appendix we develop a means of approximately treating localizer scattering when uneven ground exists in front of the localizer such as a hump in the runway.

When a localizer antenna is situated a distance, H, above a perfectly conducting flat ground plane of infinite extent, the electric field at a remote observation point can be expressed as (Reference 1, Equation (2.58)):

$$\vec{E}_i = \hat{u} \, E_o f(\phi) \, \frac{e^{ikR}}{R} \left[1 - e^{2ikzH/D_p} \right] \qquad (D-1)$$

where $\hat{u}$ is the unit vector giving the direction of polarization of the field; $f(\phi)$ is the horizontal antenna gain; R is the distance from the antenna to the observation point; k is 2π over the wavelength; D_p is the projection of R on the ground plane; H is the distance of the antenna from the ground plane; E_o is an electric field amplitude and z' is the distance of the observation point from the ground plane. The above formula for $\vec{E}_i$ is restricted to the case when the elevation angle of the ray to the observation point is small.

In actual airports, however, the reflecting ground directly in front of the localizer antenna may be uneven. Figure D-1 shows, for example, the lateral profile of a portion of the ground in front of the localizer antenna at the Syracuse-Hancock Airport.

In order to treat this and similar cases approximately we consider a simple model where the uneven foreground consists of a number of connected flat surfaces having no height variation in the direction perpendicular to the vertical plane through the runway center line. The end of the runway near the localizer is taken as the origin of the coordinate system x-z. Figure D-2 shows a diagram of the simple model we are considering. How well this simple geometrical model works, depends, of course, on the complexity of the contours of the actual ground being considered.
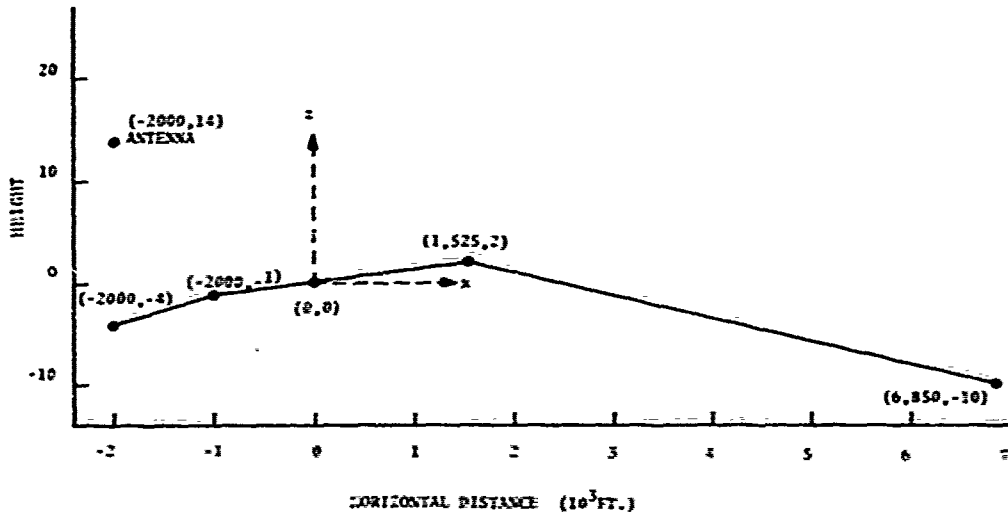
98

Figure D-1.   Lateral Profile Showing a Portion of the
               Ground in Front of the Localizer Antenna at
               the Syracuse-Hancock Airport
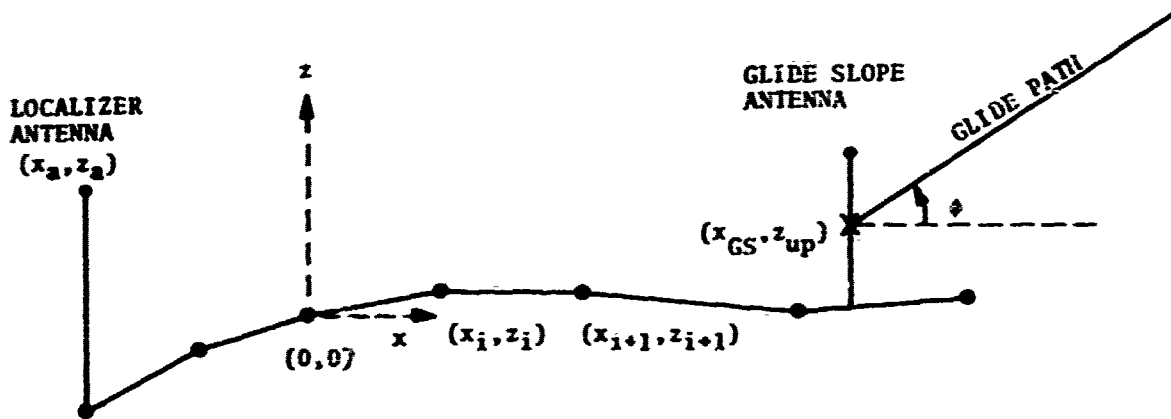

Figure D-2.   Diagram Showing a Model of the Reflecting Ground
               in Front of the Localizer Antenna. The End of
               the Runway Near the Localizer Is the Origin of
               the Coordinate System

99

In order to still be able to use Equation (D-1) for this uneven ground plane case, we consider the following model. We assume geometric optical rays emanating from the localizer antenna and being reflected from a flat ground slab segment. The rays reflecting from the two ends of the slab define a reflection region on the glide path as shown in Figure D-3. Within this region we use, in this approximation, Equation D-1 with H now the perpendicular distance of the antenna from the extended plane of the ground slab; and z' now the perpendicular distance of the observation point on the glide path from the extended plane of the slab.

Given the coordinates of the end points of the slab (x_i, z_i) and (x_j, z_j) where $j = i+1$ (see Figure D-3) we obtain the limits, x_{min} and x_{max}, of the radiated zone on the glide path:

$$x_{min} = x_{GS} + \ell_2$$

where:

$$\ell_2 = \frac{(x_{GS} - x_j) \, \text{Tan} \, \theta_4 + z_j - z_{up}}{\text{Tan} \, \phi - \text{Tan} \, \theta_4} \quad ,$$

$$\theta_4 = \theta_1 + 2\theta_2 \quad ,$$

$$\theta_1 = \text{Tan}^{-1}\left(\frac{z_a - z_j}{x_j - x_a}\right) \quad ,$$

$$\theta_2 = \text{Tan}^{-1}\left(\frac{z_j - z_i}{x_j - x_i}\right) \quad .$$

Also:

$$x_{max} = x_{GS} + \ell_1 \quad ,$$

$$\ell_1 = \frac{(x_{GS} - x_i) \, \text{Tan} \, \theta'_4 + z_i - z_{up}}{\text{Tan} \, \phi - \text{Tan} \, \theta'_4} \quad ,$$

$$\theta'_4 = \theta'_1 + 2\theta_2 \quad ,$$

$$\theta'_1 = \text{Tan}^{-1}\left(\frac{z_a - z_i}{x_i - x_a}\right) \quad .$$
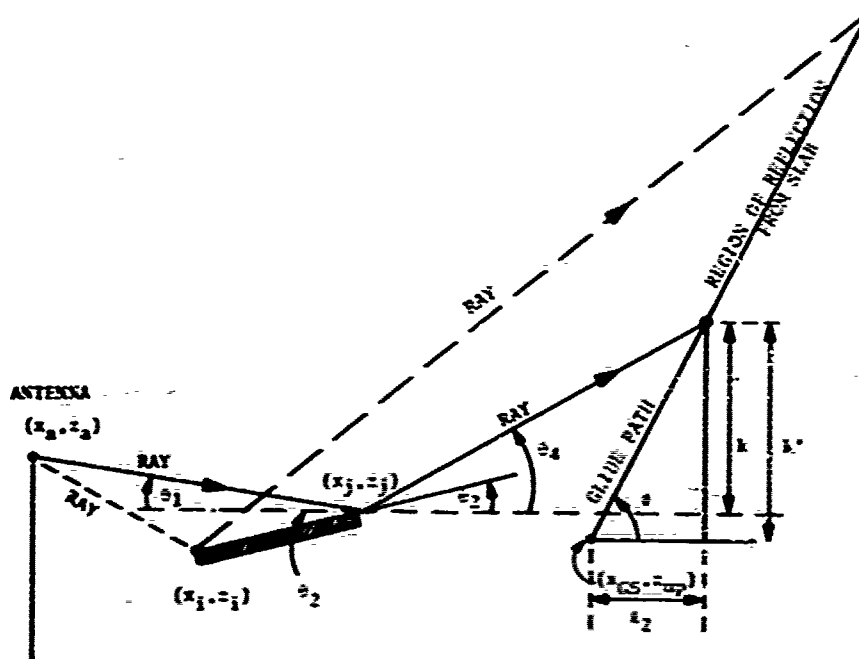
Figure D-3. Diagram For Calculating the Limits of Reflection Region for a Slab
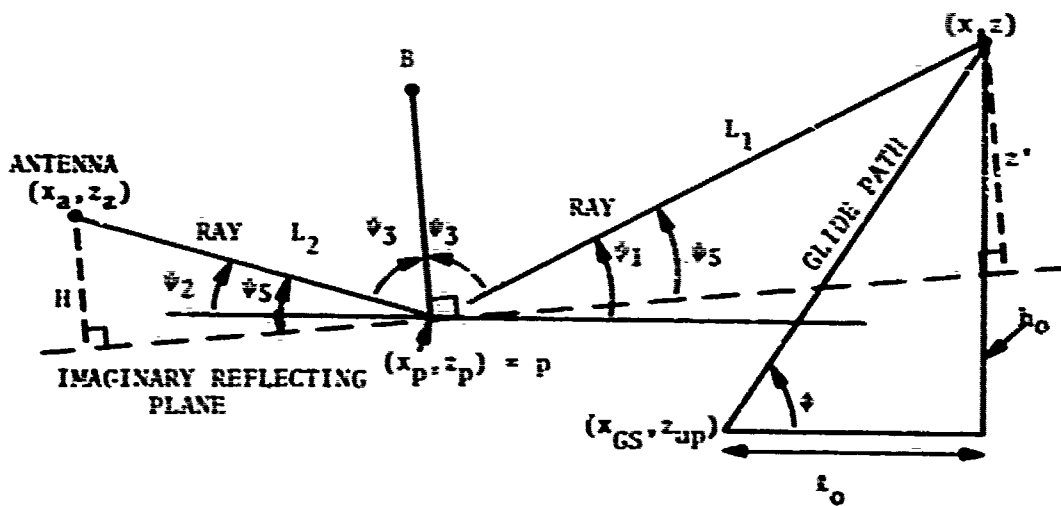

Figure D-4. Diagram for Calculating the Quantities H and z' When the Observation Point Lies on the Overlapping or Gap Regions

For the b considered above, the projection of the localizer antenna onto the extension of the slab has a perpendicular distance given by (see Figure D-4):

$$H = \left[(x_i - x_a) \left(\frac{z_j - z_i}{x_j - x_i} \right) + (z_a - z_i) \right] \cos \theta_2 .$$

The projection of an observation point (x,z) located on the glide path onto the extension of the slab has a perpendicular distance given by (see Figure D-4):

$$z' = \Delta z \cos \theta_2$$

where:

$$\Delta z = (x - x_{GS}) \, \mathrm{Tan} \, \phi - (x - x_j) \left(\frac{z_j - z_i}{x_j - x_i} \right) - (z_j - z_{up}) .$$

Since successive slabs make different angles with respect to a horizontal ground plane, the radiated regions of successive slabs may overlap or there may be gaps between them. For these gaps or overlapping zones, we use another approximation scheme to calculate the quantities H and z'. Figure D-4 shows a diagram for this method. The point $P = (x_p, z_p)$ is where two adjacent slabs meet. We draw, then, a line, L_2, from the antenna to p and a line, L_1, from p to (x,z) a point on the glide path in the zone of the gap or overlap. We would like to construct an imaginary reflecting plane for these rays. Hence, on a plane tangent to the rays we draw a line, pB, through the point, p, bisecting the angle between L_2 and L_1. Then the plane through p perpendicular to the line pB is the imaginary reflecting plane required for the rays. For the given point (x,z) the projections H and z' on this reflection plane can be calculated as follows:

$$\ell_o = x - x_{GS},$$
$$h_o = \ell_o \, \mathrm{Tan} \, \phi,$$
$$z = h_o + z_{up},$$

$$\psi_1 = \text{Tan}^{-1} \frac{z - z_p}{x - x_p} \; ,$$

$$\psi_2 = \text{Tan}^{-1} \frac{z_a - z_p}{x_p - x_a} \; ,$$

$$\psi_3 = \frac{1}{2} \left(\pi - \psi_1 - \psi_2 \right) \; ,$$

$$\psi_5 = \frac{\pi}{2} - \psi_3 \; ,$$

$$L_1 = \sqrt{(x - x_p)^2 + (z - z_p)^2} \quad .$$

$$z' = L_1 \sin \psi_5$$

$$L_2 = \sqrt{(x_p - x_a)^2 + (z_a - z_p)^2} \; ,$$

$$H = L_2 \sin \psi_5 \quad .$$

This set of equations can be used to calculate the corresponding H's and z''s for a sequence of points in the gap or overlapping region. We note that for a convex reflecting bump there is a gap and for a concave reflecting depression there is an overlap. Also we note that as the point (x,z) moves to the boundary points of the gap region, the imaginary plane will then coincide with the actual ground planes meeting at p.

In summary, in order to treat approximately the scattering problem when non-flat terrain exists in front of the localizer, we begin with a model of a series of connected slabs. From each slab we obtain a geometric optics reflection region on the glide path. Then we find regions of gaps and overlaps for which we use the second method described. For the remaining regions the first method described is used.

APPENDIX E

THEORETICAL LINEAR ARRAY PATTERNS

The CDI pattern that is measured in orbital flight around a
localizer installation can be quite different from the ideal pat-
tern expected on the basis of the signal distribution to the array
and the known element patterns. In many instances, this may be
only partially explained by the influences of the scattering
environment. An important additional factor can be mutual couplings
between the array elements, the magnitudes of which can be specific
to the particular localizer installation. The consequence of this
is that spurious signal currents are induced in individual elements
which alter the total currents from the values implied by power
dividing networks, phase shifters, etc. Instrumentation is
available to measure actual element current magnitudes and phases.[13]
Given such measurements, it is possible to calculate the signal
patterns that would be radiated by the array situated on a flat
ground plane. Routines for accomplishing these calculations for
an arbitrary linear array localizer have been incorporated in the
ILSLOC program[3] and are called into use by designating the variable
"MODE" as 7 or 8. Detailed input data specifications are given in
the ILSLOC user's manual.[3]

REFERENCES

1. G. Chin, L. Jordan, D. Kahn, S. Morin, "Instrument Landing System Scattering." Report No. FAA RD-72-137, Transportation Systems Center. December 1972, Final Report.

2. D. M. Cunnold, R. V. Row, C. F. Arnold, "Analytical and Experimental Studies of Coupling Between Antenna Over a Two-Dimensional Ground Surface of Known Contour," IEEE Trans. Antennas and Propagation, Vol. AP-16, pp. 291-298, May 1968.

3. G. Chin, L. Jordan, D. Kahn, S. Morin, D. Newson, A. Watson, "Users Manual for ILSLOC: Simulation for Derogation Effects on the Localizer Portion of the Instrument Landing Systems," May 1973, Operational Handbook Report No. FAA-RD-73-76, Transportation Systems Center, Cambridge MA 02142, August 1973.

4. Reference 1, page 22, Equation 2.48.

5. G. Chin, L. Jordan, D. Kahn, S. Morin, D. Newsom, "ILS Localizer Performance Study Part 1 Dallas/Fort Worth Regional Airport and Model Validation-Syracuse-Hancock Airport," Report No. FAA-RD-72-96, Transportation Systems Center, Cambridge MA 02142, July 1972. A second report covering the effects of the Delta and Braniff Hangars on the course structure is in preparation.

6. L. Jordan, D. Kahn, S. Morin, D. Newsom, R. Silva, "Course Structure-Runway 28R San Francisco Airport," Report No. DOT-TSC-FAA- 73-11, Transportation Systems Center, Cambridge MA 02142, September 1973.

7. L. Jordan, D. Kahn, S. Lam, S. Morin, D. Newsom, "Performance Predictions for a Parabolic Localizer Antenna on Runway 28R San Francisco Airport," Report No. FAA-RD-73-81, Transportation Systems Center, Cambridge MA 02142, June 1973.

8. L. Jordan, D. Kahn, S. Lam, S. Morin, D. Newsom, "ILS Localizer Performance Prediction of an Alford 1B Array Near a Limited Access Road at the New Orleans Airport." Report No. DOT-TSC-FAA-73-15, August 1973.

105

9. M. Abramowitz, I. A. Stegun, Editors, "Handbook of Mathematical Functions." Dover Publications, Inc., New York, 1965, page 361.

10. R. W. Redlich, "Theory of Localizer Signal Disturbances by Reflections from a Cylindrical Fuselage." Tech. Memo 6A, Electrical Engineering Department, Ohio University, March 30, 1970. Prepared for Department of Transportation, FAA, Systems Research and Development Service, FA 69 WA-2066.

11. R. W. Redlich, et al, "Instrument Landing System Improvement Program," Interim Report SRDS-RD-70-9, Department of Electrical Engineering, Ohio University, Athens, Ohio, January 1970.

12. A. Erdelyi, Asymtotic Expansions, Dover Publication, Inc., New York, 1956.

13. Redlich, op cit., p. 30.